Delft University of Technology

Study of solidification cracking during laser welding in advanced high strength steels
A combined experimental and numerical approach

Agarwal, Gautam

DOI
10.4233/uuid:dd0e5ab0-1427-4ecc-a8d8-4e8f35050fca

Publication date
2019

Document Version
Final published version

Important note
To cite this publication, please use the final published version (if applicable).
Please check the document version above.

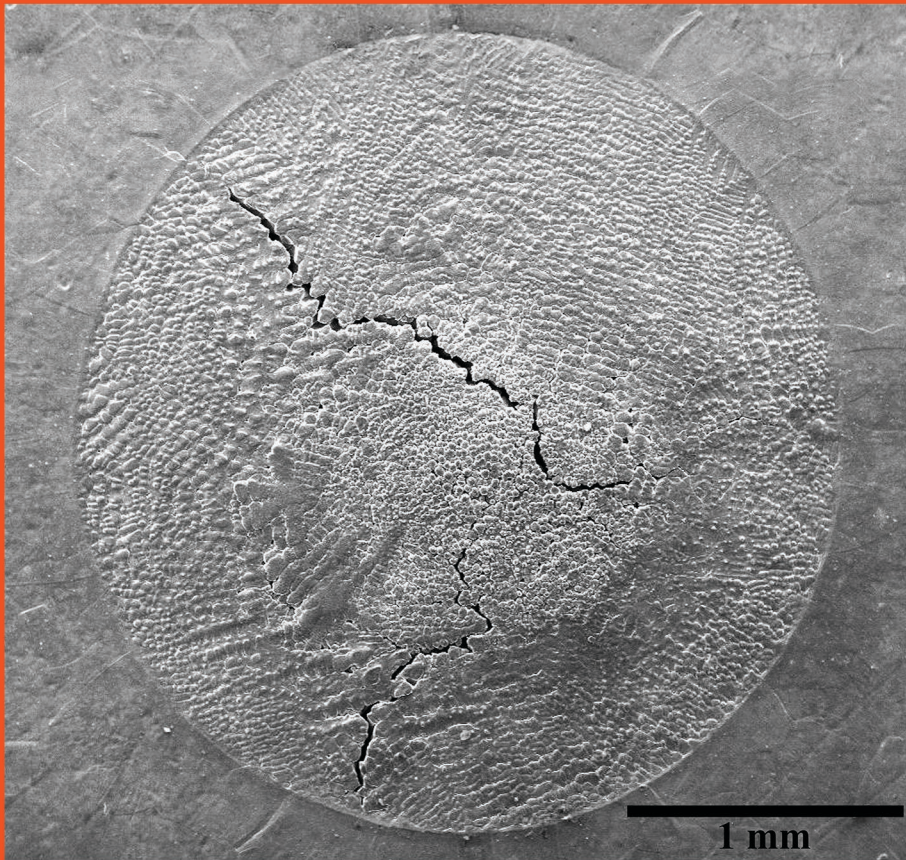# Study of solidification cracking during laser welding in advanced high strength steels

A combined experimental and numerical approach

1 mm

Gautam Agarwal

Study of solidification cracking during laser welding in advanced high strength steels

A combined experimental and numerical approach

Study of solidification cracking during laser welding in advanced high strength steels

A combined experimental and numerical approach

Proefschrift

ter verkrijging van de graad van doctor
aan de Technische Universiteit Delft,
op gezag van de Rector Magnificus prof.dr.ir. T.H.J.J van der Hagen,
voorzitter van het College voor Promoties,
in het openbaar te verdedigen op
maandag 27 mei 2019 om 15:00 uur

door

Gautam AGARWAL

Master of Science in Metallurgical Engineering,
Rheinisch-Westfälische Technische Hochschule (RWTH) Aachen, Aachen, Germany,
geboren te Kota, Rajasthan, India.

Dit proefschrift is goedgekeurd door de promotoren.

Samenstelling promotiecommissie bestaat uit:
Rector Magnificus,   voorzitter
Dr.ir. M.J.M. Hermans   Technische Universiteit Delft, promotor
Prof.dr. I.M. Richardson   Technische Universiteit Delft, promotor

Onafhankelijke leden:
Prof.dr. C.E. Cross   Los Alamos National Laboratory, USA
Prof.dr. D. Eskin   Brunel University London, UK
Prof.Dr.-Ing. T. Kannengiesser Otto von Guericke University Magdeburg, Germany
Prof.dr.ir. J. Sietsma   Technische Universiteit Delft
Dr.ir. E.M. van der Aa   Tata Steel Nederland
Prof.dr.ir. M.L. Kaminski   Technische Universiteit Delft, reservelid

If anything is worth doing, do it with all your heart.[*]

Gautama Buddha

Contents

Preface

Preventing solidification cracking is an essential prerequisite for the safety of a welded structure. An undetected solidification crack has the potential to cause premature failure during service. Two conditions generated by a weld thermal cycle are responsible for the initiation of solidification cracks. The first is the presence of excessive stresses/strains imposed on the solidifying weld metal and the second is the existence of a weak solidifying microstructure. For more than five decades, weld solidification cracking has been a subject of considerable interest. Cracking has been observed in various alloys, used in a wide range of engineering applications. Despite achieving a better understanding over this period, an accurate prediction of the occurrence of solidification cracking under a specific set of conditions remains difficult. An alloy with a high susceptibility to solidification cracking can still exhibit good weldability upon selection of appropriate welding conditions. Conversely, an alloy with supposedly high resistance to cracking, can still fail when subjected to inappropriate welding conditions.

The objective of the research work reported in this dissertation is to study and elucidate the solidification cracking phenomenon in two popular and commercially available automotive sheet steels, namely transformation-induced plasticity (TRIP) and dual phase (DP) steels. In particular, the effect of restraint (strain imposed), shape of the weld pool, solidification morphology, segregation, solidification temperature range, dendrite coherency and interdendritic liquid feeding on susceptibility to solidification cracking is considered.

Gautam AGARWAL
Delft, January 2019

1

Introduction

1.1 Introduction

THE CO$_2$ emission regulation of passenger vehicles has become stringent in the last two decades and the target emission between 2020-2025 seems to converge globally to 95-120 g of CO$_2$ per km [1], as can be seen in Figure 1.1. One of the fundamental ways to achieve this target in the automotive industry is to reduce the overall weight of the vehicle. Naturally, reduction of weight should not compromise the vehicle performance and passenger safety. To meet this demand, new steels under the umbrella of advanced high strength steel (AHSS) are being increasingly developed and adopted. These steels comprise on average, 30-35 percent of a typical car body-in-white weight [2] and possess high strength, ductility and toughness. The increased strength and ductility permits the use of thinner gauge steels thus reducing the vehicle weight [†].

The typical values of strength and ductility of different steels (conventional, AHSS) can be seen in Figure 1.2. The AHSSs used in the automotive industry normally include dual-phase (DP) steels, transformation-induced plasticity (TRIP) steels, twinning-induced plasticity (TWIP) steels, complex phase (CP) steel and martensitic steel with tensile strengths and ductilities varying from 600-1200 MPa and 10-40 %, respectively [3, 4]. Typically, these steels are used as chassis components, B-pillars, crash boxes, engine cradles *etc.* [4]. Figure 1.3 (a) shows some important parts of the body-in-white.

Apart from formability requirements in these steels, weldability of such steels is important. The higher content of alloying elements in some of the AHSSs, required for achieving necessary mechanical properties render them susceptible to solidification cracking during welding. Some automotive manufacturers have reported solidification cracking in assembling parts during laser welding. Typically, preformed parts are welded in a flange geometry and the width of the flange can be reduced compared to the flange width required for resistance spot welding to decrease the weight of the car body. When

---

[†]Emission from primary steel production is 7-8 times less compared to its nearest rival, aluminium [2]. Therefore, for overall reduction in emissions and production cost, steels are still the preferred choice in the automotive industry.

1
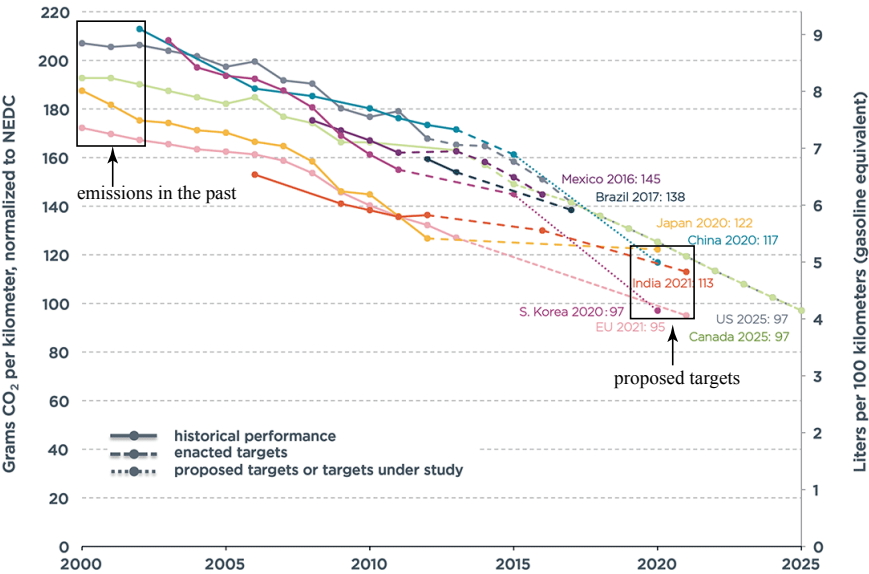
Figure 1.1: Passenger car CO_2 emission standard and fuel consumption, normalised to New European Driving Cycle (NEDC). The figure also indicates the historical and proposed emission standard of various countries. With permission form reference [1].
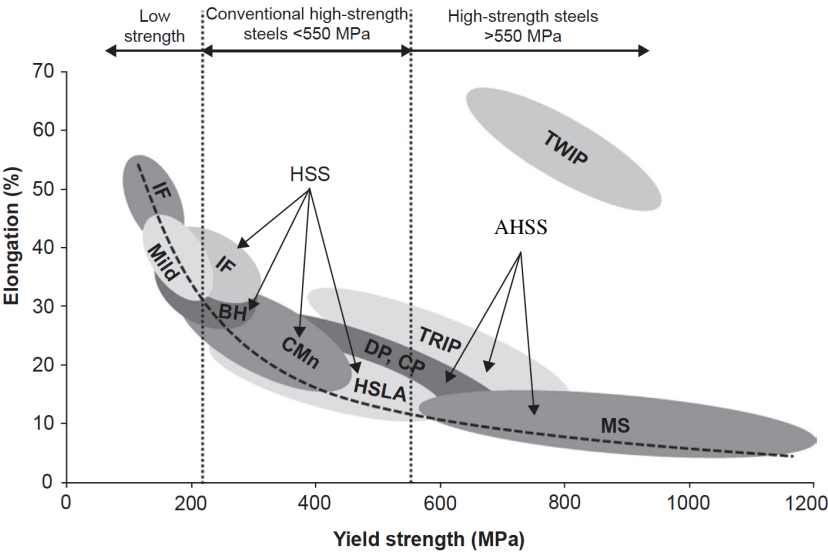
Figure 1.2: Strength *versus* ductility diagram of various steels including the present AHSS grades. With permission from reference [3].
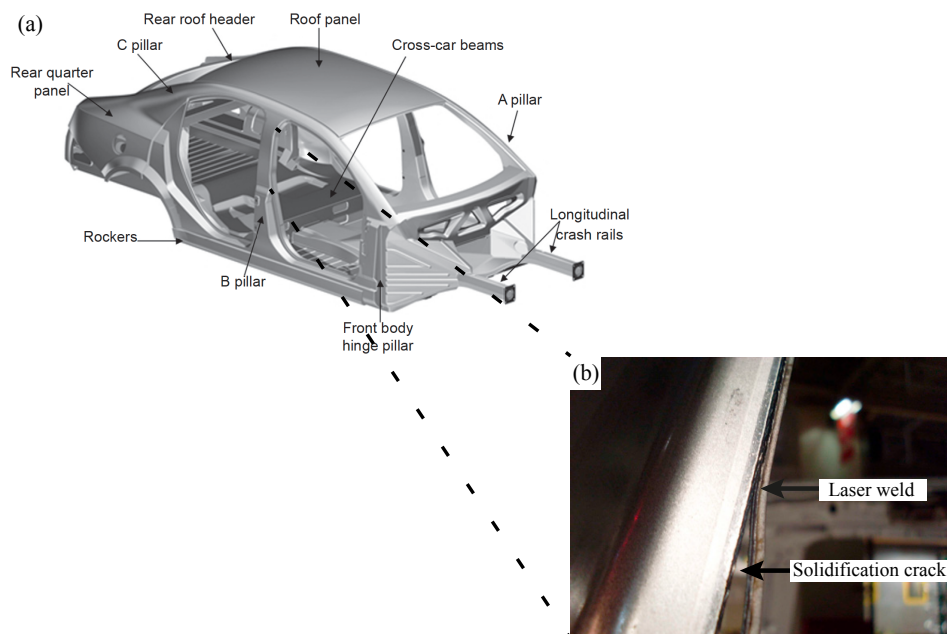
Figure 1.3: (a) Typical parts in body in white (BIW), (b) solidification cracking in the B-pillar of a Volvo XC60 car body. (a), (b) with permission from references [3] and [5] respectively.

welding is carried out below a critical distance from the edge, solidification cracking is often reported. For instance, Larsson reported [5] solidification cracking during laser welding of the B-pillar used in the Volvo XC60 (Figure 1.3 (b)).

In the continuous galvanising lines in steel production, entry and exit coils are joined by laser welding. During welding some of the AHSSs, solidification cracking may also take place. This leads to serious downtime and production losses and needs to be avoided.

1.2 Aim of the study

Solidification cracking or hot cracking results from a complex interaction between the metallurgical, mechanical and thermal conditions that prevail during welding. The objective of the present work is to study and elucidate the solidification cracking phenomenon in two popular and commercially available AHSSs, namely TRIP and DP steel sheets. In particular, the effect of the following aspects on susceptibility to solidification cracking is considered; restraint (strain imposed), shape of the weld pool, solidification morphology, segregation, solidification temperature range, dendrite coherency and interdendritic liquid feeding. For this purpose a mixture of both experimental and modelling techniques have been used. A laser welding arrangement, similar to that used in the standard hot cracking test [6], was employed. During welding, temperatures and strains were measured. To study the solidification behaviour in more detail, high-temperature laser scanning confocal microscopy was employed.

1

To investigate the solidification microstructure, the weld metal was characterised using a wide variety of techniques including optical microscopy, scanning electron microscopy, energy dispersive X-ray spectroscopy (EDS), electron probe microanalysis (EPMA), electron backscatter diffraction (EBSD) and atom probe tomography (APT).

To predict the strain fields, a 3D finite element (FE) thermo-mechanical model of laser welding was developed. The model was validated based on temperature and strain measurements. Phase field modelling was applied to study the solidification behaviour of both the steels under similar conditions that exist(ed) in experiments.

Both the experimental and modelling results are discussed pertaining to the effect of various factors affecting solidification cracking which include mechanical restraint, solidification temperature range, solidification morphology, solute segregation, liquid feeding capability and welding parameters *etc.*

1.3 Outline of the thesis

In chapter 2, an introduction to common welding practices for automotive applications (resistance spot welding and laser welding) is given. The development of stresses/strains and microstructure during welding is provided. This is followed by a general description of the solidification cracking phenomenon. A brief account of previous work on solidification cracking, also known as hot tearing or hot cracking in casting, is provided. Finally, some common hot cracking tests, including both externally loaded and self-restraint tests are described.

In chapter 3, the composition and the base metal microstructure of the steels used in the present work is outlined. The experimental procedures and modelling methods, employed in this study, are described. The hot cracking test arrangement, welding parameters, high speed camera imaging conditions, digital image correlation technique, microstructural characterisation methods and high temperature microscopy are elaborated. Subsequently, the constructed finite element (FE) thermal-mechanical model of laser welding and a phase field model for microstructural evolution upon solidification are described.

In chapter 4, results of strain measurement using the digital image correlation (DIC) technique are presented. External illumination combined with an optical bandpass filter allowed measurement of strain close to the fusion boundary. A finite element thermal-mechanical model of laser welding was constructed and validated based on the measured thermal cycles and strain measurements.

Susceptibility to weld solidification cracking in TRIP steel sheets is reported in chapter 5, using a modified standard hot cracking test. Bead-on-plate laser welding was performed on a single sided clamped specimen at increasing distances from the free edge. Solidification cracking was observed when welding was carried out close to the free edge and beyond a certain minimum distance, no cracking occurred. The validated finite element thermal-mechanical model (from chapter 4) was used to explain the cracking tendency. Heat input was varied by increasing/decreasing the welding speed, to study its effect on the solidification cracking susceptibility.

In chapter 6, the results of *in-situ* solidification experiments using a high-temperature laser scanning confocal microscope (HTLSCM) are presented and discussed. A stable melt pool was created at the centre of a thin circular disk shaped specimen while the outer

rim remained solid. Solidification cracking in TRIP steel was observed *in-situ* during the last stages of solidification. Atom probe tomography was used to obtain the elemental composition in the interdendritic region near the crack. The results are compared with those from a phase field solidification model and further discussed pertaining to the effect of liquid feeding and phosphorus microsegregation in the interdenritic regions.

In chapter 7, the results of *in-situ* experimental observations of liquid feeding during solidification of DP steel are presented. The liquid flow rate in the inter-cellular regions is derived together with the pressure difference that leads to the observed flow. The liquid flow rate is compared with the rate of solidification shrinkage and the rate of thermal deformation.

A general discussion based on the outcome of the present work is provided in chapter 8. In addition, results are presented to discuss the effect of solidification morphology (shape of weld pool), solid-liquid interface growth rate and strain distribution in the mushy region on solidification cracking. From the phase field model of solidification behind the weld pool in the TRIP and DP steels, the solidification cracking tendency is explained based on dendritic coherency, phosphorus segregation and liquid feeding tendency.

Finally, in chapter 9, conclusions, recommendations and the scope for future work based on the outcome of this study are presented.

References

[1] *International council on clean transportation. Global passenger vehicle standards (2014). Retrieved (21-04-2018) from: http://theicct.org/info-tools/global-passenger-vehicle-standards*.

[2] S. Keeler, M. Kimchi and P. J. Mconey, *Advanced high-strength steels application guidelines*, Technical Report 6.0 (World Auto Steel, 2017).

[3] T. Hilditch, T. de Souza and P. Hodgson, *2 - Properties and automotive applications of advanced high-strength steels (AHSS),* in *Welding and Joining of Advanced High Strength Steels (AHSS)*, edited by M. Shome and M. Tumuluru (Woodhead Publishing, 2015) pp. 9 – 28.

[4] C. Lesch, N. Kwiaton and F. B. Klose, *Advanced high strength steels (AHSS) for automotive applications tailored properties by smart microstructural adjustments,* steel research international **88**, 1700210 (2017).

[5] J. K. Larsson, *Avoidance of crack inducement when laser welding hot-formed car body components — a variable analysis,* Physics Procedia **5**, 115 (2010), Laser assisted net shape engineering 6, Proceedings of the LANE 2010, Part 2.

[6] VDEh, *SEP 1220-3: Testing and documentation guideline for the joinability of thin sheet of steel - Part 3: Laser beam welding*, edited by STAHL (2011).

2

Background

I<small>N</small> this chapter, an introduction to common welding practices in the automotive sector, residual stress development during welding, microstructural features of the welded joint, hot cracking phenomena and hot cracking tests is provided.

2.1 Welding processes

In the automotive industry, the most common welding methods applied to manufacture body-in-white (BIW) are resistance spot welding (RSW) and laser beam welding (LBM) [1]. Resistance spot welding is used universally in automotive manufacturing and the use of laser beam welding has increased over the last two decades.

2.1.1 Resistance spot welding

Resistance spot welding is the most common welding method used in the automotive industry [2, 3]. In this process, contacting metal surfaces are joined by the heat obtained when electric current is passed through the interface of the sheets to be welded. The heat is mainly generated due to the electrical resistance at the interface, *i.e.* Joule heating. When the current is applied, the metal parts around the interface are heated, resulting in melting and the formation of a weld pool. When current is switched off, the temperature starts to decrease and the weld pool solidifies to form a joint, generally referred to as weld nugget. Due to the simplicity of implementation, it is extensively used for joining the metal sheet components (0.5 − 3 mm) in the car body with the number of spot welds ranging from 2000-5000 [4]. Figure 2.1 shows a schematic description of the resistance spot welding process [5]. Typical electrode force varies between 3.5-4.5 kN, welding current between 5.4-6.2 A and weld time between 220-320 ms [6–8]. In some AHSSs, single pulse spot welds have low load bearing capacity in cross tension strength tests. To improve the mechanical properties, a second current pulse is often applied. The second pulse has an annealing effect on the martensitic microstructure that is formed due to the high cooling rates encountered. Other important issues in resistance spot welding include liquid metal embrittlement [9], which occurs due to liquid metal penetration

along grain boundaries.
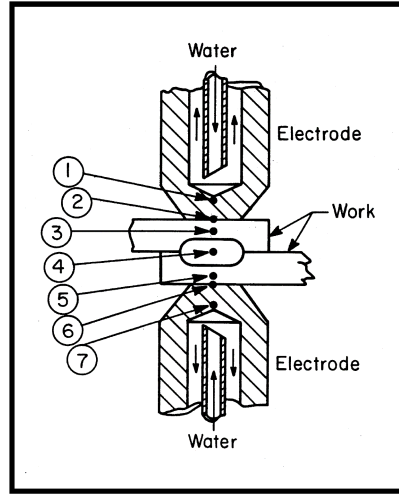
Figure 2.1: Schematic overview of RSW. Electrodes 1 and 7 press against workpieces 3 and 5. A current is then passed through these components. Because of the electrical contact resistance, heat will be generated at electrode/workpiece interfaces 2 and 6 and faying surface 4. The heat at the faying face melts the workpieces to form a nugget, 4. To prevent melting at the electrode/workpiece interface, water is circulated in the cooling chamber of the electrodes. The image and caption are reproduced from reference [5] with permission from the American Welding Society.

2.1.2 Laser beam welding

In the last two decades, laser beam welding has become increasingly popular in the automotive industry. For example, the Volkswagen Golf V model consists of 70 m of laser welding and 1500 spot welds whereas the Golf IV consisted of only 1.4 m of laser welded seams and 4500 spot welds. Increased usage of laser welding allowed a 25 % reduction in production time [10]. Similarly, laser welding already accounts for 15 % of the welded joints in the Audi A3 [11].

The active laser media in a laser can be solid, liquid or gas. Typical solid-state lasing medium are neodymium doped yttrium aluminium garnet (Nd:YAG), ruby and Nd:glass. Examples of gas lasers include CO_2 and He-Ne. In the automotive industry, CO_2 and Nd:YAG lasers ($\lambda = 1064$ nm) with power range $4 - 15$ kW are commonly used [12]. The absorption of a material depends on the wavelength of the laser [13]. Figure 2.2 shows a schematic of a typical laser beam welding setup, including the fiber and optics [14].

In laser welding, the intense laser beam is focused onto the material, leading to the formation of a melt pool. The concentrated heat source provides a high power density in the range of $10^8 - 10^{10}$ W m^{-2}, facilitating welding at high speeds and thereby increasing productivity [15]. Additionally, welds with a narrow heat affected zones and low thermal distortion can be obtained. Depending upon the energy density, laser welding can be achieved in two modes, as shown in Figure 2.3. With low energy density, the heat is absorbed locally at the surface to create a melt pool and penetration is achieved
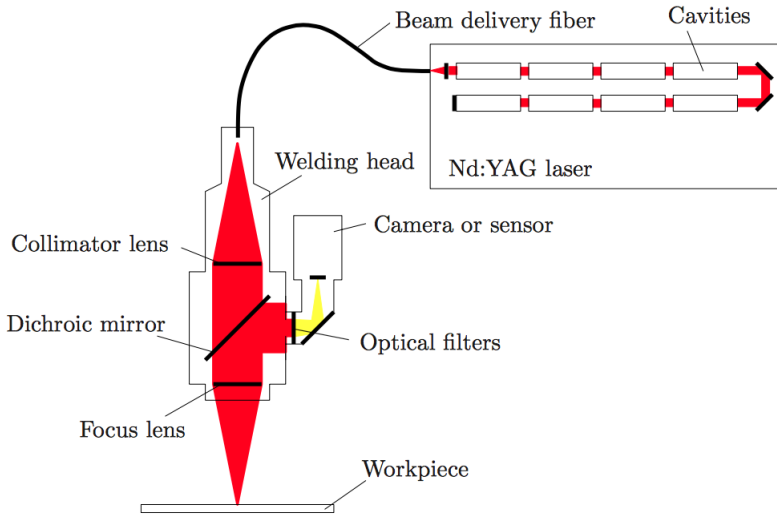
Figure 2.2: Schematic overview of a typical laser welding system. Taken from reference [14].
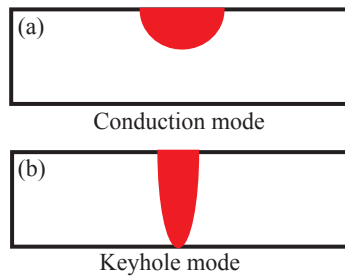
Figure 2.3: The two operational modes of laser beam welding; (a) conduction mode and (b) keyhole mode.

by conduction of the heat from the surface into the material. When energy density is increased beyond a threshold, locally the temperature surpasses the melting point and vaporisation occurs. The metal vapour exerts a recoil pressure on the melt pool and creates a depression. Depending on the amount of recoil pressure, the depression can extend to the entire thickness of the specimen, resulting in the formation of a keyhole. The keyhole is filled with an ionized plume of vapour and atmospheric gas. As a result of multiple reflections within the keyhole, laser beam absorption increases significantly resulting in deep and narrow welds [16, 17]. The threshold energy required to melt and vaporise the material, *i.e.* to create the keyhole, depends on the physical properties of the material (absorption coefficient, heat conduction, boiling point), the wavelength of the laser light and the properties of the surface of the workpiece. In the automotive industry, laser welding is generally used in the keyhole mode [18].

A typical car body has 40 m of weld flanges [19]; resistance spot welding requires a flange width of 16 mm to accommodate the electrode system on either side [20]. The

flange width can be reduced by using laser welding (Figure 2.4) leading to overall weight reductions of 30-40 kg [19].

(a) Resistance spot welding   (b) Laser welding
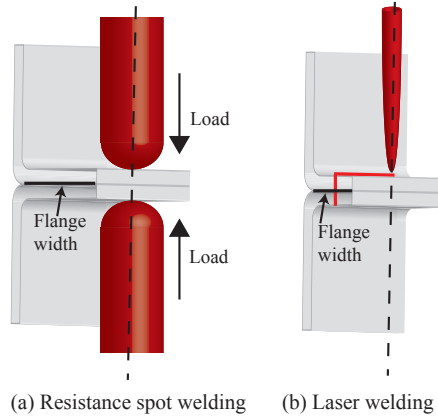
Figure 2.4: A schematic showing flange width required in the case of: (a) Resistance spot welding and (b) Laser welding.

2.2 Material response to welding

The introduction of a localised heat source on a material has two broad mutual effects. The material experiences a non-uniform heating and cooling cycle, which leads to stresses, deformation and/or distortion. In addition, fusion welding destroys the carefully designed microstructure, resulting in an as-cast structure. Regions close to the weld also experience a thermal cycle that leads to the formation of a heat affected zone, with a different microstructure to the base material.

2.2.1 Residual and transient stresses/strain during welding

Residual stresses are the stresses that exist in a material in absence of any externally applied forces [21]. Residual stresses are also referred to as internal stresses or inherent stresses [22]. These stresses arise as a result of misfits between different regions in a material, which originate due to gradients in temperature and/or deformation [23, 24]. In fusion welding, residual stresses are generated due to an inhomogeneous temperature field and local plastic deformation, and are often referred to as thermal stresses [22, 24].

Residual stresses are generally categorised on the basis of length scale at which they are present (Figure 2.5). Type I residual stresses or residual macro-stresses (σ^I) extend over macroscopic areas, *i.e.* they represent the average residual stresses acting over several grains. Type II residual stresses or residual meso-stresses (σ^{II}) represent the stresses which exist between neighbouring grains. Type III stresses (σ^{III}), also referred to as residual micro-stresses exist within a grain and originate due to the presence of voids, dislocations or solutes in a crystal lattice [21, 24]. The total residual stress (σ_R) is the sum of these three type of stresses.

In welding, residual stresses are defined with respect to the welding direction, as
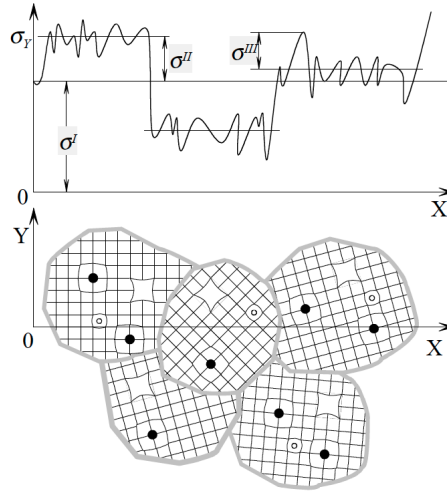
Figure 2.5: Classification of residual stresses on the length scales. With permission from reference [25]. This figure was adopted in reference [25] from the reference [21].

shown in Figure 2.6. Longitudinal residual stresses are parallel to the welding direction while transverse stresses are perpendicular in the plane of the specimen. Normal stresses are perpendicular to the plane of the specimen and the welding direction.
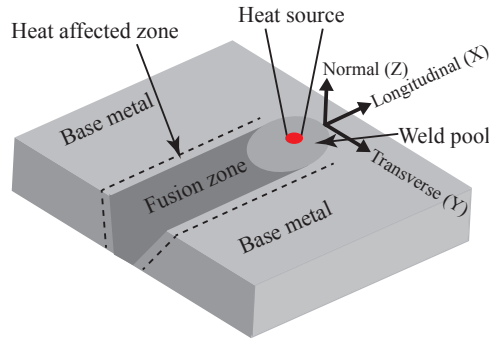
Figure 2.6: A schematic diagram showing the three distinct regions as the heat source passes through the base material(s). Stresses with respect to the welding direction are also indicated.

The transient development of longitudinal stresses can be described using a simple model from reference [25]. Consider the case of thin plate welding as shown in Figure 2.7 (a). For simplicity, the following assumptions are made:

1. The material behaviour is perfect elastic-plastic (Figure 2.7 (b)).

2. A constant thermal expansion coefficient is assumed. Moreover, dilation due to phase transformations is neglected (Figure 2.7 (c)).

(a)
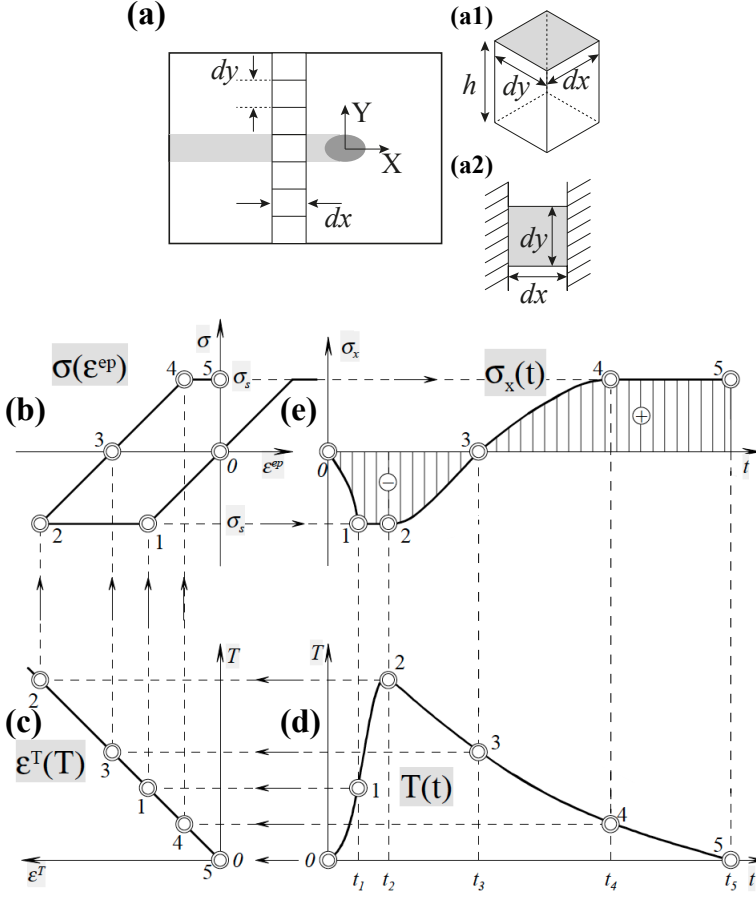
Figure 2.7: Transient longitudinal stress development during welding. Adapted (with permission) from reference [25].

Consider a small element ($dx.dy.h$) close to the fusion boundary as shown in Figure 2.7 (a1). It is assumed that that the deformation in the welding direction (x-direction) is negligible in comparison to the deformation in the transverse direction (y-direction). This assumption is reasonable since the thermal gradient is higher in the transverse direction than the longitudinal direction (x-direction). This means that the constraint is higher in the x- direction due to the surrounding cold material than in the y-direction. The idealized one dimensional case is shown in Figure 2.7 (a2). Here, in the x-direction the strain, $\epsilon_x = 0$, $\sigma_x \neq 0$ whereas there is no constraint in the y-direction, *i.e.* $\epsilon_y \neq 0$ and $\sigma_y = 0$.

Consider the thermal cycle shown in Figure 2.7 (d) for the the element shown in Figure 2.7 (a1). At time t_1, the element undergoes heating leading to thermal strain (ϵ^T) corresponding to point 1 in the Figure 2.7 (c). The expansion is constrained by the surrounding cold material leading to compressive longitudinal stress (point 1), in the

stress-strain curve shown in Figure 2.7 (b). Stress development as function of time ($\sigma_x(t)$) is shown in Figure 2.7 (e). On further increase in temperature (point 2 in the thermal cycle), yielding occurs, leading to a plastic compressive strain (ϵ^{ep}) and a compressive stress as shown in Figure 2.7 (b). During the cooling cycle (after point 2 in the thermal cycle), there is unloading and both the elastic strain and stress reduces to zero (point 3 in the stress-strain diagram and $\sigma_x(t)$ curve. On further cooling (point 4 in the thermal cycle), the contraction of the element is constrained by the surrounding material and as a result, tensile strain and stress are developed as shown in Figures 2.7 (b) and 2.7 (c). At this point, yielding starts and plastic deformation begins (point 4 onwards). At room temperature (point 5 in the thermal cycle), a tensile stress exits in the element (Figures 2.7 (b) and 2.7 (e)).

The transient development of transverse stress is similar to that of longitudinal stress. The typical distribution of longitudinal and transverse residual stresses in a weld upon cooling to room temperature are shown in Figure 2.8 [26]. To maintain the stress equilibrium, the tensile stresses at a location in a welded specimen must be compensated by compressive stresses elsewhere. Residual stresses can affect the mechanical performance of a welded joint. The presence of tensile residual stresses in a welded component affects the load bearing capacity and can lead to cold cracking. Residual stresses beyond the yield strength of a material are accommodated in the form of distortion.

(a) Longitudinal residual stresses
(b) Transverse residual stresses
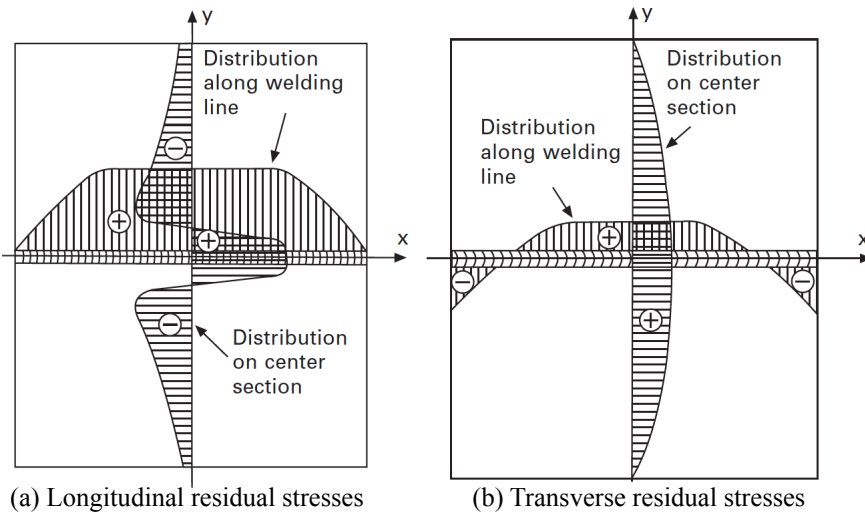
Figure 2.8: Longitudinal and transverse residual stress distribution in a weld. With permission from reference [26].

2.2.2 Microstructural features of the welded joint

A fusion weld comprises two major zones (Figure 2.6), namely the fusion zone (FZ) and the heat affected zone (HAZ) in which no melting occurs. Beyond the HAZ is the unaffected base metal (BM). In alloys, a zone surrounding the fusion zone, known as the partially melted zone, also exists. In this region, the peak temperature falls between the liquidus

and the solidus of the alloy. The fusion zone experiences melting and solidification and it's microstructure defines the quality of the weld. The solidification behaviour in the weld pool controls the size and morphology of grains, segregation and distribution of inclusions and porosity.

Most of the knowledge in weld solidification is derived from the principles of casting [27, 28]. However, temperature gradient and cooling rates are higher in welding. During solidification of a weld pool, grains nucleate on the existing base metal grains present at the fusion boundary. The grains grow such that the crystallographic orientation remains the same as the pre-existing grains at the fusion boundary. This condition is referred to as epitaxial growth. However, not all of these grains will be favourably oriented for continued growth [29]. Two primary factors control the growth of the weld metal grains:

1. The grains grow in a direction anti-parallel to that of the maximum heat transfer (or maximum temperature gradient). Since the temperature gradient is highest in the direction perpendicular to the solid-liquid interface, the resultant heat flow is also the highest in this direction. Thus, grains tend to grow in a direction perpendicular to the solid-liquid interface.

2. Grain growth generally occurs in a preferred crystallographic direction, which for cubic metals, is along the <100> directions [16, 29].

Thus, after the initial epitaxial growth, the grains whose preferred crystallographic direction are most closely aligned to the solid-liquid interface normal, *i.e.* maximum thermal gradient, will tend to grow. Grains with deviating directions are thus crowded out [27].

The shape and size of the weld pool influences the microstruture of the weld metal since the primary grains tend to grow in a direction perpendicular to the fusion boundary [16]. Both shape and size of the weld pool depend strongly on the thermophysical properties of the material and the welding parameters. With increasing heat source travel speed, the weld pool shape changes from an elliptical to a teardrop shape. Figure 2.9 depicts schematically the various shapes of the weld pool along with the respective grain morphologies. In the case of a teardrop shape of the weld pool, the direction of the thermal gradient does not change and the solidifying grains from the fusion boundaries impinge at the weld centreline. In the case of an elliptically shaped weld pool, the direction of the thermal gradient changes continuously towards the heat source travel direction. As a result, the solidifying grains also tend to continuously align towards the thermal gradient direction.

(a) Elliptical   (b) Teardrop
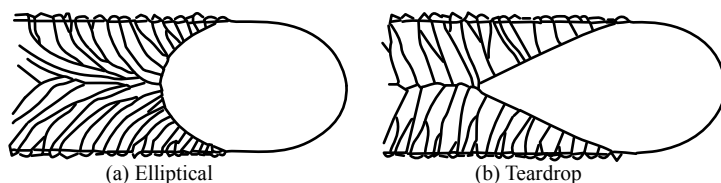
Figure 2.9: Different weld pool shapes and respective grain morphologies. With permission from reference [30].

Depending upon the location and thermal gradient in the weld pool, the weld metal microstructure can consist of planar, cellular, columnar dendritic or equiaxed dendritic

features. In addition to the local thermal gradient, these features are governed by constitutional supercooling in which the local liquidus temperature falls below the equilibrium liquidus temperature due to compositional variations (gradient). Hereafter, constitutional supercooling is described in more detail.

Constitutional supercooling

Consider the phase diagram shown in Figure 2.10 (a). As solidification begins, the liquid composition at the interface C_L is equal to the bulk composition C_o while the solid composition is kC_o. Here, k is the equilibrium partition coefficient and is defined as the ratio of solute composition in the solid and the liquid at a given temperature (C_S/C_L). As solidification proceeds, the solid rejects solute into the solid-liquid interface which must be transported away by diffusion and/or convection in the liquid [29].

In welding, the interface growth rate is high and therefore the solute rejected at the interface does not have time to mix completely with the remaining liquid by diffusion and/or convection (bulk fluid flow). As a result, a solute boundary layer develops ahead of the interface in the liquid (assuming $k < 1$). The local liquidus temperature drops and a gradient in the liquidus temperature develops. Both the compositional and temperature profile in the liquid is shown in Figures 2.10 (b) and 2.10 (c).

(a) (b) (c)
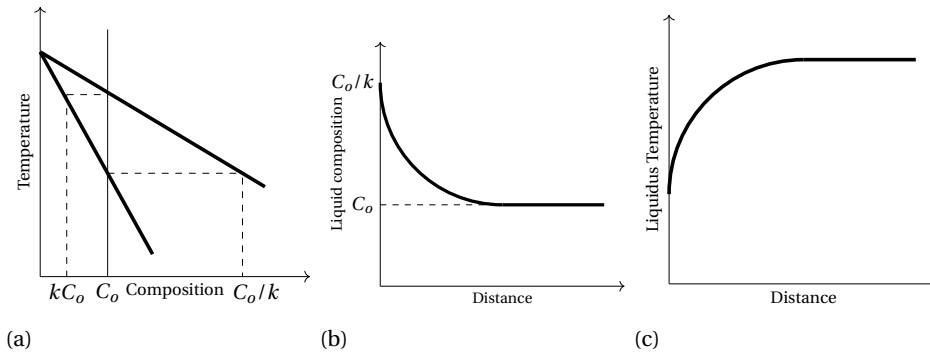
Figure 2.10: Schematic illustration showing (a) A phase diagram indicating solute enrichment in the liquid, (b) solute composition in liquid ahead of the solid-liquid interface and (c) liquidus temperature variation near the solid-liquid interface due to solute enrichment.

Depending upon the liquidus temperature gradient (dT_L/dx) and the actual temperature gradient (dT_a/dx) ahead of the solid-liquid interface, the following two cases can exist. In the first case, $dT_a/dx > dT_L/dx$. This case is shown schematically in Figure 2.11 (a). As the planar interface grows, protrusions can develop due to inclusions and/or competitive grain growth (<100> easy direction growth). When the actual temperature (T_a) is higher than the liquidus temperature such perturbation remelts as shown in the inset of Figure 2.11 (a). In such a case, the planar interface will remain stable. In the second case, $dT_a/dx < dT_L/dx$. In this case, any perturbation that forms ahead of the interface remains stable since the actual temperature is below the liquidus temperature (Figure 2.11 (b)). The planar interface breaks down and different substructures can form
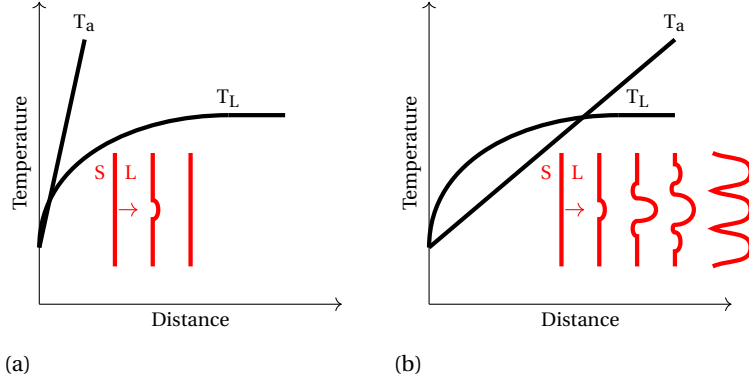
Figure 2.11: Schematic illustration showing (a) stability of planar interface and (b) breakdown of the planar interface due to constitutional supercooling.

as shown in the inset of Figure 2.11 (b) and Figure 2.12. This condition is known as constitutional supercooling or constitutional undercooling. This situation is frequently observed in welding and often used to describe the microstructural features of the weld. The condition for constitutional supercooling is given by equation 2.1:

$$\frac{dT_a}{dx} < m_L \frac{dC_L}{dx},\tag{2.1}$$

where, m_L is the liquidus slope. Now, the rate of solute rejection from the solidifying liquid must be equal to the rate of solute diffusion due to the concentration gradient in the liquid (dC_L/dx). This is given by equation 2.2

$$R(C_L - C_o) = -D_L(\frac{dC_L}{dx}),\tag{2.2}$$

where, C_L is the liquid concentration at the interface, R is the interface growth rate and D_L is the solute diffusion coefficient in the liquid. At steady state, $C_L = C_o/k$ [31]. The condition for constitutional supercooling is then given by equation 2.3 as:

$$\frac{G}{R} < -\frac{m_L C_o (1-k)}{k D_L}\tag{2.3}$$

or,

$$\frac{G}{R} < -\frac{\Delta T_o}{D_L},\tag{2.4}$$

where, G is the actual temperature gradient (dT_a/dx), ΔT_o is the equilibrium solid-ification temperature range of the alloy. As the degree of undercooling increases, the interface morphology changes from planar to cellular to dendritic. Schematic Figure 2.12 shows the effect of G and R on the substructure formation. The shaded region repre-sents the common morphologies experienced in welding [16, 29, 31, 32]. As the thermal gradient decreases from the fusion boundary towards the weld centreline, the extent of

constitutional supercooling increases. This promotes the formation of a dendritic mircostructure along with the presence of microsegregation. Figure 2.13 shows a schematic of the typical solidification morphologies observed in the weld metal region as a function of G_L, R and alloy content. In general, as the alloy content increases, the extent of the constitutional supercooling increases and dendritic morphology may also exist near the weld centre.

2
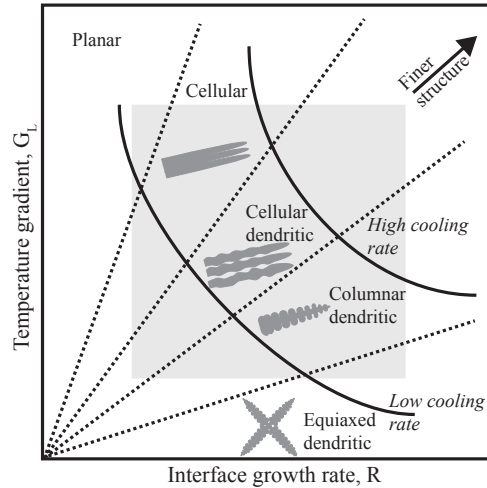
Figure 2.12: Schematic showing how interface morphology changes with temperature gradient and interface growth rate. The shaded region shows typical weld microstructural morphologies. Adapted (with permission) from reference [32].
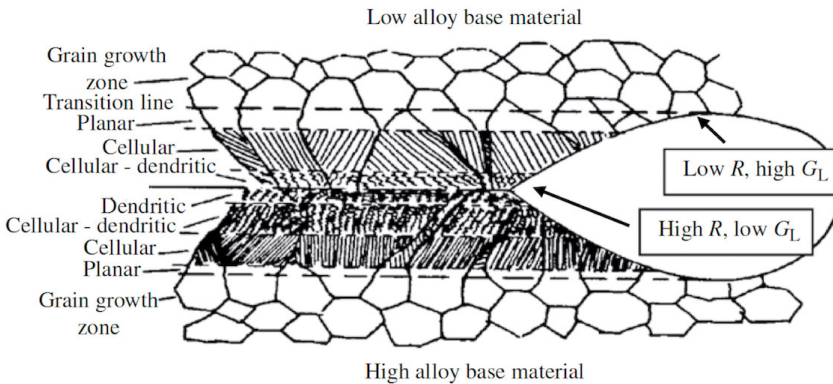
Figure 2.13: Schematic showing various types of morphology in the weld metal region as a function of G_L, R and alloy content. With permission from reference [33].

2.3 Solidification cracking/hot cracking[‡]

Solidification cracks, also referred to as hot cracks or hot tears in casting, are intergranular or interdendritic cracks that occur in constrained solidification conditions. Casting and welding are common examples in which a constrained solidification condition is present. Solidification cracking usually involves the presence of liquid films at grain boundaries in the fusion zone. Liquid films may also exist in the heat affected zone or the partially melted zone and can lead to another form of cracking known as liquation cracking. Figure 2.14 shows an example of solidification cracking and liquation cracking near the weld centreline and fusion boundary, respectively [34].
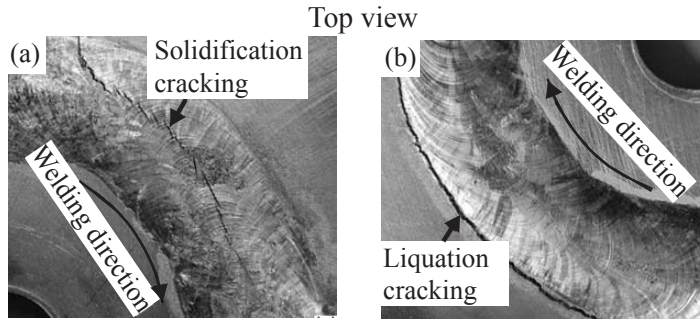
Figure 2.14: (a) Solidification cracking and (b) liquation cracking during circular patch welding of Al alloys. With permission from reference [34].

Non-uniform thermal expansion and contraction during welding leads to complex stress patterns in and around the welds. These stresses arise due to solidification shrinkage, thermal contraction, restraint and phase transformation. Figure 2.15 shows a schematic of the mechanism of solidification cracking [35]. The mushy region (two phase region) is separated by the liquidus (T_L^*) and solidus (T_S^*) isotherms with the heat source moving towards the right. At the trailing edge of the mushy region, *i.e.* when the solid fraction approaches 1, there are still liquid films present at the weld centreline. These films accumulate the tensile strain that develops due to the solidification shrinkage (liquid to solid phase change), thermal contraction of the solidified dendrites and the surrounding restraint. If the strain exceeds a threshold value of the material, solidification cracking occurs. Two fundamental factors generated by the weld thermal cycle are responsible for solidification cracking. The first is the restraint which is usually the mechanical or thermal stresses/strains and the second is the solidifying microstructure. It is the complex interaction of these two factors that leads to solidification cracking. Figure 2.16 outlines the various aspects that affect these two fundamental factors [36]. These aspects are discussed in the next section.

[‡]As per the American Welding Society (AWS), a hot crack is defined as a crack that forms at temperatures near the completion of solidification [32]. Often, cracks that occur after solidification such as ductility-dip-cracks are also considered to fall under the ambit of hot cracks. In this thesis, hot cracks or solidification cracks refer to the cracks that occur before solidification is complete, *i.e.* liquid films are still present. Although the term solidification cracking is preferred in the thesis, hot tearing or hot cracking are also used interchangeably in some instances.
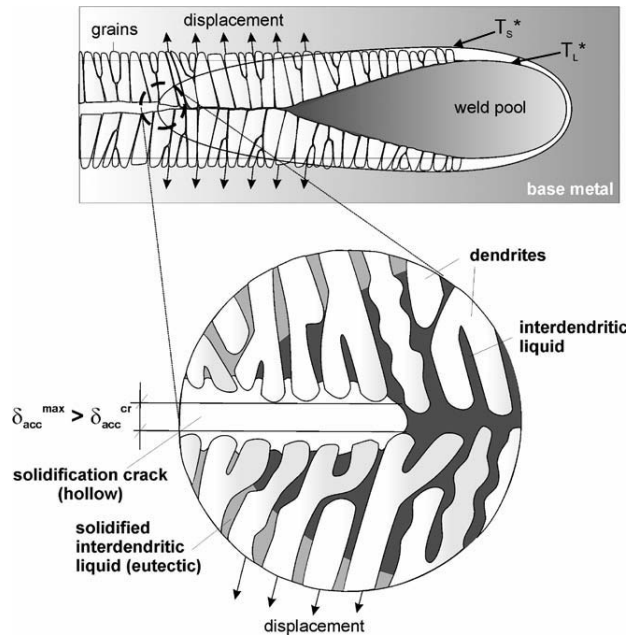
Figure 2.15: (a) Schematic showing the mechanism of solidification cracking. With permission from reference [35].
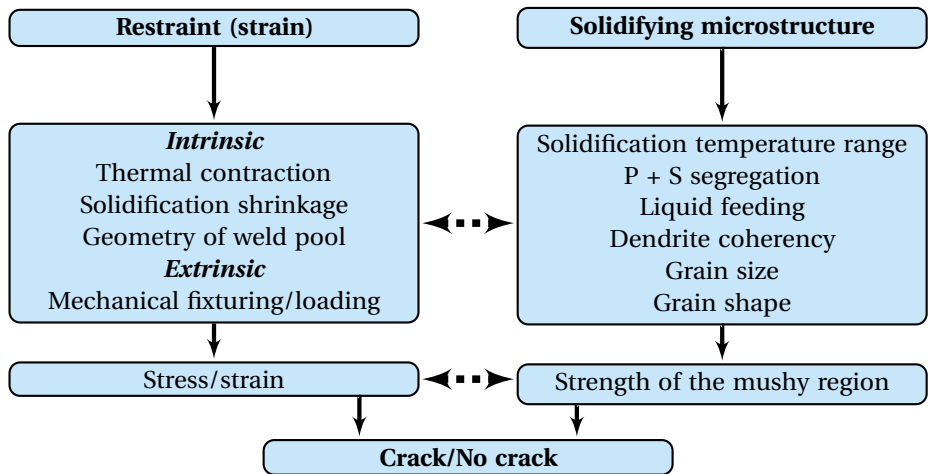
Figure 2.16: Fundamental conditions leading to weld solidification cracking. Adapted from references [30] and [36].

2.3.1 Factors contributing to solidification cracking

Firstly, the thermo-mechanical (or restraint) aspects that affect the solidification cracking susceptibility are discussed, followed by the metallurgical aspects.

Thermo-mechanical aspects

Upon solidification of a weld pool, non-uniform thermal contraction, solidification shrinkage and external fixturing (clamping) leads to the presence of tensile stresses/strains. If the local stress exceeds the threshold strength of a material, failure occurs. Consequently, a threshold stress (and hence strain), imposed on the solidifying metal, is assumed to be the cause for solidification cracking [§]. Over the period of last five decades, various theories focusing on critical strain, critical stress and critical strain rate based criteria have been proposed.

Strain based criteria: The strain based theory was first proposed by Pellini [37] in the 1950s for hot cracking in castings. This theory has been extended to weld solidification cracking and states that cracking occurs due to the rupture of liquid films that persist until the last stage of solidification. For liquid films to rupture, a critical amount of tensile strain needs to be present which is localized at the intergranular liquid film. The amount of strain depends upon the duration for which the liquid film persists, which in turn is affected by the solidification temperature range and the local cooling rate. This theory provided a qualitative physical explanation of the solidification cracking. Later on, Clyne and Davies [38] considered the mushy zone (or the two phase region) based on the fraction of solid (f_S). In the mushy zone, when $0.4 < f_s < 0.9$, any opening at the dendritic boundaries can be easily compensated by the remaining liquid; this is often referred to as the bulk liquid feeding or relaxation zone [¶]. In the brittle zone, when $0.9 < f_s < 0.99$, a crack cannot be healed by the remaining liquid due to a low permeability. They defined a cracking sensitivity coefficient (CSC) as the ratio t_v/t_r, where, t_v is the time spent in the vulnerable zone (*i.e.* $0.9 < f_s < 0.99$) and t_r is the time spent in the feeding or relaxation zone (*i.e.* $0.4 < f_s < 0.9$). Cracking susceptibility increases if the CSC is high. For determining the cracking susceptibility, the time spent in the crack susceptible regime (t_v) has more influence since the stresses/strains begin to accumulate at the grain boundary liquid films.

Building upon the work of Pellini, Prokhorov [41] considered the mushy zone as a single entity and defined its ductility as solidification occurs. During solidification, there is a loss in ductility of the mushy region. The temperature range over which ductility decreases is referred to as brittle temperature range (BTR). The BTR usually falls within the solidification temperature range, however, it can extend to temperatures below the solidus due the presence of liquid films at the grain boundaries, which form as a result of solute segregation and a drop in local solidus temperature. Based on the ductility curve (Figure 2.17), Prokhorov defined a critical amount of strain after which cracking occurs. Strain starts to accumulate as solidification begins and solidification cracking occurs if

---

[§]It is not yet proven beyond doubt that a critical strain rate is responsible for cracking. In the author's viewpoint, a higher strain rate facilitates the necessary minimum strain required for cracking to be reached while the grain boundary liquid films exist.

[¶]When $f_s < 0.4$, free flow of liquid is assumed.
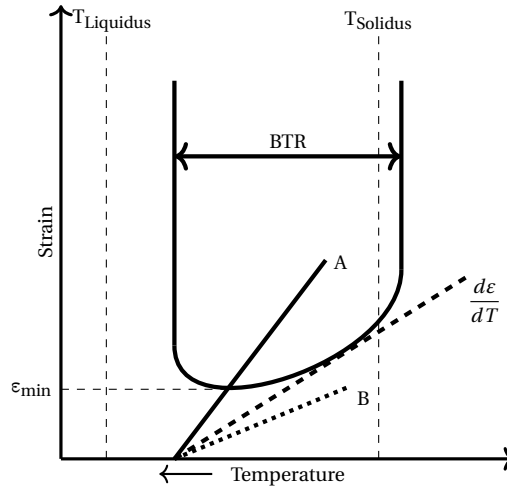
Figure 2.17: Schematic showing ductility curve and Brittle Temperature Range (BTR). Adapted from references [39, 40].

the total accumulated strain (line A) exceeds the ductility limit (ε_{min}), *i.e.* the line A is steeper than the critical strain tangent. If the the accumulated strain remains below ε_{min}, solidification cracking does not occur. The minimum ductility (ε_{min}) for Al alloys varies between 0.1-0.5 % [42] and 2-5 % for plane carbon steels [43].

The drawback of this theory is that strain localisation at the liquid films is not considered.

Stress based criteria: The stress-based theory assumes that cracking occurs if the applied or induced stress exceeds a certain threshold stress of the semi-solid material. In 1970s, Chihoski [44] described the nature of dynamic transverse stresses surrounding the weld pool. Later on, in 1990s, Zacharia [45] used the stress based approach to describe the thermo-mechanical behaviour in the weld pool vicinity. The model showed that at a certain distance behind the weld pool, the nature of the stresses in the mushy region change from compressive to tensile. If the temperature at which tensile stresses start to develop is above the effective solidus temperature (T_E), *i.e.* a network of liquid films exists, solidification cracking may occur. Figure 2.18 shows a schematic representation of the dynamic relationship of stresses near the weld pool.

The model was further verified based on welding experiments on 316 stainless steel sheets using an external predefined tensile load.
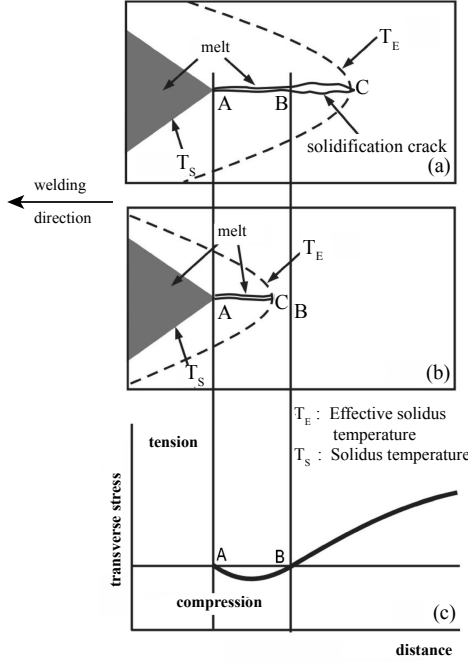
Figure 2.18: Nature of transverse stresses behind the weld pool. (a) the effective solidus temperature behind the weld pool is in the region where tensile stress exists, which can lead to solidification cracking, (b) the effective solidus temperature (T_E) is in the region where compressive stress exists, (c) schematic of transverse stress behind the weld pool. With permission from reference [46].

Strain rate based criteria: Following Prokhorov's work [39, 41], a strain-rate based criteria is nowadays widely accepted as the limiting factor that leads to cracking. To avoid solidification cracking, the semi-solid material needs to accommodate the tensile strains *via* appropriate plastic deformation, interdendritic liquid feeding, structure rearrangement and diffusion-aided creep. These processes require sufficient time and therefore cracking occurs if the strain rate exceeds a certain threshold [47]. From the ductility curve shown in Figure 2.17, strain imposed on the mushy region can be related to strain rate (8.2) by:

$$\frac{d\varepsilon}{dT} = \frac{d\varepsilon}{dt}\frac{dt}{dT}. \tag{2.5}$$

It follows from Prokhorov's work that a combination of a minimum local strain and local strain rate is needed for initiation of a solidification crack. The effect of the local strain rate on the minimum strain required for cracking depends on the nature of the ductility curve, *i.e.* whether the minimum ductility is towards the liquidus temperature or the solidus temperature.

Welding experiments of Matsuda *et al.* [48] and other more recent studies [49, 51, 52], show the strain-rate based dependency of solidification cracking.

Metallurgical aspects

Metallurgical aspects that have been known to affect the solidification cracking suscepti-
bility of weld metals include [30, 36] (i) the solidification temperature range, (ii) the back
filling capacity, (iii) the dendrite coherency, (iv) the surface tension of the grain boundary
liquid, and (v) the grain structure. These factors are directly or indirectly affected by the
weld metal composition.

Solidification temperature range   From the strain based theory by Pellini [37], it follows
that the liquid film life is dependent on the actual solidification temperature range of
the alloy in question. The brittle temperature range (BTR) is also influenced by the
solidification temperature range. Generally, with a wider BTR, an alloy has a higher
susceptibility to solidification cracking [32, 36]. The actual solidification temperature
range is influenced by impurity elements; *e.g.* sulphur or phosphorus in steels are known
to increase the range tremendously. Figure 2.19 shows the effect of various alloying
elements on the solidification temperature range of carbon and low-alloy steels [30].
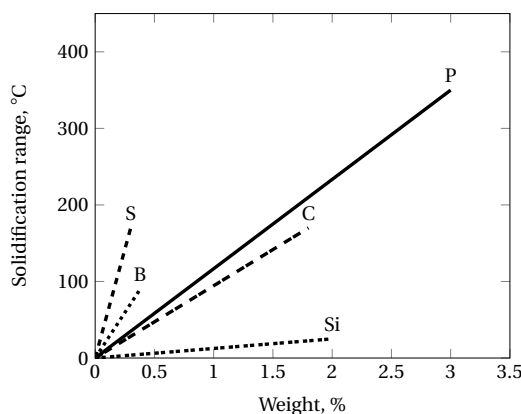
Figure 2.19: Effect of alloying elements on the solidification temperature range of carbon and low-alloy steels.
Replotted (with permission) from reference [30].

A small amount of sulphur increases the solidification temperature range drastically
and can push the solidus temperature down to 1261 K by forming an Fe-FeS eutectic
[53]. Similarly, microsegregation of phosphorus can lead to the formation of Fe-Fe$_3$P at
1321 K [53]. The extended solidification temperature range allows the existence of liquid
films at the interdendritic or grain boundaries and renders the mushy region susceptible
to cracking. It is often preferred to form MnS instead of FeS for two reasons. Firstly,
MnS forms at a higher temperature and lowers the amount of available S in the liquid
and secondly, FeS forms continuous liquid films at the grain boundaries while MnS
forms mostly as globular discontinuous particles [30, 32]. However, if the S content is
high (>0.05 wt. %), MnS can also form continuous films, increasing the susceptibility to
cracking [32].

The mode of solidification in stainless steels is well known to affect the solidification
cracking tendency. For instance, δ ferrite has a higher partition coefficient for S, P than

austenite and therefore steels in which solidification begins with δ ferrite are more resis-
tant to cracking [53]. Lundin *et al.* [54] reported that steels containing even 0.35 wt.%
S are weldable if the solidification mode remains ferritic. For austenitic stainless steels,
it is recommended that S and P content should be below 0.005 wt.% and 0.006 wt.%,
respectively [55].

Dendrite coherency   At high temperature and within the solidification temperature
range, the amount of liquid is high and therefore the solidifying dendrites are surrounded
by liquid. From a particular temperature or fraction of solid (dependent on the alloy), a
rigid network is formed and the solid structure is able to transmit stresses. The tempera-
ture at which the rigid network is formed is known as the coherency temperature [32, 56].
Figure 2.20 shows a series of micrographs during a controlled solidification experiment of
succinonitrile-acetone [56]. At $t = 30$, when the fraction of solid (f_s) is 0.82, the dendrites
are still separated by continuous liquid films. Between $f_s = 0.82$ and $f_s = 0.94$, the dendrite
arms coalesce and only isolated liquid droplets remain. At higher solid fraction, there is
minimal susceptibility to solidification cracking. When grain boundaries are involved, the
intergranular coalescence temperature is generally low compared with the intragranular
coalescence temperature. A decrease in intergranular coalescence temperature depends
on the grain boundary energy and the solid-liquid interfacial energy [56, 57]. In general,
an alloy is vulnerable to solidification cracking in the solid fraction range, $0.94 < f_s < 1$
[56].

(f) t = 1500s (e) t = 210s (d) t = 75s   (c) t = 30s   (b) t = 10s   (a) t = 0s

   $f_S = 0.98$ $f_S = 0.97$ $f_S = 0.94$ $f_S = 0.82$ $f_S = 0.70$ $f_S = 0.00$
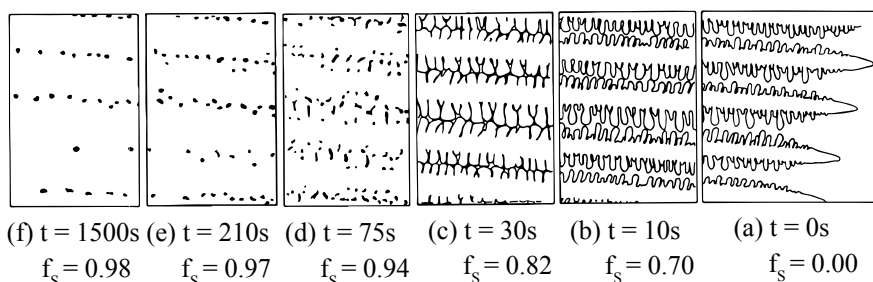
Figure 2.20: Series of micrographs as solidification progresses. (a)-(b) Liquid feeding is relatively easy, (c)
continuous liquid films are present and liquid feeding is difficult, (d) liquid films transforms to droplets and a
solid network is formed, (e)-(f) only isolated liquid droplets remain as solidification completes. With permission
from reference [58].

The shrinkage-brittleness theory proposed by Pumphrey and Jennings [59] is also
based upon the concept of coherency temperature. It says that cracking occurs when
there is some extent of coherency in the mushy region, *i.e.* within an effective temperature
range which is below the solidification temperature range. Figure 2.21 illustrates the role
of coherency temperature (and composition) on susceptibility to solidification cracking.

Surface tension   Surface tension or interfacial energy affects the coherency temperature
and therefore has a role in solidification cracking. For example, Kujanpää *et al.* [60]
considered the effect of γ-γ and δ-δ interfacial energies on solidification cracking in
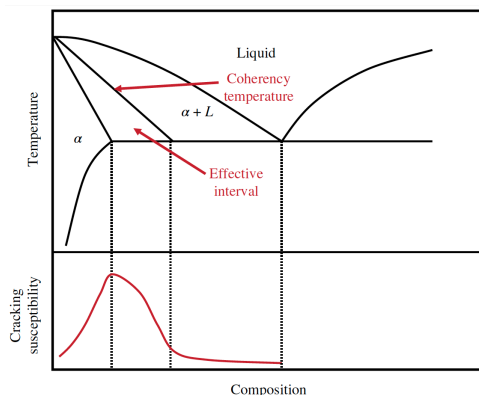
Figure 2.21: Solidification cracking susceptibility of an alloy based on shrinkage-brittleness theory. With permission from reference [32].

austenitic stainless steels. γ-γ grain boundaries have a lower interfacial energy compared to δ-δ or γ-δ. As a result, liquid easily wets the γ-γ boundaries resulting in an increased susceptibility to solidification cracking. Furthermore, elements like phosphorus and sulphur increases while oxygen reduces the grain boundary wetting [32].

Back-filling capacity   In order to avoid solidification cracking, adequate back-filling or interdendritic liquid feeding is necessary to compensate both the solidification shrinkage and thermal contraction. Early work of Feurer [61] considered the feeding of the mushy zone by the remaining liquid. Near the coherency temperature‖ and when the solid fraction is still high (between 0.94-0.99), liquid feeding tendency decreases due to both low permeability and the small amount of available liquid. If the rate of feeding is less than the rate of shrinkage, cracking occurs. Figure 2.22 schematically represents Feurer's [61] rate of feeding (ROF)-rate of shrinkage (ROS) model. The first physically based comprehensive model on hot tearing was reported by Rappaz, Drezet and Gremaud [58], also popularly known as the RDG model. Apart from solidification shrinkage considered by Feurer's model, they also included the effect of thermal contraction. Recently, Kou [62] in his model considered these effects at the grain boundary, where cracking generally occurs. Both these models are described in more detail later in this chapter.

Grain morphology   Grain morphology has a prominent effect on solidification cracking behaviour. Generally, solidification cracking occurs along grain boundaries. Grain boundaries are enriched with impurities (P, S) and provide an interface for liquid wetting. Welds with a fine grain size facilitates increased grain boundary area. Strain localization is thus prevented, resulting in improved resistance to solidification cracking [30, 32, 36].

Weld pool shape also affects the cracking behaviour. A teardrop shaped weld pool entails the coalescence or impingement of solidifying columnar grains at the weld centre-

---

‖Coherencey temperature refers to the temperature at which a given alloy begins to develop mechanical resistance [56].
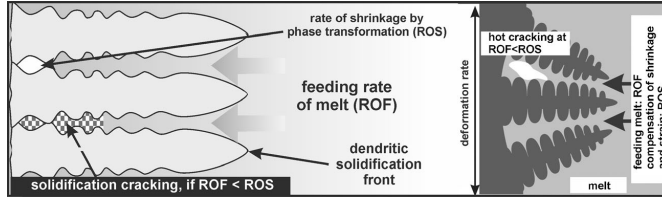
Figure 2.22: ROF-ROS model following Feurer's work [61]. With permission from reference [46].

line; this results in the formation of a thin film of liquid enriched with impurity elements. The strain is localized at the liquid films resulting in a higher likelihood of solidification cracking. In general, an elliptical weld pool shape offers better resistance to solidification cracking [32]. Alternating grain orientations using arc oscillation can also reduce the solidification cracking tendency [63]. Due to the alternating grain orientation, the direction of the crack is forced to change regularly which makes crack propagation difficult [63].

2.4 Recent models on solidification cracking

2.4.1 RDG criterion

Rappaz, Drezent and Gremaud proposed the first comprehensive and physically sound model of hot cracking [58, 64]. Unlike Feurer's model [61], contributions from both solidification shrinkage and tensile deformation were considered. Solidifying columnar dendrites were assumed to grow in one direction and were subjected to tensile deformation (rate) $\dot{\epsilon}$ in the perpendicular direction. Unidirectional liquid feeding was considered opposite to the growth direction. The schematic diagram (Figure 2.23) indicates the considered processes in the model. A steady-state mass balance equation was derived and the velocity of liquid was related to Darcy's law. The differential mass balance equation was integrated across the mushy zone and a liquid pressure drop was derived. Below a certain pressure in the liquid, $i.e.$ cavitation pressure, a void was assumed to nucleate. The maximum deformation rate ($\dot{\epsilon}_p$) sustainable by the mushy zone before hot cracking occurs is given by:

$$\int_{T_S}^{T_L} \frac{(\int f_s \dot{\epsilon}_p \, dT)(f_s)^2}{G(1 - f_S)^3} \, dT = \frac{\lambda_2^2}{180} \frac{G}{(1 + \beta)\mu} (p_m - p_c) - v_T \frac{\beta}{1 + \beta} \int_{T_S}^{T_L} \frac{(f_s)^2}{(1 - f_s)^2} \, dT, \quad (2.6)$$

where, T is the temperature, T_L and T_S are the liquidus and solidus temperature respectively, f_s is the fraction of solid, $\dot{\epsilon}_p$ is the maximum deformation rate perpendicular to the growth direction, λ_2 is the secondary dendrite arm spacing, G is the temperature gradient, β is the shrinkage factor, μ is the viscosity, p_m and p_c are the metallostatic pressure (at the dendrite tips) and the cavitation pressure (near the trunk of the dendrites) respectively and v_T is the solidification rate. The hot cracking susceptibility is proportional to $1/\dot{\epsilon}_p$, $i.e.$ a given alloy with a low threshold deformation rate $\dot{\epsilon}_p$ is more prone to hot cracking. The RDG criterion indicates that strain rate is the controlling factor for hot cracking. Based on a cavitation pressure of 2 kPa, susceptibility to solidification cracking was evaluated for Al-Cu alloys as a function of Cu content. The model predicts the known
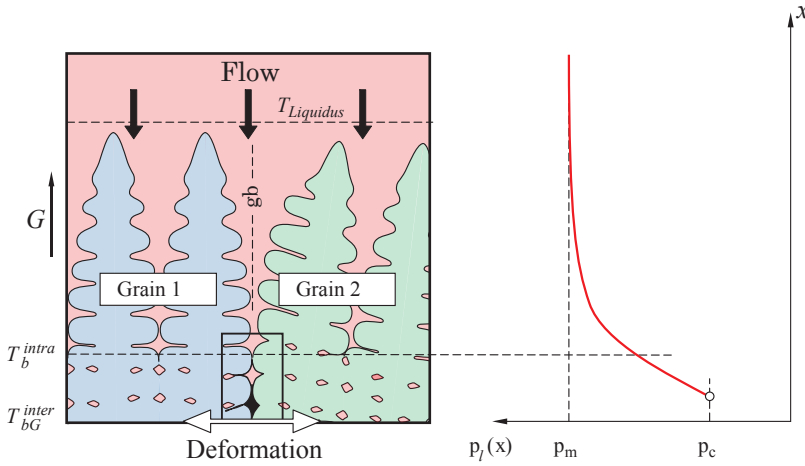
Figure 2.23: Schematic illustrating the RDG model. T_b^{intra} and T_{bG}^{inter} refer to the coalescence or bridging temperature of the dendritic and grain boundaries respectively. With permission from reference [64].

trend in Al-Cu alloys with a peak susceptibility to solidification cracking for Al-1.4 wt. % Cu alloy. Later on, Drezet *et al.* [65] applied the RDG criterion on steels for susceptibility to hot cracking during continuous casting, that agreed with the experimental observations.

In contradiction to the RDG model, Coniglio and Cross in their study [49] demonstrated that pore nucleation by liquid fracture is unlikely to occur and proposed a porosity-based crack initiation model. Pores were assumed to form based on hydrogen content and surface tension. Furthermore, a crack propagation model was proposed using a simplified mass balance approach in which crack advancement and liquid feeding compensate the deformation rate of the grain boundary liquid. Combining this with Darcy's law, a critical deformation rate was calculated and found to be in agreement with the experimentally measured local strain rate. A possible extension to this work includes determining the limiting strain rate at which a crack ceases to propagate.

Recently, Aucott *et al.* [50] studied *in-situ* solidification cracking during arc welding of steel using synchrotron X-ray radiography and post mortem micro-tomography. Isolated micro-cavities with size varying between 10–27 μm were observed at a strain of about 3.1 %. It was proposed that as the strain induced on the solidifying weld metal increases; the micro-cavities grow *via* coalescence to form micro-cracks, which propagate further.
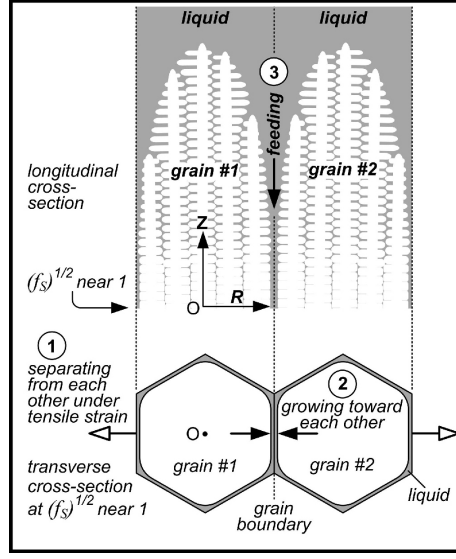
Figure 2.24: Mechanism of cracking along the grain boundary [62]. 1: Tensile deformation perpendicular to the grain boundary by the surrounding material, 2: Grains grow towards each other as solidification progresses, 3: Liquid feeding must compensate both the solidification shrinkage and tensile deformation. A high magnitude of $dT/d\sqrt{f_s}$ near $\sqrt{f_s} = 1$ leads to increased solidification cracking susceptibility. With permission from reference [66].

2.4.2 Kou's criterion

In 2015, Kou proposed a new criterion for cracking during solidification [62]. Unlike the RDG model in which the entire mushy zone was considered, Kou's criterion considers various events occurring at the grain boundary; the cracks are generally intergranular. The following aspects (Figure 2.24) are considered:

- Growth of grains towards each other as solidification progresses. At the same time tensile strain is exerted by the surrounding material.

- Liquid feeding occurs along the grain boundary to compensate both the shrinkage and tensile deformation.

- If the rate of separation exceeds the combined rate of growth and rate of liquid feeding, solidification cracking occurs.

Based on mass conservation at the grain boundary near $\sqrt{f_s} = 1$, the following criterion for cracking was derived:

$$\left\{ \underbrace{\frac{d\epsilon_{local}}{dt}}_{\text{separation}} > \underbrace{\sqrt{1-\beta}\frac{d\sqrt{f_s}}{dT}\frac{dT}{dt}}_{\text{growth}} + \underbrace{\frac{d}{dz}[(1-\sqrt{1-\beta}\sqrt{f_s})v_z]}_{\text{feeding}} \right\}_{\sqrt{f_s}\to 1}, \tag{2.7}$$

where, ϵ_{local} is the local tensile strain, β is the shrinkage factor, T is the temperature, z is the growth direction of grains and v_z is the liquid feeding velocity along the grain

boundary. According to equation 2.7, increasing $|dT/\sqrt{f_s}|$ near $\sqrt{f_s} = 1$ makes the right hand side of the equation smaller and the susceptibility to cracking increases. To assess the susceptibility, solidification curves of different Al-Cu alloy compositions were deduced based on the Scheil-Guliver solidification model [67, 68]. The assumption to neglect solid-state diffusion is reasonable since cooling rates in welding are very high. Accordingly, there is little time available for diffusion in the solid. An average steepness of the *T versus* $\sqrt{f_s}$ curve for f_s in the range of 0.87-0.94 was calculated to correlate with the known cracking tendency in Al-Cu alloys. For $f_s = 0.98$ and above, it is assumed that a rigid solid network forms to resist cracking.

Both the RDG and Kou criterion are sensitive to actual solidification curves ($f_s - T$) and depend on the accuracy with which the solidification path can be predicted, particularly for high solid fraction values.

2

2.5 Hot cracking tests

Hundreds of hot cracking tests have been developed and documented to assess the susceptibility of materials to hot cracking [69]. These tests are divided broadly into two categories, self restraint and externally loaded tests. Of these, the vast majority of tests are self restraint because these are in general easy to set-up and inexpensive [46, 70]. Some of the most common hot cracking tests are classified in Figure 2.25 and discussed further.
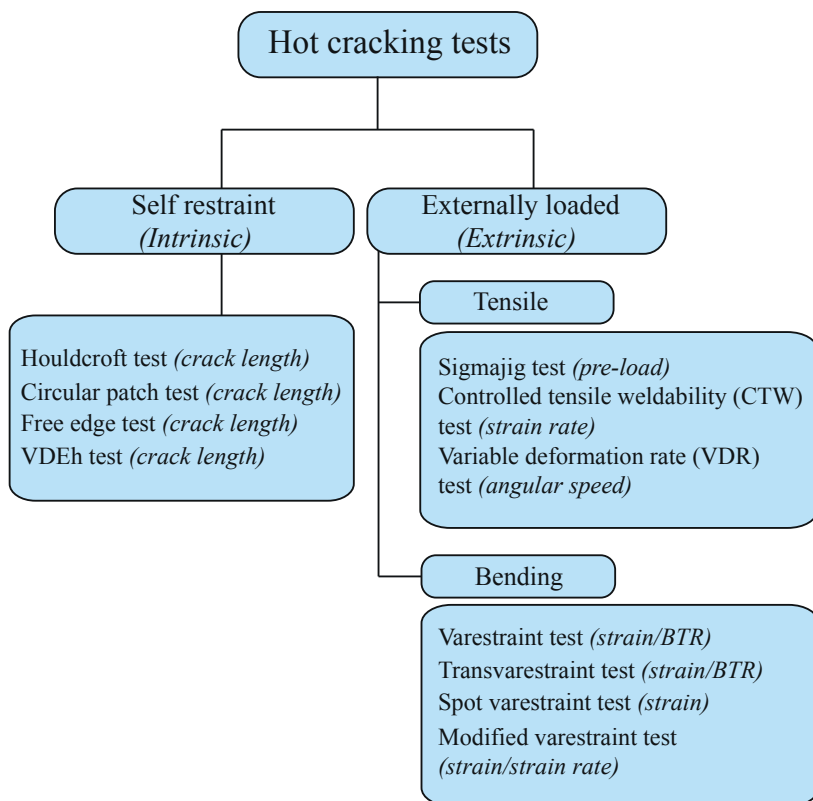
Figure 2.25: Classification of some common hot cracking tests. Loading condition and evaluation criterion for individual test are mentioned in brackets. BTR refers to brittle temperature range. For a more exhaustive list and description, please refer to references [46, 70–72].

2.5.1 Self restraint tests

In self restraint or intrinsic tests, the stresses and strains generated internally during welding are responsible for the initiation and propagation of solidification cracks. These tests provide an easy means to qualitatively rank alloys based on a, "go-no go" analysis. Accordingly, these tests are widely adopted in practice. Crack length serves as an index of susceptibility to cracking. The local conditions that leads to cracking (strain, strain rate *etc.*) are in general difficult to determine.

Houldcroft test   Also known as fishbone test, it was developed in 1955 by Houldcroft [73]. Typically, defined saw cut configurations in increasing length order (Figure 2.26 (a)) are made in a thin gauge material. Bead-on-plate welding is generally carried out in the direction of increasing slot depth. The progression of slots allows the dissipation of built up stresses (decrease in restraint) as the heat source moves further into the test piece. Solidification cracking occurs from the starting edge and continues along the centreline (Figure 2.26 (b)). Depending upon the threshold of the material, the crack continues to propagate through the entire width or ceases to propagate if the stresses/strains are released adequately.
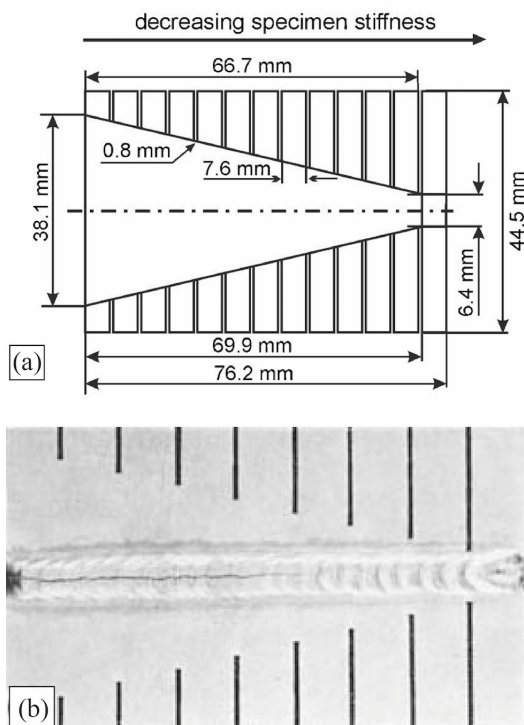
Figure 2.26: (a) Houldcroft test with defined saw depth configuration. With permission from reference [46], (b) solidification crack in an Al alloy. Taken from reference [30], with permission from the American Welding Society.

Circular patch test   In the circular patch test, a circular patch is removed from the test plate. The circular patch, referred to as inner piece in the schematic Figure 2.27 of the test set-up, is bolted together with the outer plate to a large base plate [34]. A small gap is maintained between the inner and outer plates. Different combinations of inner plate, outer plate and filler metal can be used [74]. Due to obstructed shrinkage upon welding provided by the constraints, tension is induced at the outer edge while compression is introduced at the inner edge. The tensile strain is perpendicular to the welding direction

and leads to liquation and/or solidification cracking (Figure 2.14). Crack length is used as an indicator for susceptibility to cracking.
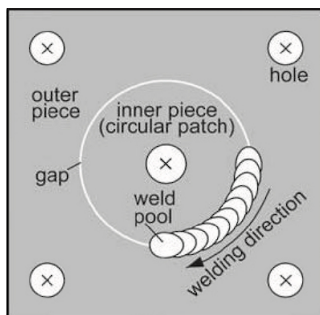
Figure 2.27: Circular patch test. With permission from reference [34].

Free edge test   In the free edge test [70], the amount of restraint is varied by the starting position of welding from the free edge (Figure 2.28). When welding is carried out close to the free edge, *i.e.* with less restraint, there is a high likelihood of solidification cracking. When the starting distance is increased, typically the crack length decreases and beyond a certain threshold starting position no cracking is observed.
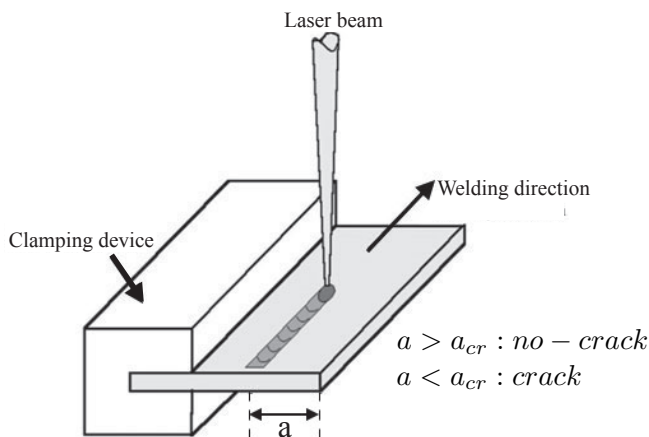
Figure 2.28: Free edge test. With permission from reference [70].

VDEh standard hot cracking test   In 2011, steel institute VDEh (Verein Deutscher Eisen-hüttenleute) developed a standard hot cracking test for laser welding of thin sheets used in the automotive industry [75]. This test is similar to the free edge test. Laser bead-on-plate welding is carried out on single sided clamped rectangular steel sheets with dimensions of 90 x 45 mm². The starting position is set at a distance of 3 mm from the free edge with the welding direction inclined 7° to the edge, as shown in the schematic Figure 2.29. In order to have standard welding conditions among the users of this test, a common procedure is adopted. At first, 90 % of the rated maximum laser power is used and the maximum welding speed with a stable keyhole is determined. This welding speed is then used with maximum laser power for the hot cracking test. Each test is repeated 10 times and the average crack length is determined. Crack length is used to assess the hot cracking susceptibility and rank different materials.
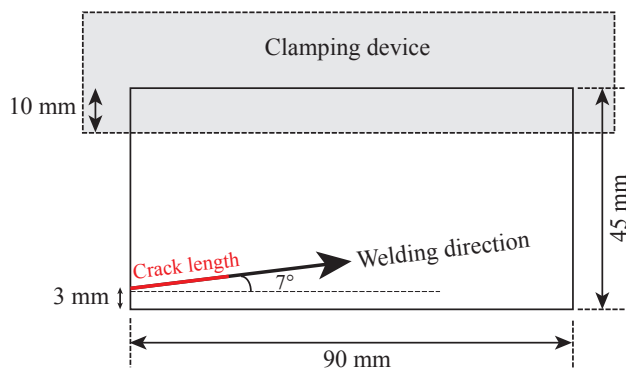
Figure 2.29: Schematic of the VDEh standard hot cracking test.

2.5.2 Externally loaded tests

Self restraint tests are inexpensive and easy to use, however, it is difficult to determine the critical local conditions that lead to cracking. These tests are primarily intended for a "go-no-go" analysis. In order to determine the global conditions such as pre-load, strain and/or strain rate that lead to cracking, several externally loaded hot cracking tests were developed. These test arrangements are in general expensive to build [70]. Some of the common tests are elaborated here.

Sigmajig test   The Sigmajig test developed by Goodwin [76] involves the application of transverse stress before welding by a movable specimen clamping system (Figure 2.30). Thin sheet metal of size 50 x 50 mm² are used. A critical pre-applied stress applied using the movable clamping system, is determined for cracking to occur. The test was able to reproduce the known cracking behaviour in type 304 and 316 stainless steels. Originally developed for autogenous gas tungsten arc welding, the test set-up is also used with laser or electron beam welding [46].
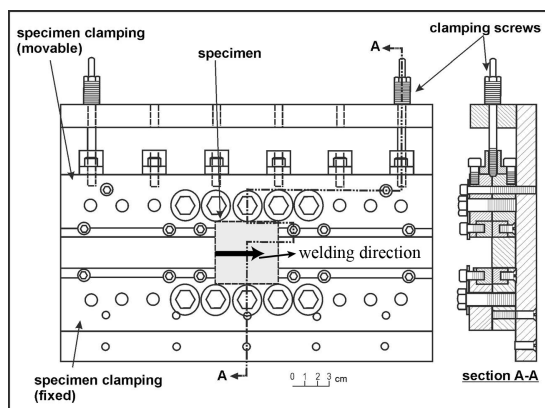
Figure 2.30: Schematic of the Sigma-jig test. With permission from reference [46].

Controlled tensile weldability test (CTW)   The test developed at the federal institute for materials research and testing in Germany (BAM) [46], allows the application of a tensile load before or during welding. A constant or a varied global strain rate can be applied to study the cracking behaviour. The test set-up allows the use of various welding processes, different loading directions, thick test specimens (up to 10 mm) and local displacement measurements [46]. A photo of the test set-up is shown in Figure 2.31.
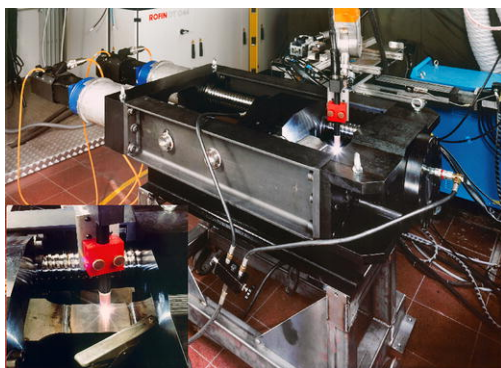
Figure 2.31: CTW test facility at BAM. With permission from reference [46].

Variable deformation rate test (VDR)   The continuously variable deformation rate test developed by Matsuda *et al.* [48] provides a critical deformation rate for the onset or propagation of solidification cracking. Figure 2.32 shows a schematic and working principle of the VDR test. Test plates are arranged in a T-joint configuration and a fillet weld is made using gas metal arc welding (GMAW). The horizontal plate is rotated around the centre of rotation with a constant angular velocity while welding is carried out towards the centre of rotation. The weld metal experiences deformation rate, the magnitude of

which is directly proportional to the distance from the centre of rotation. Accordingly, weld metal at the starting position experiences the maximum deformation rate and there is a high likelihood for the initiation of a solidification crack. Depending upon the alloy composition, a critical deformation rate (or angular velocity) can be determined below which the crack ceases to propagate [48].
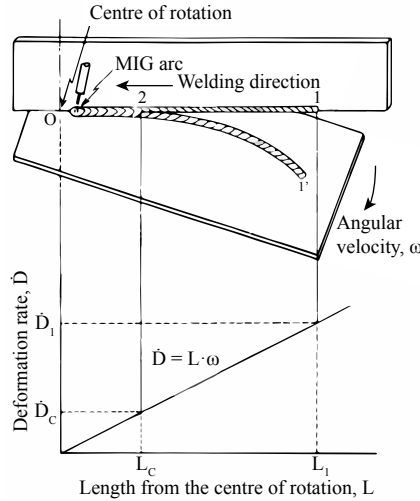
Figure 2.32: Schematic and working principle of VDR test. Taken from reference [48], with permission from the Joining and Welding Research Institute (Osaka University).

Varestraint test   The variable restraint or the Varestraint test was developed by Savage and Lundin [77]. In this test, an augmented strain is applied to the test specimen by applying bending load using a die block, as shown in the schematic Figure 2.33. Several variants of this test have been developed including a longitudinal type (primarily for heat affected zone and liquation cracking), a transverse type (for solidification cracking) and a spot type (for heat affected zone cracking) [78]. The augmented strain (ϵ) can be calculated by:

$$\epsilon = \frac{t}{2R + t},\qquad(2.8)$$

where, t is the sample thickness and R is the radius of the die. Generally, a threshold strain is determined for cracks to appear. Sometimes, the maximum crack length and total crack length (in the case of branching) are also used to rank alloys that crack at similar values of augmented strain. Due to the nature of the test, it is difficult to determine the local critical strain/strain rate that leads to cracking.
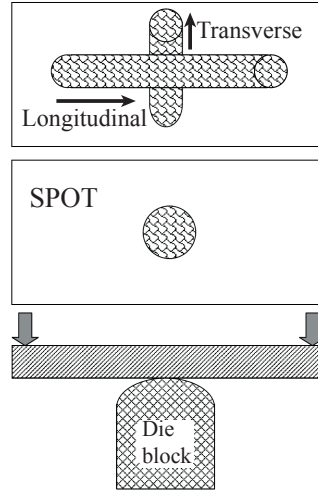
Figure 2.33: Different types of varestraint tests. With permission from reference [78].

2.6 Summary

In this chapter, brief descriptions of the common welding processes, residual stresses in welding and microstructural features of welds are provided. In addition, an introduction to solidification cracking phenomenon, factors that affect solidification cracking, recent models on solidification cracking and common hot cracking tests are discussed.

Over the last decades, strain rate based criteria for cracking have gained wide acceptance. This criteria is based on Prokhorov's work which was further elaborated by the work of Rappaz *et al.* [58] and Kou [62]. The prediction of these models depend upon the accuracy with which the strength of the mushy region can be determined, which in turn depends on several aspects of the solidifying microstructure (Figure 2.16). It is difficult to take into account all the aspects responsible for solidification cracking. As a result, all the present models provide cracking susceptibility (ranking of alloys) but are not yet capable of predicting whether cracking occurs or not under a given set of welding conditions. This thesis is focused on elucidating the interplay of the two fundamental factors (Figure 2.16), which are responsible for solidification cracking. In particular the following aspects are considered; restraint (strain imposed), solidification temperature range, dendrite coherency, interdendritic liquid feeding, solidification morphology and shape of the weld pool.

References

[1] M. Shome and M. Tumuluru, *Introduction to welding and joining of advanced high-strength steels (AHSS),* in *Welding and Joining of Advanced High Strength Steels (AHSS),* edited by M. Shome and M. Tumuluru (Woodhead Publishing, 2015) pp. 1 – 8.

[2] M. Tumuluru, *Resistance spot welding techniques for advanced high-strength steels (AHSS),* in *Welding and Joining of Advanced High Strength Steels (AHSS),* edited by M. Shome and M. Tumuluru (Woodhead Publishing, 2015) pp. 55 – 70.

[3] S. Aslanlar, *The effect of nucleus size on mechanical properties in electrical resistance spot welding of sheets used in automotive industry,* Materials & Design **27**, 125 (2006).

[4] Y. J. Chao, *Failure mode of spot welds: interfacial versus pullout,* Science and Technology of Welding and Joining **8**, 133 (2003).

[5] K. Yeung and P. Thornton, *Transient thermal analysis of spot welding electrodes,* Welding Journal (Miami) **78**, 1s (1999).

[6] E. M. van der Aa, M. Amirthalinham, J. Winter, D. N. Hanlon, M. J. M. Hermans, M. Rijnders and I. M. Richardson, *Improved resistance spot weldability of 3rd generation AHSS for automotive applications,* in *11th International Seminar on Numerical Analysis of Weldability* (Institute of Materials Science, Joining and Forming of Graz University of Technology, 2015).

[7] P. Eftekharimilani, E. M. van der Aa, M. J. M. Hermans and I. M. Richardson, *Microstructural characterisation of double pulse resistance spot welded advanced high strength steel,* Science and Technology of Welding and Joining **22**, 545 (2017).

[8] M. Amirthalingam, E. M. van der Aa, C. Kwakernaak, M. J. M. Hermans and I. M. Richardson, *Elemental segregation during resistance spot welding of boron containing advanced high strength steels,* Welding in the World **59**, 743 (2015).

[9] J. Frei and M. Rethmeier, *Susceptibility of electrolytically galvanized dual-phase steel sheets to liquid metal embrittlement during resistance spot welding,* Welding in the World **62**, 1031 (2018).

[10] A. Kochan, *Laser technology is key to new VW golf, Retrieved (29-01-2019) from: https://www.autonews.com/article/20031117/SUB/311170826/laser-technology-is-key-to-new-vw-golf* (2003).

[11] S. Webzell, *A wealth of welding options, Retrieved (29-01-2019) from: https://automotivemanufacturingsolutions.com/technology/a-wealth-of-welding-options* (2015).

[12] W. M. Steen and J. Mazumder, *Background to laser design and general applications,* in *Laser Material Processing* (Springer London, London, 2010) pp. 11–78.

[13] M. S. Brown and C. B. Arnold, *Fundamentals of laser-material interaction and application to multiscale surface modification,* in *Laser Precision Microfabrication,* edited by K. Sugioka, M. Meunier and A. Piqué (Springer Berlin Heidelberg, Berlin, Heidelberg, 2010) pp. 91–120.

[14] B. Aalderink, *Sensing, monitoring and control of laser based welding of aluminium sheets,* Ph.D. thesis, University of Twente (2007).

[15] G. Agarwal, H. Gao, M. Amirthalingam and M. J. M. Hermans, *In-situ strain investigation during laser welding using digital image correlation and finite element based numerical simulation,* Science and Technology of Welding and Joining **23**, 134 (2018).

[16] G. den Ouden and M. J. M. Hermans, *Welding technology* (VSSD, Delft, The Netherlands, 2009).

[17] J. Y. Lee, S. H. Ko, D. F. Farson and C. D. Yoo, *Mechanism of keyhole formation and stability in stationary laser welding,* Journal of Physics D: Applied Physics **35**, 1570 (2002).

[18] S. Nayak, E. Biro and Y. Zhou, *Laser welding of advanced high-strength steels (AHSS),* in *Welding and Joining of Advanced High Strength Steels (AHSS),* edited by M. Shome and M. Tumuluru (Woodhead Publishing, 2015) pp. 71 – 92.

[19] M. A. Omar, *Automotive joining,* in *The Automotive Body Manufacturing Systems and Processes* (Wiley-Blackwell, 2011) Chap. 3, pp. 107–176.

[20] K.-M. Hong and Y. C. Shin, *Prospects of laser welding technology in the automotive industry: A review,* Journal of Materials Processing Technology **245**, 46 (2017).

[21] D. Radaj, *Introduction,* in *Heat Effects of Welding: Temperature Field, Residual Stress, Distortion* (Springer Berlin Heidelberg, Berlin, Heidelberg, 1992) pp. 1–18.

[22] K. Masubuchi, *Chapter 3 - fundamental information on residual stresses,* in *Analysis of Welded Structures,* edited by K. Masubuchi (Pergamon, 1980) pp. 88 – 111.

[23] P. Withers and H. Bhadeshia, *Residual stress. part 2 – nature and origins,* Materials Science and Technology **17**, 366 (2001).

[24] A. R. Pyzalla, *Internal stresses in engineering materials,* in *Neutrons and Synchrotron Radiation in Engineering Materials Science* (Wiley-Blackwell, 2008) Chap. 2, pp. 21–56.

[25] A. Pilipenko, *Computer simulation of residual stress and distortion of thick plates in multi-electrode submerged arc welding. Their mitigation techniques,* Ph.D. thesis, Norwegian University of Science and Technology, Trondheim, Norway (2001).

[26] H. Murakawa, *13 - Residual stress and distortion in laser welding,* in *Handbook of Laser Welding Technologies,* Woodhead Publishing Series in Electronic and Optical Materials, edited by S. Katayama (Woodhead Publishing, 2013) pp. 374 – 398.

[27] S. David, S. Babu and J. Vitek, *Welding: Solidification and microstructure,* JOM **55**, 14 (2003).

[28] S. A. David and J. M. Vitek, *Correlation between solidification parameters and weld microstructures,* International Materials Reviews **34**, 213 (1989).

[29] T. J. Lienert, S. S. Babu, T. A. Siewert and V. L. Acoff, *ASM Handbook, Volume 06A - Welding Fundamentals and Processes* (ASM International, 2011).

[30] S. Kou, *Welding Metallurgy*, 2nd ed. (John Wiley & Sons, Inc., 2003) pp. 263–296.

[31] D. A. Porter, K. E. Easterling and M. Y. Sherif, *Phase transformations in metals and alloys*, 3rd ed. (CRC press, 2009).

[32] J. Lippold, *Welding Metallurgy and Weldability*, 1st ed. (John Wiley & Sons, 2014) pp. 84–119.

[33] K. Easterling, *Introduction to the Physical Metallurgy of Welding*, 2nd ed. (Butterworth-Heinemann, 1992) pp. 55–125.

[34] S. Kou, *Solidification and liquation cracking issues in welding,* JOM **55**, 37 (2003).

[35] V. Ploshikhin, A. Prikhodovsky, M. Makhutin, A. Ilin and H.-W. Zoch, *Integrated mechanical-metallurgical approach to modeling of solidification cracking in welds,* in *Hot Cracking Phenomena in Welds* (Springer Berlin Heidelberg, Berlin, Heidelberg, 2005) pp. 223–244.

[36] C. E. Cross, *On the origin of weld solidification cracking,* in *Hot Cracking Phenomena in Welds*, edited by T. Böllinghaus and H. Herold (Springer Berlin Heidelberg, 2005) pp. 3–18.

[37] W. S. Pellini, *Strain theory of hot-tearing,* Foundry **80**, 124 (1952).

[38] T. W. Clyne and G. J. Davies, *The influence of composition on solidification cracking susceptibility in binary alloy systems,* British Foundryman **74**, 65 (1981).

[39] N. N. Prokhorov and N. N. Prokhorov, *Fundamentals of the theory for technological strength of metals while crystallising during welding,* Transactions of the Japan Welding Society **2**, 205 (1971).

[40] T. Senda, F. Matsuda and G. Takano, *Studies on solidification crack susceptibility for weld metals with trans-varestraint test (2),* Journal of the Japan Welding Society , 48 (1973).

[41] N. N. Prokhorov, *The problem of the strength of metals while solidifying during welding,* Svar Proiz **6**, 5 (1956).

[42] K. Nakata and F. Matsuda, *Evaluations of ductility characteristics and cracking susceptibility of Al alloys during welding,* Transactions of JWRI **24**, 83 (1995).

[43] F. Matsuda, H. Nakagawa, H. Kohmoto, Y. Honda and Y. Matsubara, *Quantitative evaluation of solidification brittleness of weld metal during solidification by in-situ observation and measurement (report ii),* Transactions of JWRI **12**, 73 (1983).

[44] R. A. Chihoski, *The character of stress fields around a weld arc moving on an aluminum sheet,* Welding Journal **51**, 9s (1972).

[45] T. Zacharia, *Dynamic stresses in weld metal hot cracking,* Welding Journal (Miami, Fla) **73**, 164S (1994).

[46] T. Kannengießer and T. Böllinghaus, *Hot cracking tests - an overview of present technologies and applications,* Welding in the World **58**, 397 (2014).

[47] D. G. Eskin and L. Katgerman, *A quest for a new hot tearing criterion,* Metallurgical and Materials Transactions A **38**, 1511 (2007).

[48] F. Matsuda, H. Nakagawa, K. Nakata and H. Okada, *The VDR cracking test for solidification crack susceptibility on weld metals and its application to aluminum alloys,* Transactions of JWRI **8**, 85 (1979).

[49] N. Coniglio and C. Cross, *Mechanisms for solidification crack initiation and growth in aluminum welding,* Metallurgical and Materials Transactions A **40**, 2718 (2009).

[50] L. Aucott, D. Huang, H. Dong, S. Wen, J. Marsden, A. Rack and A. Cocks, *Initiation and growth kinetics of solidification cracking during welding of steel,* Scientific Reports **7: 40255** (2017).

[51] M. Wolf, T. Kannengieβer and T. Böllinghaus, *Determination of critical strain rate for solidification cracking by numerical simulation,* in *Hot Cracking Phenomena in Welds II*, edited by T. Böllinghaus, H. Herold, C. E. Cross and J. C. Lippold (Springer Berlin Heidelberg, Berlin, Heidelberg, 2008) pp. 77–92.

[52] A. Kromm and T. Kannengießer, *Influence of local weld deformation on the solidification cracking susceptibility of a fully austenitic stainless steel,* in *Hot Cracking Phenomena in Welds II*, edited by T. Böllinghaus, H. Herold, C. E. Cross and J. C. Lippold (Springer Berlin Heidelberg, Berlin, Heidelberg, 2008) pp. 127–145.

[53] V. Shankar, T. Gill, S. Mannan and S. Sundaresan, *Solidification cracking in austenitic stainless steel welds,* Sadhana **28**, 359 (2003).

[54] C. D. Lundin, C. H. Lee, R. Menon and V. Osorio, *Weldability evaluations of modified 316 and 347 austenitic stainless steels: Part i – preliminary results,* Welding Journal **67**, 46s (1988).

[55] F. Matsuda, S. Katayama and Y. Arata, *Solidification crack susceptibility in weld metals of fully austenitic stainless steels (report v) : Solidification crack susceptibility and amount of phosphide and sulphide in SUS 310S weld metals,* Transactions of JWRI **10**, 201 (1981).

[56] M. Rappaz and J. Dantzig, *Solidification*, 1st ed. (EFPL Press, 2009) pp. 538–540.

[57] N. Wang, S. Mokadem, M. Rappaz and W. Kurz, *Solidification cracking of superalloy single- and bi-crystals,* Acta Materialia **52**, 3173 (2004).

[58] M. Rappaz, J. M. Drezet and M. Gremaud, *A new hot-tearing criterion,* Metallurgical and Materials Transactions A **30**, 449 (1999).

[59] W. I. Pumphrey and P. H. Jennings, *A consideration of the nature of brittleness and temperature above the solidus in castings and welds in aluminum alloys,* Journal of the Institute of Metals **75**, 235 (1948).

[60] V. P. Kujanpää, S. A. David and C. L. White, *Formation of hot cracks in austenitic stainless steel welds – solidification cracking,* Welding Journal **65**, 203s (1986).

[61] U. Feurer, *Influence of alloy composition and solidification conditions on dendrite arm spacing, feeding, and hot tear properties of aluminum alloys,* in *Proceedings of the International Symposium on Engineering Alloys, Delft* (1977) pp. 131–145.

[62] S. Kou, *A criterion for cracking during solidification,* Acta Materialia **88**, 366 (2015).

[63] S. Kou and Y. Le, *Alternating grain orientation and weld solidification cracking,* Metallurgical Transactions A **16**, 1887 (1985).

[64] M. Rappaz and J. Dantzig, *Solidification*, 2nd ed. (EFPL Press, 2009) pp. 626–634.

[65] J. M. Drezet, M. Gremaud, R. Graf and M. Gaümann, *A new hot tearing criterion for steel,* Proceedings of the 4th European Continuous Casting Conference, IOM communications, Birmingham, UK , 755 (2002).

[66] J. Liu and S. Kou, *Effect of diffusion on susceptibility to cracking during solidification,* Acta Materialia **100**, 359 (2015).

[67] G. H. Gulliver, *The quantitative effect of rapid cooling upon the constitution of binary alloys,* Journal of the Institute of Metals **9**, 120 (1913).

[68] E. Scheil, *Bemerkungen zur schichtkristallbildung,* Zeitschrift für Metallkunde **34**, 70 (1942).

[69] G. Goodwin, *Test methods for evaluating hot cracking: Review and perspective,* Proceedings of the United States–Japan Symposium on Advances in Welding Metallurgy **1**, 59 (1990).

[70] N. Coniglio and C. E. Cross, *Towards establishment of weldability testing standards for solidification cracking,* in *Cracking Phenomena in Welds IV*, edited by T. Boellinghaus, J. C. Lippold and C. E. Cross (Springer International Publishing, Cham, 2016) pp. 37–66.

[71] C. Cross and N. Coniglio, *Weld solidification cracking: Critical conditions for crack initiation and growth,* in *Hot Cracking Phenomena in Welds II*, edited by T. Bölling-haus, H. Herold, C. E. Cross and J. C. Lippold (Springer Berlin Heidelberg, 2008) pp. 47–66.

[72] J. Lippold, *Welding Metallurgy and Weldability*, 1st ed. (John Wiley & Sons, 2014) pp. 343–371.

[73] P. T. Houldcroft, *A simple cracking test for use with argon-arc welding,* British Welding Journal **2**, 471 (1955).

[74] C. Huang and S. Kou, *Liquation cracking in full-penetration Al-Cu welds,* Welding Journal **83**, 50s (2004).

[75] VDEh, *SEP 1220-3: Testing and documentation guideline for the joinability of thin sheet of steel - Part 3: Laser beam welding*, edited by STAHL (2011).

[76] G. Goodwin, *Development of a new hot-cracking test—the sigmajig,* Welding Journal **66**, 33s (1987).

[77] W. F. Savage and C. D. Lundin, *The varestraint test,* Welding Journal **44**, 433s (1965).

[78] J. Lippold, *Welding Metallurgy and Weldability*, 1st ed. (John Wiley & Sons, 2014) pp. 345–347.

3

Experimental procedures and modelling methods

IN this chapter, experimental procedures including test materials, hot cracking test set-up, welding conditions, high-speed camera imaging, digital image correlation, high temperature microscopy and microstructural characterisation are described. In addition, modelling methods including a finite element (FE) thermo-mechanical model of welding and a phase field model for the solidification of a melt pool are also described. Procedures are followed and models employed in the subsequent chapters.

3.1 Materials selection

Two commercial advanced high strength steel (AHSS) sheets, a transformation-induced plasticity steel (TRIP) and a dual phase (DP) steel were selected for this work. These steels are widely employed in automotive car bodies [1] and hence make a good case for the present study. Both grades offer improved formability and crash-worthiness compared to conventional steel grades [2]. In general, AHSS grades can be described as 'multiphase', incorporating one or more 'hard' phases in a soft ferrite matrix.

The chemical composition, heat treatment, phase diagram and microstructure of both the steels are described in the next section.

3.1.1 Transformation-induced plasticity (TRIP) steel

The TRIP effect is attained when the austenite transforms into martensite upon deformation. TRIP steels with a fully austenitic structure have been known for more than five decades [3]. However, due to the high amount of expensive alloying elements (such as nickel) required to stabalise austenite, these steels could not be commercially exploited. In the late 1980s, Matsumura *et al.* [4, 5] demonstrated the TRIP effect in a low-alloy steel containing C 0.2, Mn 1-2 and Si 1-2 (all in wt. %). In addition to high strength (>600 MPa) and ductility (elongation to failure 25 %), the lean composition and low price has subsequently lead to its popularity, particularly in the automotive industry.

Table 3.1: Composition of the TRIP and DP steels (major alloying elements) used in this work (in weight %).

Elements, wt. %	C	Mn	Al	Si	Cr	P	S
TRIP	0.19	1.63	1.1	0.35	0.019	0.089	0.005
DP	0.15	2.3	0.03	0.10	0.56	0.01	≈ 0

In this work, cold rolled and galvanized steel sheets of thickness 1.25 mm were used. The composition of the steel is listed in Table 3.1. In addition to C, Mn is also an austenite stabaliser. Silicon is primarily added to suppress cementite precipitation during bainite formation. In the process, the remaining austenite is enriched with C and is retained in the final microstructure. However, an increase in the Si content beyond 0.5 wt. % reduces the galvanizability by forming silicon oxide [6]. Both Al and P also inhibit cementite formation and are added to partially substitute Si. P also stabalises ferrite by solute strengthening and addition of 0.1 wt. % increases the strength of ferrite by 75 MPa [7]. The typical heat treatment during cold rolling of TRIP steel is shown schematically in Figure 3.1. In the first stage, the steel strips are heated up to the intercritical regime, where they have a microstructure consisting of ferrite (α) and austenite (γ). During heating, dissolution of pearlite and carbide occurs to form austenite (above the A_{c1} temperature). The next step involves intercritical annealing (IA) in which the steel is held isothermally in the temperature range of 750-900°C. During this stage, the austenite is enriched with C and other alloying elements. However, the C content in the austenite is not enough to suppress martensite formation upon cooling and hence another heat treatment is required. The steel is rapidly cooled to an intermediate soaking temperature. During cooling, some pro-eutectoid ferrite may form. Due to fast cooling rates and alloying additions (Si/Al/P) pearlite formation is suppressed. After the fast cooling, the steel is held at this temperature. This stage is known as an isothermal bainitic transformation (IBT) treatment, where bainite formation occurs. As the transformation progresses, the remaining austenite becomes further enriched in C due to the suppression of cementite formation by the alloying elements (Si/Al/P). The last stage involves fast cooling to room temperature. Depending upon the alloying contents and heat treatment, the final microstructure consists of 60-70 % ferrite (α), 20-30 % bainite (α_β), 5-15 % retained austenite (γ_{RA}) and a small amount of martensite (α') (depending upon the martensite start temperature (M_s)) [8–10].

The pseudo binary, phase diagram of TRIP steel is shown in Figure 3.2. A commercial thermodynamic software, Thermo-Calc^{TM} with database TCFE7 was used for this purpose. The liquidus temperature of the TRIP steel is 1786 K and the equilibrium solidification temperature range is 50 K. The microstructure of the as received TRIP steel is shown in Figure 3.3. A two step colour-tint etching procedure, developed by De *et al.* [11] was followed. The etching reveals the retained austenite (γ_{RA}) as whitish, martensite as straw-coloured, bainite as dark and the ferrite matrix as tan coloured.

3.1.2 Dual Phase (DP) steel
Dual Phase (DP) steels consist of a soft ferritic matrix along with a hard martensitic second phase in the form of islands. A straightforward heat treatment cycle (intercritical
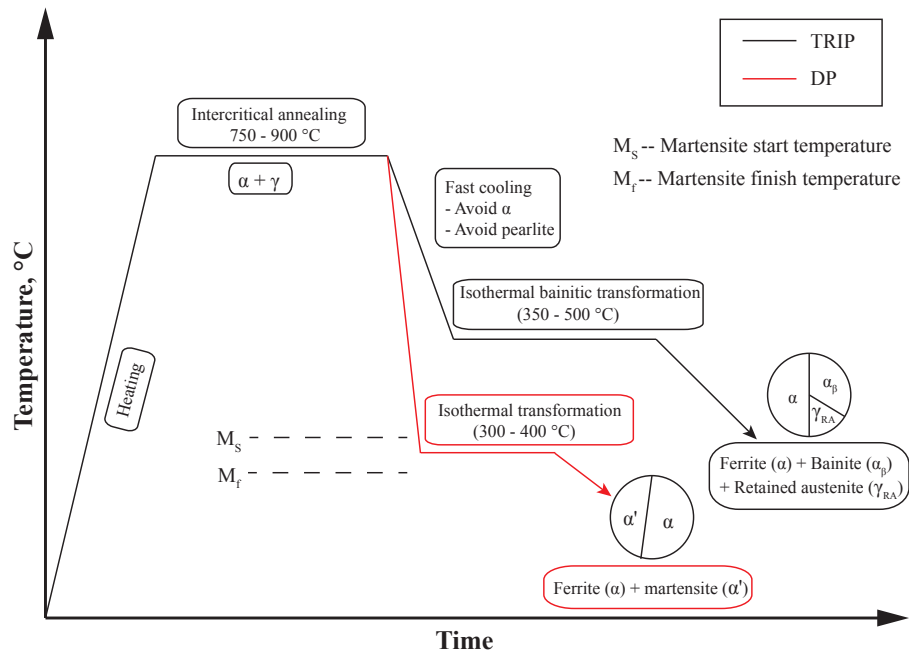
Figure 3.1: Typical heat treatment cycle fro TRIP and DP steels.

Figure 3.2: Pseudo binary phase diagram of TRIP steel used in the present work.
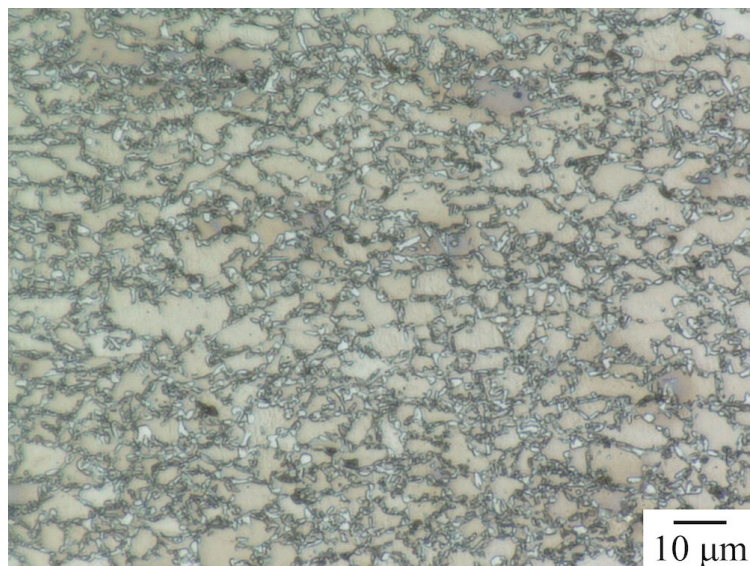
Figure 3.3: Optical micrograph of TRIP steel showing ferrite matrix with bainite (darker region). The bright spots are of retained austenite (γ_{RA}).

annealing followed by isothermal or continuous transformation below the M_s tempera-ture, shown in the schematic Figure 3.1) combined with a low alloying content provides very good mechanical properties. Due to this, DP steels are often employed in the auto-motive industry [1]. DP steels typically have a low yield ratio (yield strength to ultimate tensile strength) due to a combination of a soft ferritic phase and a hard martensitic phase [12, 13]. To achieve the desired microstructures, DP steels contain 0.06–0.15-wt. % C and 1.5–3 wt. % Mn (the former strengthens the martensite, the latter causes solid-solution strengthening in ferrite, and both stabilise the austenite), Cr and Mo (to retard pearlite or bainite formation), Si (to promote ferrite transformation), V and Nb (for precipitation strengthening and microstructure refinement) [12].

The composition of the DP steel sheets used in the present work is listed in Table 3.1 and the pseudo binary phase diagram is shown in Figure 3.4. The liquidus temperature of DP steel is 1786 K and the equilibrium solidification temperature range is 33 K. Figure 3.5 shows the microstructure of the as received steel. The etching procedure for the TRIP steel was repeated here.

Both the TRIP and DP steels undergo the similar phase transitions before solidification is complete. Solidification begins with the formation of the δ ferrite phase. δ ferrite continues to form until the peritectic phase transition, *i.e.* the austentite (γ) phase begins to from at the δ ferrite-liquid interface and subsequently within both the existing phases. A three phase region ($\delta + \gamma + L$) is present in both the steels. According to the phase diagram, the three phase region is more pronounced in TRIP steel than in DP steel. Solidification continues as both the liquid and the δ phase are transformed into austenite (γ).
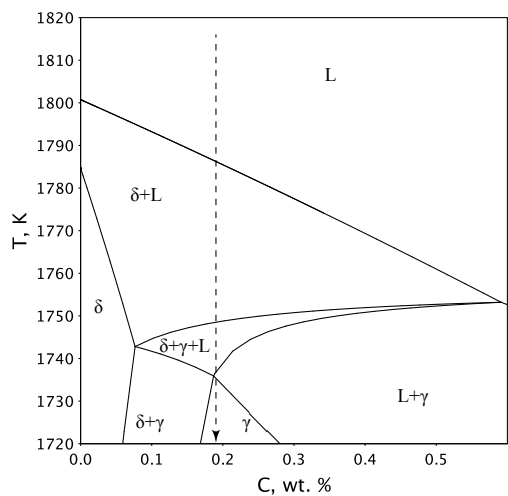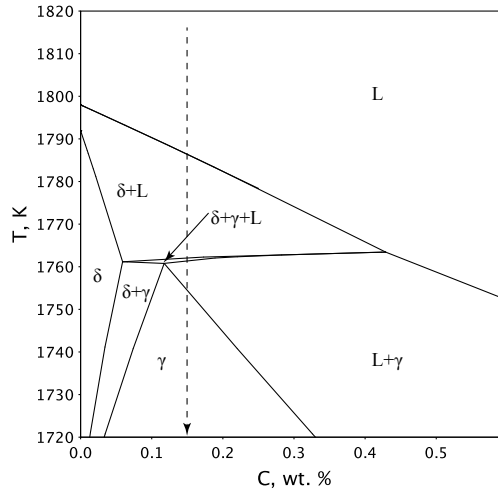
Figure 3.4: Pseudo binary phase diagram of DP steel used in the present work.
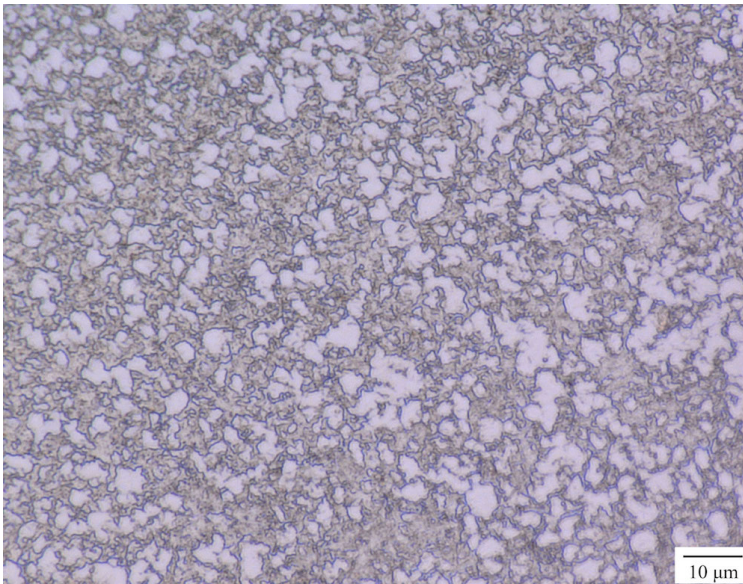
Figure 3.5: Optical micrograph of DP steel showing ferrite matrix with martensite islands. The brownish/tan region is the ferrite matrix while brighter portions are the martensite islands.
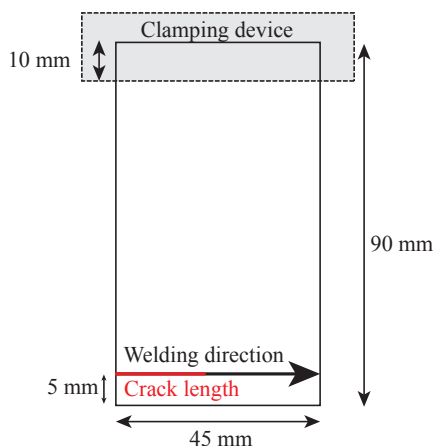
Figure 3.6: Schematic of the solidification cracking test setup.

3.2 Solidification cracking test arrangement

The hot cracking test used in the present work is based on the free edge and the VDEh standard hot cracking test, discussed in the preceding chapter. Bead-on-plate laser welding experiments were conducted parallel to the free edge at various distances from the free edge. The approach is described schematically in Figure 3.6.

Bead-on-plate laser welding was carried out using a 3 kW Nd:YAG laser (Trumpf HAAS HL3006D) in the keyhole mode, with a laser power of 1100 W and a welding speed of 10 mm s^{-1}. Specimens were kept at the focal point of the optical system (focal length = 150 mm) with the laser spot size being 0.45 mm. The low welding speed was necessitated in order to obtain the transient displacement field during welding, by digital image correlation. The laser power was adapted to obtain a fully penetrated weld. Temperature measurements were performed close to the fusion boundary using spot welded K-type thermocouples. In the assembly lines of car manufacturers, laser welding is generally carried out without the use of shielding gas. Also, the hot cracking test standard does not mention the use of shielding gas. To assess the effect of shielding gas on solidification cracking susceptibility, initial welding experiments were performed both with and without shielding gas. No difference in cracking tendency was observed and further tests were therefore carried out without a shielding gas to more closely mimic the industrial procedure.

3.3 High-speed camera imaging

The use of high-speed camera imaging for laser welding research dates back to the mid 1980s [14]. Since then, the advancement in high-speed camera imaging technology has led to an increased use in welding research. In this study, high-speed camera imaging was used to verify the nature of cracking during laser welding. For this purpose, a Phantom Miro M-310 high-speed camera together with a Sigma lens (DL 75-300 mm and close-up
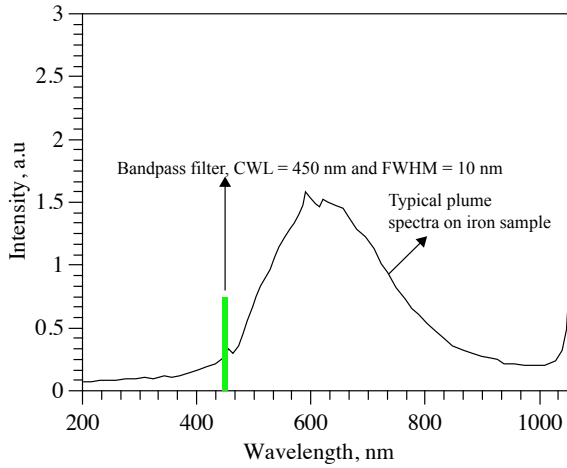
Figure 3.7: Typical emission spectrum of an Nd:YAG laser plume on an iron-based specimen. The graph is replotted from [15].

lens 2X magnification) were used. In order to minimise the effect of intensity of laser plume light, two auxiliary high intensity 30 W LEDs with a wavelength of 450 nm were used to illuminate the top surface of the specimen. A corresponding optical narrow bandpass filter with a centre wavelength of 450 nm and a full-width half maxima (FWHM) of 10 nm was placed in front of the lens. A typical emission spectrum of the laser plume on an iron-based specimen [15] and the position of bandpass filter are shown in Figure 3.7. The experimental arrangement involved a stationary laser and camera, with the specimen moving unidirectionally on a motor controlled stage. The region of interest was on the specimen surface behind the laser spot and images were captured at a rate of 500 frames per second. The camera was positioned sideways with respect to the specimen.

3.4 Digital image correlation (DIC)

Digital image correlation (DIC) is a non-contact method to measure the surface displacement field. In this work, DIC was used to measure 2D displacement/strain fields close to the fusion boundary during welding.
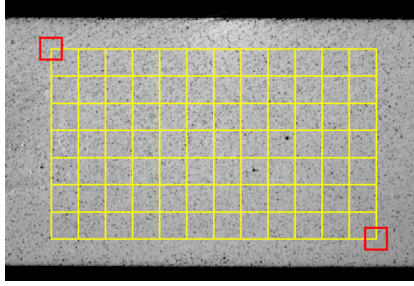
Figure 3.8: An example of reference image with subset (shown in red) used for tracking its centre point. Displacement is calculated at the grid points (intersection points of the grid). With permission from reference [16].

In DIC, a video camera acquires digital images of a random speckle pattern on the specimen surface, before and during deformation. Displacements are calculated by correlating the sequence of digital images. In order to obtain a unique correspondence of pixels between two images, the ideal surface texture should be isotropic and non-periodic [17]. For this purpose, a random speckle pattern is created on the specimen surface. The pattern adheres to the surface and there is no relative motion between the pattern and the underlying specimen surface. For correlation, the reference image is divided into subsets of pixels, the motion of which is detected to calculate displacement at defined grid points as shown in Figure 3.8 [16]. Figure 3.9 shows a schematic illustration of the subset before and after deformation. The undeformed/reference subset is tracked in a defined region of interest (ROI). To achieve this, an area with similar gray level distribution as that in the undeformed subset is sought in the deformed image. Then, the subset position is found using the following normalised cross-correlation coefficient [16, 18],
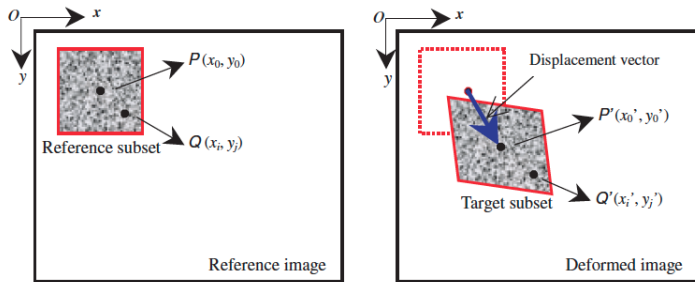
Figure 3.9: Schematic illustration of the subset before and after deformation. With permission from reference [16].

$$C(x, y, x^*, y^*) = \frac{\sum F(x,y) G(x^*, y^*)}{\sqrt{\sum F(x,y)^2 \sum G(x^*, y^*)^2}},\tag{3.1}$$

where, $F(x, y)$ is the gray level at (x, y) in the subset before deformation and $G(x^*, y^*)$ is the gray level at (x^*, y^*) after deformation. The maximum value of the correlation coefficient is found when the grey level distribution inside the undeformed subset matches the local area within the deformed image. The position of the subset in the deformed image is around the position where the correlation coefficient is a maximum. The difference between the reference subset centre point $P(x_0, y_0)$ and the deformed subset centre point $P'(x_0', y_0')$ thus gives the displacement vector [16]. Subsequently, the position of an arbitrary point $Q(x_i, y_i)$ in the reference subset is mapped to point $Q'(x_i', y_i')$ in the deformed subset by using the first-order shape function [19]. For complicated deformed subsets, a second-order shape function is also used [16].

Due to the discrete nature of a digital image with pixels as the smallest unit, displacements smaller than one pixel cannot be calculated using the above procedure. In order to achieve sub-pixel resolution, gray level intensities of points within a pixel must be obtained. For this, usually bilinear or bicubic interpolation functions are used for gray level interpolation [16, 18]. The strain can be obtained by differentiating the estimated displacements. However, smoothing of the computed displacement field is recommended before differentiation [20, 21]. The strains in the x, y directions are calculated as follows,

$$e_{xx} = \frac{\partial u}{\partial x} + \frac{1}{2} \left\{ \left(\frac{\partial u}{\partial x} \right)^2 + \left(\frac{\partial v}{\partial x} \right)^2 \right\},\tag{3.2}$$

$$e_{yy} = \frac{\partial v}{\partial y} + \frac{1}{2} \left\{ \left(\frac{\partial u}{\partial y} \right)^2 + \left(\frac{\partial v}{\partial y} \right)^2 \right\}.\tag{3.3}$$

Here, e_{xx}, e_{yy} are the strains in x, y directions and u, v are the displacements in the x, y directions respectively.

The sources of error in the displacement field calculations include speckle pattern quality, image distortion, out-of-plane displacement and the correlation algorithm. Details of how individual factors lead to an error in the displacement computation are described in the review paper [16].

In the present work, a LIMESS Q-400-3D DIC system along with a commercial software package Istra 4D was used to capture images and to compute displacement fields during welding. Since the 2D displacement field was calculated, only one camera was used. Before the measurement, camera calibration was performed. The calibration parameters are divided into two categories, intrinsic and extrinsic. Intrinsic parameters of the camera includes focal length, principal point and distortion of the lenses, while extrinsic parameters include the rigid transformation from global coordinate system to camera coordinate system. Intrinsic parameters are used to obtain the projective transformation from camera coordinate system into the 2D image coordinates [17]. The calibration was performed using a checkerboard grid of size 18 mm by 18 mm with each square size of 2 mm. A series of 10 images of the calibration grid were taken near the specimen surface in order to obtain the calibration parameters. A speckle pattern on the specimen surface was created using high temperature commercial paint (VHT Flame Proof) of white and
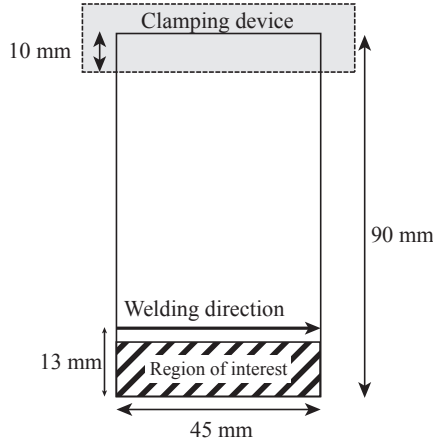
Figure 3.10: Schematic showing the region of interest on which the DIC was performed during welding.

black colour. The paint can withstand a peak temperature of 1330 K. Images at a rate of 8 frames per second during welding were acquired with the region of interest shown in Figure 3.10. The camera-specimen geometry is shown in Figure 4.1. The scale factor of the image was found to be 46.44 pixels per mm. A subset size of 17 × 17 pixels, which translates to a subset size of approximately 370 × 370 μm^2, was used for the calculation of displacements. To suppress the light from the laser plume, two auxiliary high intensity 30 W LEDs were used as described in the previous section. Based on the data obtained from the DIC experiments, the maximum uncertainties in the displacements measurement and transverse strains are 2×10^{-4} mm and 0.02 %, respectively [22].

3.5 High temperature laser scanning confocal microscopy

High temperature laser scanning confocal microscopy was used to study the *in-situ* solidification behaviour of the two steels. In laser scanning confocal microscopy, a high intensity laser light, in this case a He-Ne laser ($\lambda = 632.8\,$nm), is focused by an objective lens on the surface of the specimen. The reflected beam is then focused onto the photon detector *via* a beam splitter as shown in Figure 3.11 [23, 24]. A confocal pinhole placed in front of the detector allows only the light incident from the focal plane to pass on to the detector while light from out-of-focus planes is blocked. In addition, the pinhole also blocks thermal radiation emitted from most of the specimen (only the radiation from the focal plane goes through) and only the polarised reflection of the laser beam reaches the imaging sensor leading to high lateral resolution (ca. $0.25\,\mu$m). By scanning the laser beam spot over the specimen, an image is constructed.
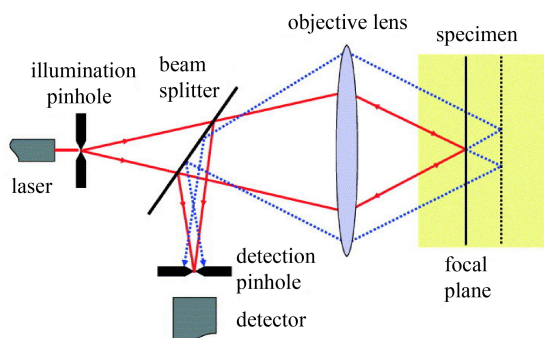
Figure 3.11: Optical principle of confocal microscopy. With permission from reference [24].

In this work, a laser scanning confocal microscope (supplied by Lasertec) in conjunction with an infra-red furnace was used (Figure 3.12). A 1.5 kW halogen lamp located at the bottom focal point in the gold plated ellipsoidal cavity is used to heat the specimen. Specimens were placed at the upper focal point in the cavity. Thin circular disk specimens (thickness between 200-250 μm) were used to obtain a circular melt pool (Figure 3.13). The specimen is kept inside an alumina crucible which in turn is held by a platinum holder. A B-type thermocouple wire was welded to the platinum holder [25, 26]. The power input to the halogen lamp was controlled by a PID controller, thereby allowing a pre-described thermal cycle to be implemented. To prevent oxidation, ultra high purity Ar (99.9999 %) was flushed into the cavity. A stable melt pool with a diameter between 3-4 mm was created before applying the cooling cycle. The temperature and images were recorded simultaneously at a frequency of 30 Hz.

3
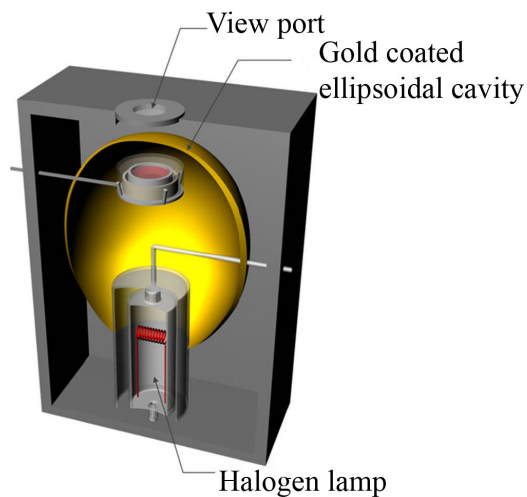
Figure 3.12: Schematic of the infra-red furnace. With permission from reference [27].
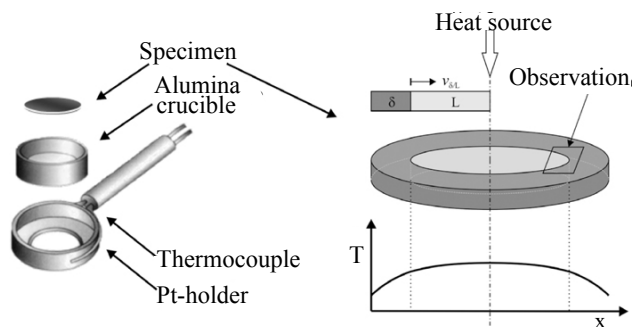
Figure 3.13: Schematic of the specimen geometry, holder and concentric solidification method. With permission from reference [28].

3.6 Microstructural characterisation

Optical microscopy

The top surface and transverse cross-sections of the welded plates were prepared for metallographic investigations. After mounting the sample using conductive resin; grinding, polishing and etching was performed for optical and electron microscopy studies. A two step etching procedure was followed [11]. In the first step, etching was performed for 15-20 seconds using 20 ml of Picral (4 %) mixed with 1 ml of concentrated hydrochloric acid (37 %). Immediately, the sample was washed with water and then by ethanol. After drying the surface by hot air, etching was performed for 8-10 seconds using 10 % aqueous sodium metabilsulfite solution. The two step etching procedure has the following effects on the microstructural constituents; martensite appears straw coloured, retained austenite appears white, bainite appears bluish black and the ferrite matrix appears tan coloured [9, 11]. An example is shown in the optical micrograph of the TRIP steel base metal (Figure 3.3). The samples were further studied using a Keyence VHX-5000 optical microscope.

Scanning electron microscopy

Scanning electron microscopy (SEM) was performed on the weld topside and fracture surface using a JEOL JSM 6500F^{TM} microscope. Energy Dispersive Spectroscopy (EDS) analysis, in conjunction with SEM, was conducted on the weld topside to qualitatively examine the inclusions. Wavelength Dispersive Spectroscopy (WDS) was performed for mapping of elements on the weld surface using a CAMECA® SX100 microprobe. An electron beam energy of 15 kV and probe current of 200 nA was used. For the elemental mapping, an area of $300 \times 400\ \mu m^2$ was selected near the centre of the weld surface and scanning was performed in the spot mode with a spacing of 2 μm.

Electron backscatter diffraction

Due to post welding cooling rates in excess of $100\,Ks^{-1}$ [29, 30], the microstructure of the weld metal is predominantly martensitic. In order to determine the microstructural features of the weld such as solidification substructure and grain orientation, knowledge of the parent grains; *i.e.* austenite, is needed. Cayron *et al.* [31] proposed a method for reconstruction of the austenite grains in steels based on the ferrite orientations of lath martensite. The austenite grain structure is reconstructed by assuming that the orientation relationship between the lath martensite and the parent austenite is either Kurdjumov-Sachs or Nishiyama-Wassermann. For this purpose, use of a computer program ARPGE developed by Cayron [32] was used. The weld surface was prepared for electron backscatter diffraction (EBSD) measurements by mechanical polishing using colloidal silica. EBSD at an accelerating voltage of 15 kV was undertaken to obtain ferrite orientation maps with a step size of 1 μm. A minimum confidence index (CI) of 0.1 was used for parent grain reconstruction.

Atom probe tomography

Atom-probe tomography (APT) is a material analysis technique that allows three dimensional (3D) reconstruction of individual atomic positions in a specimen with a sharply pointed tip (needle like specimen), along with their chemical identities [33]. In this technique, the sample is prepared in the form of a sharp tip usually by dual focused-ion beam (FIB) microscopy and placed in a ultra high vacuum system at low temperatures (20-30 K) [34]. A high voltage is applied at the tip of the specimen which generates an electric field at the tip surface. Subsequently, a local electrode is pulsed with a negative voltage at high frequency to generate the necessary electric field for field evaporation of individual atoms or a group of atoms at the tip. Alternatively, laser pulses at high frequency can also be used for the evaporation of atoms. The evaporated ions are projected onto a position sensitive detector where the position and time of flight of individual striking ions is recorded. The time of flight allows the determination of charge to mass ratio and thus the chemical identity of individual atoms. By progressively removing the atoms from the tip, a 3D image of the specimen is constructed using dedicated software [33–35]. Figure 3.14 shows the schematic of a pulsed laser local-electrode atom-probe (LEAP) tomograph.
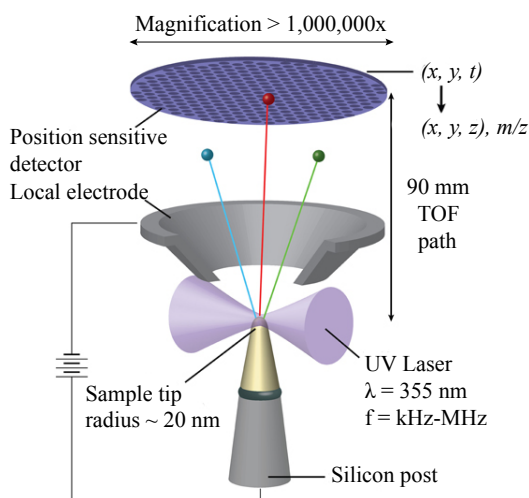
Figure 3.14: Schematic of a pulsed-laser local-electrode atom probe tomograph. Taken from reference [36], which is published as an open access article under CC BY license.

In this work, the needle shaped specimens were prepared for APT by focused ion beam (FIB) milling in a FEI-Helios Nanolab 600i dual beam FIB/SEM. Subsequently, APT measurements were performed using a LEAP 3000X HR in voltage mode using a set-point temperature of 65 K. A pulsed fraction voltage of 15 % and a pulsed frequency of 200 kHz was applied. Data reconstruction was undertaken using the procedure described in reference [37, 38] and data analysis was performed using IVAS software.

3.7 Finite element modelling

Finite-element modelling (FEM) is a powerful numerical methodology to obtain approximate solutions of partial differential equations that describe many engineering problems. These problems are boundary value problems (also known as field problems) in which the dependent variables (*e.g.* temperature) satisfy a partial differential equation (*e.g.* heat transfer) over a domain or field of independent variables (*e.g.* spatial coordinates x, y, z) and satisfy certain conditions over the boundary of the domain (*e.g.* ambient temperature, convection and radiation). The field variables or the dependent variables are of interest in a particular problem [39].

In the finite element method, the entire domain is divided into a set of simple subdomains called finite elements. The finite elements are connected with adjacent elements by discrete number of points, called nodes. The field variable is approximated at the nodes using a linear combination of trial functions. The field variable is then calculated within the elements using interpolation functions (also known as shape functions) [40].
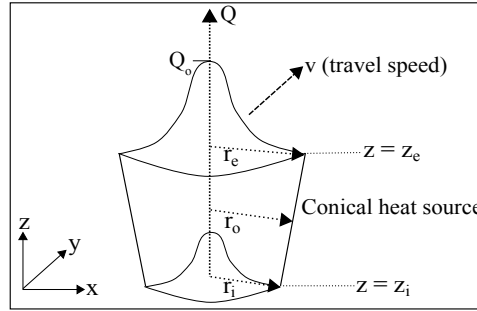
Figure 3.15: 3D conical heat source with Gaussian distribution adopted in the present work.

In this work, a sequentially coupled 3D finite element (FE) thermal mechanical model with isotropic hardening was utilised for laser bead-on-plate welding. Initially, a transient heat transfer analysis was carried out to obtain the time dependent thermal history. In this study, a frequently used [41–43] 3D conical Gaussian heat source was adopted to describe the laser beam heat input (Figure 3.15). The power density distribution at any plane perpendicular to the z-axis is expressed as:

$$Q_v = Q_o \exp\left(\frac{-3r^2}{r_o^2}\right), \tag{3.4a}$$

where, Q_v is the net volumetric heat flux, Q_o is the maximum heat source intensity and r is the radial distance from the centre of the heat source, expressed as:

$$r = \sqrt{x^2 + y^2}. \tag{3.4b}$$

The radius of the heat source (r_o) is assumed to decrease linearly through the thickness of the cone and can be expressed as:

$$r_o = r_e - \frac{(r_e - r_i)(z_e - z)}{(z_e - z_i)}, \tag{3.4c}$$

where, r_e and r_i are the radii of the top and bottom surfaces of the conical heat source, respectively. The z coordinates of the top and bottom surfaces are z_e and z_i, respectively. Q_o can be determined via the energy conservation principle:

$$\eta P = \int_0^H \int_0^{2\pi} \int_0^{r_o} Q_o \exp\left(\frac{-3r^2}{r_o^2}\right) r\, dr\, d\theta\, dh, \tag{3.5a}$$

using $z_e - z_i = H$ and $z = z_i + h$, further leads to,

$$Q_o = \frac{9\eta P \exp(3)}{\pi(\exp(3) - 1)} \cdot \frac{1}{(z_e - z_i)(r_e^2 + r_i^2 + r_e r_i)}. \tag{3.5b}$$

Here, η is the process efficiency of the laser welding and P is the laser power. The height of the heat source, *i.e.* H was considered to be equal to the sheet thickness and $r_e = 1\,\text{mm}$, $r_i = 0.9\,\text{mm}$ were chosen to achieve the dimensions of the weld observed in the experiments.

The thermal history, *i.e,* temperatures (T) at (x, y, z, t) was obtained by solving the following Fourier heat transfer equation using the temperature-dependent thermal properties of the material,

$$\frac{\partial}{\partial x}\left(k(T)\frac{\partial T}{\partial x}\right) + \frac{\partial}{\partial y}\left(k(T)\frac{\partial T}{\partial y}\right) + \frac{\partial}{\partial z}\left(k(T)\frac{\partial T}{\partial z}\right) + Q_v = \rho(T)C_p(T)\left(\frac{\partial T}{\partial t}\right). \tag{3.6}$$

Here, $k(T)$ is the temperature dependent thermal conductivity, $\rho(T)$ is the temperature dependent density and $C_p(T)$ is the temperature dependent specific heat capacity.

The initial boundary condition for the transient analysis is given by

$$T(x, y, z, 0) = T_0, \tag{3.7}$$

where, T_0 is the ambient temperature taken as 293 K. The natural boundary condition, implicitly considered in the finite element analysis is,

$$k_n \frac{\partial T}{\partial n} - q + h(T - T_0) + \sigma e(T^4 - T_0^4) = 0. \tag{3.8}$$

The condition applies on the boundaries which are subjected to convection, radiation and heat flux. k_n is the thermal conductivity normal to the boundary, q is the imposed heat flux on the boundary due to the external heat source, h is the heat transfer coefficient for convection, σ is the Stefan-Boltzmann constant for radiation ($5.67 \times 10^{-8}\,\text{W}\,\text{m}^{-2}\,\text{K}^{-4}$) and e is the emissivity. The heat transfer coefficient was taken to be $10\,\text{W}\,\text{m}^{-2}\,\text{K}^{-1}$ [44]. The emissivity was assumed to be a function of temperature based on the work of van der Aa [45] given by,

$$e = 0.7 - 0.02\exp\left(\frac{900}{T}\right). \tag{3.9}$$

The thermophysical properties of the TRIP steel, *i.e.* density, specific heat capacity and thermal conductivity were taken from reference [46] and are shown in Figure 3.16. Note that the chemical composition of the TRIP steel used in [46] is similar to the TRIP steel used in this work. Moreover it is reported in the reference that the properties were

measured as a function of temperature up to 1723 K. At this temperature, the steel is still in the solid state. The latent heat data was taken from a commercial thermodynamic software, Thermo-Calc^{TM}(database TCFE7). In the two phase region, apparent heat capacity method was applied [47]. The latent heat is included as an additional term in the heat capacity. The total heat capacity can be written as,

$$C_p = C_{p,solid}(1 - f_L(T)) + C_{p,liquid}f_L(T) + L\frac{\mathrm{d}f_L}{\mathrm{d}T}, \tag{3.10}$$

where, $C_{p,solid}$ is the specific heat capacity of the solid, $C_{p,liquid}$ is the specific heat capacity of the liquid, f_L is the fraction of liquid and L is the latent heat of fusion. The apparent heat capacity was related to the temperature-phase fraction data, obtained using the Scheil-Gulliver solidification approximation with carbon as the fast diffusing component. The total apparent heat in the two phase region as a function of temperature is shown in Figure 3.17.
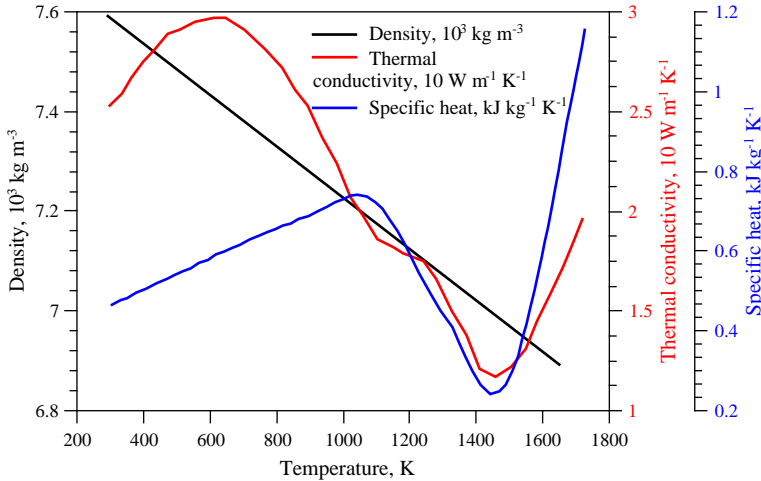
Figure 3.16: Thermophysical properties of TRIP steel. Taken from reference [46].

The thermophysical properties of DP steel used in the model are shown in Figure 3.18. Thermal conductivity was measured as a function of temperature (room temperature, 473 K, 673 K, 873 K, 1073 K, 1273 K), using a laser flash apparatus (NETZSCH LFA 427), following the standard DIN EN 821/2 [48]. The thermal conductivity above 1273 K was taken based on extrapolation; a constant value of 36.6 W m^{-1} K^{-1} was assumed from 1400 K onwards [49]. Specific heat was measured as a function of temperature, using differential scanning calorimetry (NETZSCH DSC 404 C), following the standard DIN EN 821/3 [50] until 1623 K. Density data was obtained using Thermo-Calc^{TM}(database TCFE7). The apparent heat capacity for DP steel was calculated by the same procedure as described above and is shown in Figure 3.19.
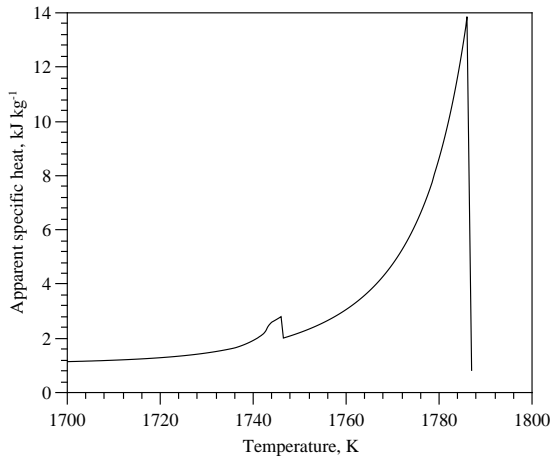
Figure 3.17: Apparent specific heat as a function of temperature for TRIP steel.
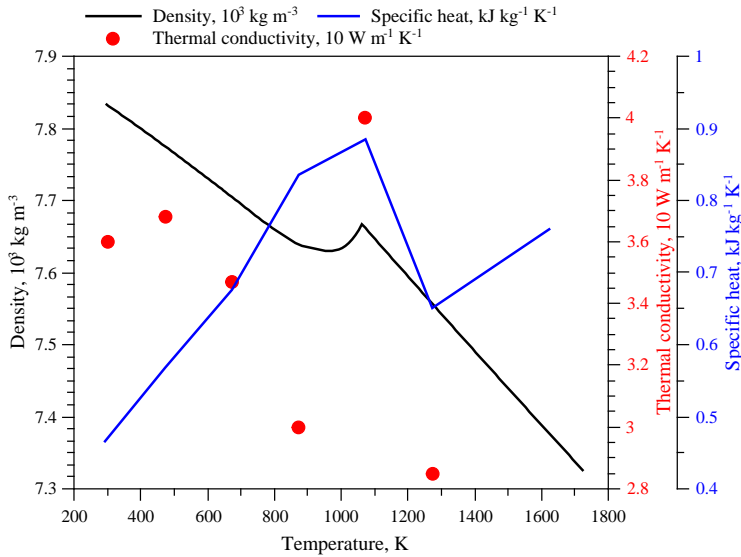
Figure 3.18: Thermophysical properties of DP steel.

The thermal history obtained from the transient finite element analysis was imported sequentially to the mechanical model. Hibbitt *et al.* [51] used the sequential thermal-mechanical modelling approach and based on a comparison with welding experiments, concluded that the effect of mechanical behaviour on thermal load is negligible. Since then, the sequential coupling approach is frequently applied in welding research [52–54]. An isotropic hardening model with the Von Mises yielding criterion was used for the
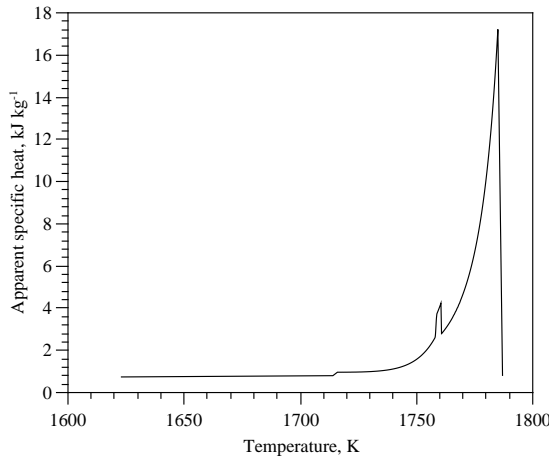
Figure 3.19: Apparent specific heat as a function of temperature for DP steel.

elastic-plastic mechanical analysis. A small tangent modulus value of 2 MPa was used to avoid convergence issues in the numerical analysis. Several studies considered elasto-plastic behaviour in the mechanical model on the assumption that the influence of the strain hardening effect is negligible [55–58]. The fluid flow effect was also not considered and material properties at the melting point (1786 K for TRIP steel and 1786 K for DP steel) were used for higher temperatures. The yield stress, Young's modulus and thermal expansion coefficient as a function of temperature are shown in Figure 3.20.
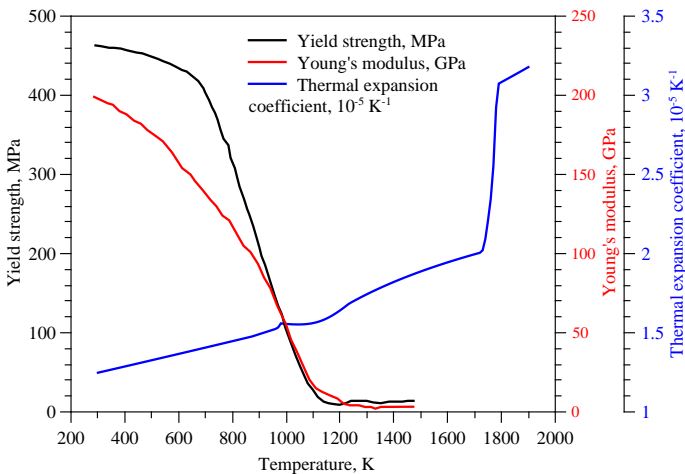
Figure 3.20: Temperature dependent mechanical properties of TRIP steel. The yield stress and Young's modulus data was taken from from reference [46]. Thermal expansion coefficient data was taken from the commercial software JMatPro®.
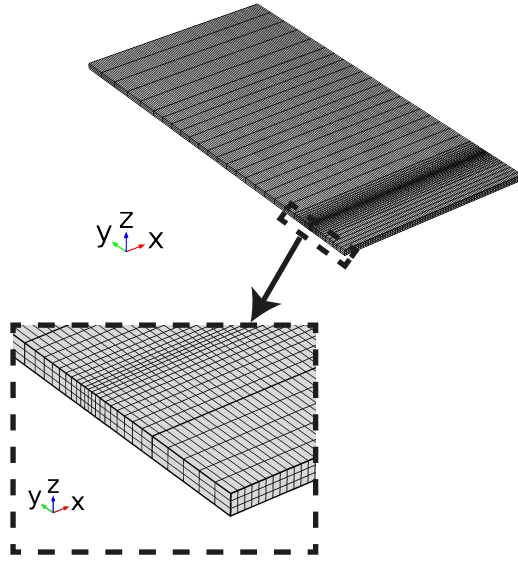
Figure 3.21: FE-model of the laser welding.

The commercial finite element software, COMSOL^{TM} (version 5.2) was used in the present work. Hexahedral elements (brick) were used for meshing the geometry. A minimum mesh size of 0.27 x 0.417 x 0.417 mm^3 was used in the weld zone and gradually the mesh size was increased. Figure 3.21 shows the geometry of the FE model. In order to obtain continuous strain between the elements, second order elements (quadratic shape functions) were used in the mechanical analysis. However, first order elements (linear shape functions) were used in the thermal analysis. The total number of nodes are 20056, 138229 for the thermal and mechanical analyses respectively.

The process efficiency of laser welding, *i.e.* η was assumed to be 40 % based on previous work of Pan [59] on a similar experimental arrangement. In this way, heat losses due to convection and radiation in the keyhole were taken into account. To implement the clamping conditions in the mechanical model, the displacements of the nodes between the clamp in the three directions were fixed.

3.8 Phase field modelling

Over the last decades, the phase field method has become an important tool to visualise the microstructural development without the need of explicit tracking of the interface (Figure 3.22 (a)) [60]. The method is based on the framework of irreversible thermodynamics. Consider the case of solidification in which a solid phase is growing in the liquid, separated by an interface as shown in Figure 3.22 (b). The phase field method considers a single variable, ϕ, known as the order parameter that varies with position and time. The solid phase can be represented by $\phi = 1$ while the liquid phase by $\phi = 0$. The interface is considered to be diffuse and the order parameter varies continuously ($0 < \phi < 1$) within the interface as shown in Figure 3.22 (b).
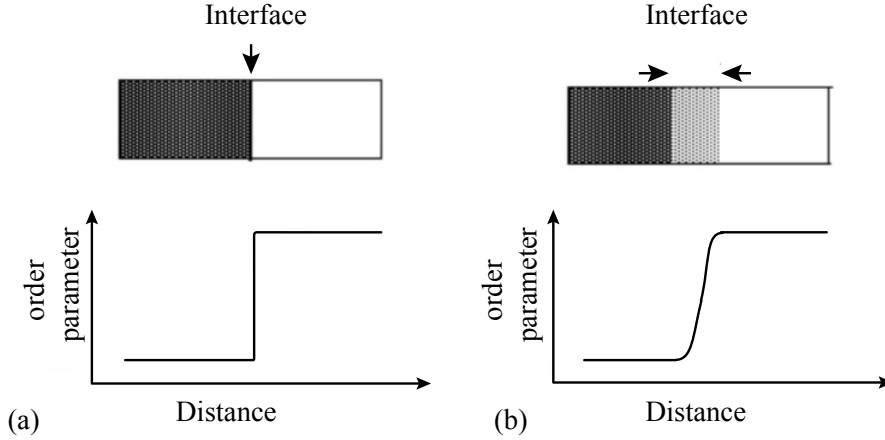
Figure 3.22: (a) Sharp interface, (b) diffuse interface. With permission from reference [60].

By considering the interface as diffuse, the boundary conditions that are required for a sharp interface are not needed in the phase field method [60]. The phase field is defined as the set of values of the order parameter at each location in a given space at a given time. The free energy G is defined in terms of ϕ and the gradients of ϕ. The microstructural evolution thus depends on how G varies with ϕ. Based on Cahn and Hilliard theory [61–64], the free energy of a heterogeneous system is given by [60, 65],

$$G = \int_V \left[g_0 \{\phi, c, T\} + \frac{\epsilon^2}{2} (\nabla \phi)^2 \right] dV, \tag{3.11a}$$

with

$$\epsilon^2 = \frac{\partial^2 g_0}{\partial (\nabla \phi)^2} - 2\partial \frac{(\partial g_0 / \partial \nabla^2 \phi)}{\partial \phi}, \tag{3.11b}$$

where, g_0 is the free energy per unit volume as a function of ϕ, composition c and temperature T. ϵ^2 is the gradient energy coefficient. For g_0, expressions typically bearing double well potential or double obstacle potential shapes are used with two minima representing the free energy of the solid and liquid phase. The free energy density within the interface is based on extrapolation. The generic form of the phase field equation for which the free energy decreases with time is [60]:

$$\frac{\partial \phi}{\partial t} = M_\phi \left(\epsilon_\phi^2 \nabla^2 \phi - \frac{\partial g(\phi)}{\partial \phi} \right), \tag{3.12}$$

where, M_ϕ is the mobility related to interface kinetic coefficient.

In this work, the approach used by Steinbach *et al.* [66] is used. Considering the dual phase system (solid and liquid), the phase-field equation is [67]:

$$\frac{\partial \phi_\alpha}{\partial t} = \sum_\beta \mu_{\alpha\beta} \left\{ \sigma_{\alpha\beta} \left[\phi_\beta \nabla^2 \phi_\alpha - \phi_\alpha \nabla^2 \phi_\beta + \frac{\pi^2}{2\eta^2} (\phi_\alpha - \phi_\beta) \right] + \frac{\pi}{\eta} \sqrt{\phi_\alpha \phi_\beta} \Delta G_{\alpha\beta} \right\}, \tag{3.13}$$

where, $\mu_{\alpha\beta}$ is the solid-liquid interface mobility, $\sigma_{\alpha\beta}$ is the solid-liquid interface energy, η is the interface thickness. $\Delta G_{\alpha\beta}$ is the driving force for solidification, which is a function of the local chemical composition and temperature. The phase field equation is coupled with the diffusion equations by the driving force, details of which can be found in reference [67].

Table 3.2: Energy parameters used in the phase field model for the interaction between liquid-delta ferrite phases. Taken from references [68, 69].

Surface energy	$1.6 \times 10^{-1}\,\mathrm{J\,m^{-2}}$
Kinetic coefficient	$7.3 \times 10^{-11}\,\mathrm{m^4\,J^{-1}\,s^{-1}}$
Static anisotropy coefficient	0.45
Kinetic anisotropic coefficient	0.3

A commercial software, MICRESS® (based on the approach of Steinbach *et al.* [66]) was used to simulate the microstructural evolution during solidification. The software is coupled with the thermodynamic database TCFE6 and mobility data base MOB2 to obtain equilibrium phase boundaries and diffusion coefficients respectively (*via* the commercial software Thermo-Calc™). The initial concentration of the components was set to be in equilibrium in the liquid phase for both the steels. During solidification, the system undergoes a liquid to solid reaction based on the phase field evolution which is related to local driving force. The emphasis is on the liquid to δ ferrite phase transformation during solidification. The energy parameters used in the model [68] for phase interactions are listed in Table 3.2.

The following two cases were considered:

1. The first approach was based on *in-situ* high temperature confocal microscopy experiments in which a local melt pool was allowed to solidify under controlled conditions. Cooling rate and thermal gradient used in the phase-field model were based on the experimental conditions. Further details are provided in the chapter 6.

2. A phase field model for solidification under laser welding conditions was created for both TRIP and DP steels. The thermal gradients were adopted from the FE-model. A fixed mechanical mechanical boundary condition was applied to the simulation domain. The focus was on the solidification behaviour at the weld centreline behind the weld pool and particularly on the conditions that lead to the separation of grains. The approach is described schematically in Figure 3.23, the results of which are discussed in chapter 8.
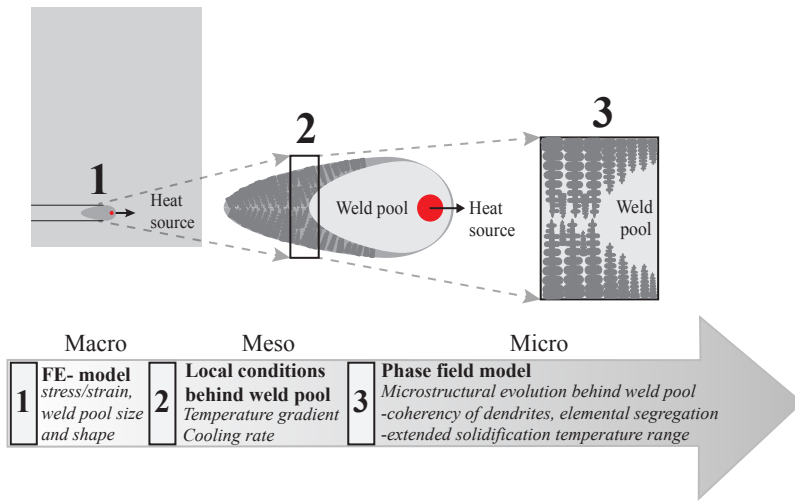
Figure 3.23: Schematic of the approach adopted in the present work. At first, a FE-thermal model of laser welding was created. The validated model was then used to extract the local conditions -thermal gradient and cooling rate behind the weld pool. These parameters along with the thermodynamic and mobility data from Thermo-Calc^{TM} were used in the phase field model of solidification. The focus is on the microstructural evolution behind the weld pool.

References

[1] T. Hilditch, T. de Souza and P. Hodgson, *Properties and automotive applications of advanced high-strength steels (AHSS)*, in *Welding and Joining of Advanced High Strength Steels (AHSS)*, edited by M. Shome and M. Tumuluru (Woodhead Publishing, 2015) pp. 9 – 28.

[2] R. Kuziak, R. Kawalla and S. Waengler, *Advanced high strength steels for automotive industry,* Archives of Civil and Mechanical Engineering **8**, 103 (2008).

[3] V. F. Zackay, E. R. Parker, D. Fahr and R. Bush, *The enhancement of ductility in high-strength steels,* Transactions of the ASM **60**, 252 (1967).

[4] O. Matsumura, Y. Sakuma and H. Takechi, *Enhancement of elongation by retained austenite in intercritical annealed 0.4C-1.5Si-0.8Mn steel,* Transactions of the Iron and Steel Institute of Japan **27**, 570 (1987).

[5] O. Matsumura, Y. Sakuma and H. Takechi, *TRIP and its kinetic aspects in austempered 0.4C-1.5Si-0.8Mn steel,* Scripta Metallurgica **21**, 1301 (1987).

[6] J. Mahieu, J. Maki, B. De Cooman and S. Claessens, *Phase transformation and mechanical properties of Si-free CMnAl transformation-induced plasticity-aided steel,* Metallurgical and Materials Transactions A **33**, 2573 (2002).

[7] F. B. Pickering, *Physical metallurgy and the design of steels* (Applied Science Publishers, London, 1978).

3

[8] B. D. Cooman, *Structure–properties relationship in trip steels containing carbide-free bainite,* Current Opinion in Solid State and Materials Science **8**, 285 (2004).

[9] M. Amirthalingam, *Microstructural development during welding of TRIP steels,* Ph.D. thesis, TU Delft (2010).

[10] S. Chatterjee, *Transformations in TRIP-assisted Steels: Microstructure and Properties,* Ph.D. thesis, University of Cambridge (2006).

[11] A. K. De, J. G. Speer and D. K. Mattock, *Color tint-etching for multiphase steels,* Advanced Materials & Processes **161**, 27 (2003).

[12] C. Tasan, M. Diehl, D. Yan, M. Bechtold, F. Roters, L. Schemmann, C. Zheng, N. Peranio, D. Ponge, M. Koyama, K. Tsuzaki and D. Raabe, *An overview of dual-phase steels: Advances in microstructure-oriented processing and micromechanically guided design,* Annual Review of Materials Research **45**, 391 (2015).

[13] C. Lesch, N. Kwiaton and F. B. Klose, *Advanced high strength steels (AHSS) for auto-motive applications tailored properties by smart microstructural adjustments,* steel research international **88**, 1700210.

[14] Y. Arata, N. Abe and T. Oda, *Fundamental phenomena in high power CO_2 laser welding,* Transactions of JWRI **14**, 5 (1985).

[15] B. Aalderink, R. Aarts, J. Jonker and J. Meijer, *Weld plume emissions during nd:yag laser welding,* in *Lasers in manufacturing 2005,* edited by E. Beyer, F. Dausinger, A. Ostendorf and A. Otto (AT-Fachverlag GmbH Stuttgart, München, Germany, 2005) pp. 413–417.

[16] B. Pan, K. Qian, H. Xie and A. Asundi, *Two-dimensional digital image correlation for in-plane displacement and strain measurement: a review,* Measurement Science and Technology **20**, 062001 (2009).

[17] M. A. Sutton, J.-J. Orteu and H. Schreier, *Image Correlation for Shape, Motion and De-formation Measurements: Basic Concepts,Theory and Applications,* 1st ed. (Springer Publishing Company, Incorporated, 2009).

[18] S. Yoneyama, *Basic principle of digital image correlation for in-plane displacement and strain measurement,* Advanced Composite Materials **25**, 105 (2016).

[19] H. W. Schreier and M. A. Sutton, *Systematic errors in digital image correlation due to undermatched subset shape functions,* Experimental Mechanics **42**, 303 (2002).

[20] D. J. Segalman, D. B. Woyak and R. E. Rowlands, *Smooth spline-like finite-element differentiation of full-field experimental data over arbitrary geometry,* Experimental Mechanics **19**, 429 (1979).

[21] S. Yoneyama, *Smoothing measured displacements and computing strains utilising finite element method,* Strain **47**, 258.

[22] *LIMESS webpage Retrieved (29-01-2019) from:* `https://www.limess.com/en/products/q400-digital-image-correlation#technical-specifications` (2017).

[23] P. T. Jones, D. Desmet, M. Guo, D. Durinck, F. Verhaeghe, J. V. Dyck, J. Liu, B. Blanpain and P. Wollants, *Using confocal scanning laser microscopy for the in situ study of high-temperature behaviour of complex ceramic materials,* Journal of the European Ceramic Society **27**, 3497 (2007).

[24] F. van de Velde, F. Weinbreck, M. W. Edelman, E. van der Linden and R. Tromp, *Visualisation of biopolymer mixtures using confocal scanning laser microscopy (cslm) and covalent labelling techniques,* Colloids and Surfaces B: Biointerfaces **31**, 159 (2003).

[25] D. Phelan, M. Reid and R. Dippenaar, *Kinetics of the peritectic phase transformation: In-situ measurements and phase field modeling,* Metallurgical and Materials Transactions A **37**, 985 (2006).

[26] M. Reid, D. Phelan and R. Dippenaar, *Concentric solidification for high temperature laser scanning confocal microscopy,* ISIJ International **44**, 565 (2004).

[27] I. Sohn and R. Dippenaar, *In-situ observation of crystallization and growth in high-temperature melts using the confocal laser microscope,* Metallurgical and Materials Transactions B **47**, 2083 (2016).

[28] S. Griesser, M. Reid, R. Pierer, C. Bernhard and R. Dippenaar, *In situ quantification of micro-segregation that occurs during the solidification of steel,* steel research international **85**, 1257 (2014) .

[29] S. A. David and T. DebRoy, *Current issues and problems in welding science,* Science **257**, 497 (1992).

[30] J. W. Elmer, S. M. Allen and T. W. Eagar, *Microstructural development during solidification of stainless steel alloys,* Metallurgical Transactions A **20**, 2117 (1989).

[31] C. Cayron, B. Artaud and L. Briottet, *Reconstruction of parent grains from ebsd data,* Materials Characterization **57**, 386 (2006).

[32] C. Cayron, *ARPGE: a computer program to automatically reconstruct the parent grains from electron backscatter diffraction data,* Journal of Applied Crystallography **40**, 1183 (2007).

[33] D. N. Seidman and K. Stiller, *An atom-probe tomography primer,* MRS Bulletin **34**, 717 (2009).

[34] D. N. Seidman, *Three-dimensional atom-probe tomography: Advances and applications,* Annual Review of Materials Research **37**, 127 (2007).

[35] T. F. Kelly and D. J. Larson, *Atom probe tomography 2012,* Annual Review of Materials Research **42**, 1 (2012).

3

[36] L. M. Gordon and D. Joester, *Mapping residual organics and carbonate at grain boundaries and the amorphous interphase in mouse incisor enamel*, Frontiers in Physiology **6**, 57 (2015).

[37] B. Gault, F. de Geuser, L. T. Stephenson, M. P. Moody, B. C. Muddle and S. P. Ringer, *Estimation of the reconstruction parameters for atom probe tomography*, Microscopy and Microanalysis **14**, 296 (2008).

[38] B. Gault, D. Haley, F. de Geuser, M. Moody, E. Marquis, D. Larson and B. Geiser, *Advances in the reconstruction of atom probe tomography data*, Ultramicroscopy **111**, 448 (2011), Special issue: 52nd International Field Emission Symposium.

[39] D. Hutton, *Fundamentals of Finite Element Analysis*, McGraw-Hill series in mechanical engineering (McGraw-Hill, 2004).

[40] N. Kim, *Introduction to Nonlinear Finite Element Analysis*, SpringerLink (Springer US, 2014).

[41] N. Shanmugam, G. Buvanashekaran, K. Sankaranarayanasamy and S. R. Kumar, *A transient finite element simulation of the temperature and bead profiles of t-joint laser welds*, Materials & Design **31**, 4528 (2010).

[42] J. Ma, F. Kong and R. Kovacevic, *Finite-element thermal analysis of laser welding of galvanized high-strength steel in a zero-gap lap joint configuration and its experimental verification*, Materials & Design **36**, 348 (2012).

[43] M. Z. ul abdein, D. Nélias, J.-F. Jullien and D. Deloison, *Experimental investigation and finite element simulation of laser beam welding induced residual stresses and distortions in thin sheets of AA 6056-T4*, Materials Science and Engineering: A **527**, 3025 (2010).

[44] H. Gao, *Residual Stress Development due to High-Frequency Post Weld Impact Treatments for High-Strength Steels*, Ph.D. thesis, TU Delft (2014).

[45] E. van der Aa, *Local Cooling during Welding: Prediction and Control of Residual Stresses and Buckling Distortion*, Ph.D. thesis, TU Delft (2007).

[46] E. A. A. Ahmed, *Laser Welding of Advanced High Strength Steels*, Ph.D. thesis, RWTH Aachen (2011).

[47] H. Hu and S. Argyropoulos, *Mathematical modelling of solidification and melting: A review*, Modelling and Simulation in Materials Science and Engineering **4**, 371 (1996).

[48] *Advanced technical ceramics - monolithic ceramics, thermo-physical properties - part 2: Determination of thermal diffusity by the laser flash (or heat pulse) method; DIN 821-2*, (1997).

[49] X. Li, L. Wang, L. Yang, J. Wang and K. Li, *Modeling of temperature field and pool formation during linear laser welding of DP1000 steel*, Journal of Materials Processing Technology **214**, 1844 (2014) .

[50] *Advanced technical ceramics - monolithic ceramics - thermo-physical properties - part 3: Determination of specific heat capacity; DIN 821-3,* (2005).

[51] H. D. Hibbitt and P. V. Marcal, *A numerical, thermo-mechanical model for the welding and subsequent loading of a fabricated structure,* Computers & Structures **3**, 1145 (1973).

[52] E. Friedman, *Thermomechanical analysis of the welding process using the finite element method,* Journal of Pressure Vessel Technology **97**, 206 (1975).

[53] H. Gao, R. K. Dutta, R. M. Huizenga, M. Amirthalingam, M. J. M. Hermans, T. Buslaps and I. M. Richardson, *Pass-by-pass stress evolution in multipass welds,* Science and Technology of Welding and Joining **19**, 256 (2014).

[54] E. Feulvarch, V. Robin and J. M. Bergheau, *Thermometallurgical and mechanical modelling of welding – application to multipass dissimilar metal girth welds,* Science and Technology of Welding and Joining **16**, 221 (2011).

[55] J. Cañas, R. Picón, F. Paríis, A. Blazquez and J. Marín, *A simplified numerical analysis of residual stresses in aluminum welded plates,* Computers & Structures **58**, 59 (1996).

[56] D. Deng, W. Liang and H. Murakawa, *Determination of welding deformation in fillet-welded joint by means of numerical simulation and comparison with experimental measurements,* Journal of Materials Processing Technology **183**, 219 (2007).

[57] W. Liang and H. Murakawa, *An inverse analysis method to estimate inherent deformations in thin plate welded joints,* Materials & Design **40**, 190 (2012).

[58] A. A. Bhatti, Z. Barsoum, H. Murakawa and I. Barsoum, *Influence of thermo-mechanical material properties of different steel grades on welding residual stresses and angular distortion,* Materials & Design (1980-2015) **65**, 878 (2015).

[59] Y. Pan, *Laser welding of zinc coated steel without pre-set gap,* Ph.D. thesis, TU Delft (2011).

[60] R. S. Qin and H. K. Bhadeshia, *Phase field method,* Materials Science and Technology **26**, 803 (2010).

[61] J. Cahn and J. Hilliard, *Free energy of a nonuniform system. iii nucleation in a two-component incompressible fluid,* Journal of Chemical Physics **31**, 688 (1959).

[62] J. W. Cahn, *On spinodal decomposition,* Acta Metallurgica **9**, 795 (1961).

[63] J. Cahn, *Spinodal decomposition,* Transactions of the Metallurgical Society of American Institute of Mining, Metallurgical, and Petroleum Engineers **242**, 166 (1968).

[64] H. E. Hilliard, *Spinodal decomposition,* in *Phase Transformations,* edited by V. F. Zackay and H. I. Aaronson (Metals Park, OH, ASM International, 1970) pp. 497–560.

[65] W. J. Boettinger, J. A. Warren, C. Beckermann and A. Karma, *Phase-field simulation of solidification,* Annual Review of Materials Research **32**, 163 (2002).

3

[66] I. Steinbach and F. Pezzolla, *A generalized field method for multiphase transformations using interface fields,* Physica D **134**, 385 (1999).

[67] B. Böttger, J. Eiken and I. Steinbach, *Phase field simulation of equiaxed solidification in technical alloys,* Acta Materialia **54**, 2697 (2006).

[68] M. Amirthalingam, E. M. van der Aa, C. Kwakernaak, M. J. M. Hermans and I. M. Richardson, *Elemental segregation during resistance spot welding of boron containing advanced high strength steels,* Welding in the World **59**, 743 (2015).

[69] H. Gao, G. Agarwal, M. Amirthalingam and M. J. M. Hermans *Hot cracking investigation during laser welding of high-strength steels with multi-scale modelling approach,* Science and Technology of Welding and Joining **23**, 287 (2018).

3

4

Strain investigation during laser welding using digital image correlation and finite-element based numerical simulation[**]

IN-SITU strain evolution during laser welding has been measured by means of digital image correlation to assess the susceptibility of an advanced high strength automotive steel to solidification cracking. A novel method realised by using auxiliary illumination and an optical narrow bandpass filter allowed strain measurements as close as 1.5 mm from the fusion boundary with good spatial and temporal resolution. A finite element thermomechanical model of the welding process supports the experimentally measured transverse strain. The validated finite element numerical model can be used to assess the local strain and associated stress conditions which influences weldability and in particular, solidification cracking.

4.1 Introduction

In the last decades, laser beam welding has become increasingly popular in the automotive industry. The high power density ($\sim 10^{10}$ W m^{-2}) facilitates the welding of steels at high speed, thereby increasing productivity. During welding, materials experience non uniform heating and cooling cycles; this results in the development of stresses, deformation and distortion. Apart from metallurgical effects, described in chapter 2, the evolution of strains and stresses in the weld and heat affected zone determine the weldability of an alloy. An important indicator of weldability is its resistance to cracking, either in the

---

72

4. Strain investigation during laser welding using digital image correlation and finite-element based numerical simulation

weld or in the heat affected zone. One of the major defects encountered in the casting and welding industries is hot tearing, also referred to as solidification cracking [1, 2]. Accurate determination of local strain and associated stresses produced during welding is important to generate a better understanding of welding induced deformation and defect formation, including solidification cracking.

One of the methods to measure full field displacement and strain during a thermome-chanical process is digital image correlation (DIC). The DIC technique, described in detail in chapter 3, has been used to measure strains at the grain level [4], to study failure in thermal barrier coatings [5], to investigate fatigue cracks [6] *etc.* DIC is generally applied *ex-situ* for welding related measurements. *In-situ* studies are hindered by the intense light emitted during welding, which renders observation close to the fusion boundary difficult. There are only a few reported studies in which the *in-situ* strains are measured during welding [7–10]. In these studies displacement fields were measured either far from the weld centreline or on the underside of the specimen in order to minimise the effect of intense light and heat.

In this study, the DIC technique is applied on the upper surface close to a weld to measure *in-situ* transverse strain fields during laser welding of TRIP steel sheets. The re-sults are compared with the output from a finite-element (FE)-based thermal mechanical model. In addition, the DIC technique is also used to measure the transverse strain fields during welding of DP steel sheets.

4.2 Experimental setup

Bead-on-plate welding experiments were performed using a 3 kW Nd:YAG laser in the keyhole mode. A laser power of 1100 W and a welding speed of $10 \, \text{mm} \, \text{s}^{-1}$ was used in all the experiments. With these parameters, a full penetration weld bead of width 2.5 mm was obtained. Rectangular TRIP steel sheets of dimensions 90 x 45 mm^2 and 1.25 mm thickness were welded. The chemical composition of the steel is listed in Table 3.1. The experimental arrangement used in this study is shown schematically in Figure 4.1 (a). This figure includes the coordinate system used for DIC measurements. The starting laser beam position was at $x = 0$ mm, $y = 13$ mm and $t = 0$ s. The distance of the laser beam from the free edge was maintained at 13 mm. Similar bead-on-plate experiments were conducted as standard tests to determine the hot cracking susceptibility of steels used in the automotive sector [11]. Random speckle patterns were applied on the top surface using a high temperature commercial paint. The paint can withstand temperature up to 1100 °C. The temperature during the welding was measured at several positions close to the fusion boundary by spot welded K type thermocouples.

A LIMESS Q-400-3D DIC system [13] along with a commercial software package Istra 4D was used to capture and analyse images at a frame rate of 8 Hz. Before carrying out image correlation on the specimen surface, calibration of the DIC cameras was carried out using 10 images of a translated and rotated checkerboard grid of known spacing. More information about the principle of the DIC method is available in chapter 3 (section 3.4). A typical emission spectrum of the laser plume on an iron based specimen is shown in Figure 4.1 (b) [12]. In order to minimise the effect of the intensity of the laser plume light, two auxiliary high intensity 30 W LEDs with a wavelength of 450 nm were used to illuminate the top surface of the specimen. Corresponding optical narrow bandpass filters

4
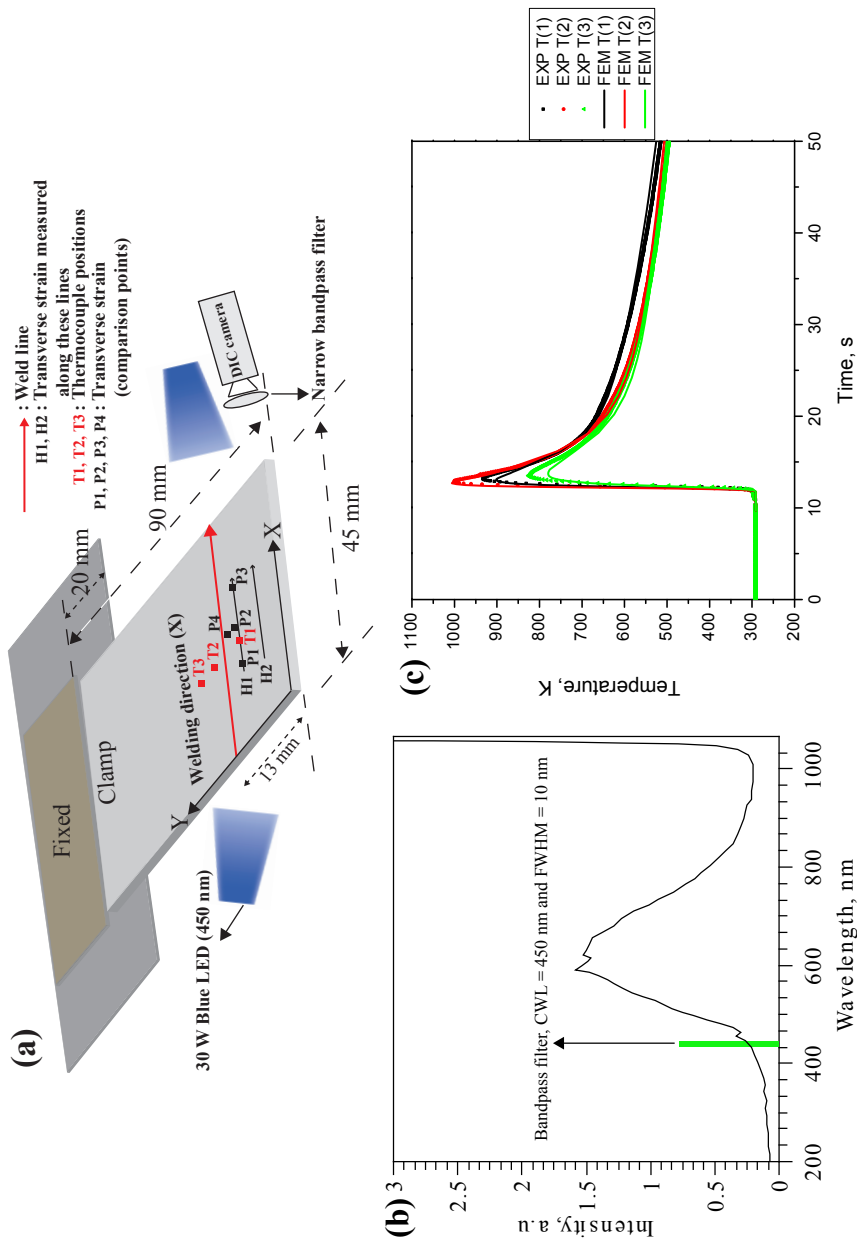
Figure 4.1: (a) Schematic of the laser bead-on-plate welding and DIC measurement setup, (b) typical emission spectrum of a Nd:YAG laser plume on an iron based specimen, replotted from reference [12]. The position of the optical narrow bandpass filter in this spectrum is also indicated and (c) simulated and experimental temperature cycle. Here, T(1) refers to the measured temperature cycle at a distance of 3 mm from the weld centreline towards the free edge. T(2) and T(3) are the measured temperature cycles at a distance of 2.5 mm and 4 mm from the weld centreline towards the constrained edge.

with a centre wavelength of 450 nm and a full width half maxima (FWHM) of 10 nm were placed in front of the lenses to minimise the effect of plume light. This approach allowed measurement of displacement fields as close as 1.5 to 2 mm from the fusion boundary.

4.3 Modelling approach

To complement the results from the DIC, a sequentially coupled 3D finite-element (FE)-based thermal mechanical model with isotropic hardening was developed to numerically calculate the temperature and the strain fields during welding. In the first step, a heat transfer analysis was conducted to retrieve the time dependent temperature field. A 3D conical heat source with Gaussian distribution. Subsequently, the temperature field history was applied as a thermal load for simulating the thermomechanical response of the material. Details of the mechanical model are discussed in chapter 3 (section 3.7). After validation, the FE-model can be used to ascertain strain fields in regions where laboratory experimental measurements are impractical.

4.4 Results and discussion

4.4.1 Temperature cycle during welding of TRIP steel

Figure 4.1 (c) shows the measured and simulated thermal cycle at thermocouple locations T(1), T(2) and T(3), respectively. T(1) refers to the measured temperature cycle at a distance of 3 mm from the weld centreline towards the free edge. T(2) and T(3) are the measured temperature cycles at a distance of 2.5 mm and 4 mm from the weld centreline towards the constrained edge. Good agreement was found between the experimental and simulated thermal cycles. Therefore, time-temperature profiles in the heat transfer model were subsequently imported to the thermomechanical model and the thermomechanical response of the material was simulated.

4.4.2 Transverse strain during welding of TRIP steel

Figure 4.2 (a) shows the spatial distribution of transverse strain (in %) at $t = 3.0$ s on a surface 2 mm from the fusion boundary. The top image shows the numerically computed distribution. The bottom image overlaying the speckle pattern shows the experimentally measured distribution. At some locations black spots are seen in the strain map. The measurement couldn't be performed at these locations due to data distortion caused by fume and spatter.

The transverse strain (TS) field during welding was measured at $t = 1.75$ s and $t = 2.25$ s, along lines H1 and H2 parallel to the weld (Figure 4.1 (a)) of length 20 mm and at a distance of 2 mm and 5.5 mm from the fusion boundary, respectively. The starting coordinates of lines H1, H2 are (10, 9.5) mm and (10, 6) mm, respectively. Temporal evolution of transverse strain was measured at points P1 (10, 9) mm, P2 (22.5, 10) mm and P3 (30, 9) mm. The coordinates of the points are mentioned in the brackets. Transverse strain data at these locations was also extracted from the FE-based numerical study.

Figures 4.2 (b) and (c) show both the experimentally measured and numerically computed distribution of transverse strain (in %) along lines H1 and H2 at $t = 1.75$ s and $t = 2.25$ s. The strain distribution measured by the DIC technique is comparable with the numerical results. Due to the optical filtering of the intense laser plume light,
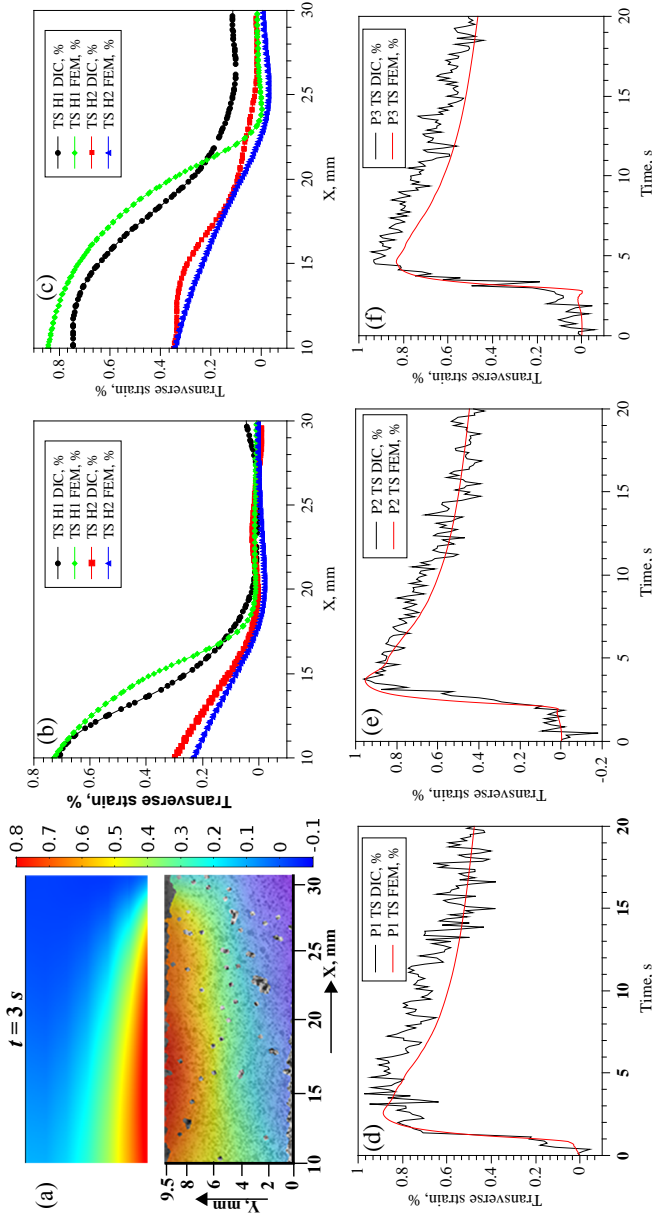
Figure 4.2: (a) Spatial distribution of transverse strain (in %) at $t = 3.0$ s. Top image shows the distribution calculated using the FE-based model. The bottom image overlaying the speckle pattern shows the strain distribution measured using the DIC technique. The coordinate system is the same as that used in Figure 4.1 (a), (b) experimentally measured and numerically computed spatial distribution of transverse strain (in %) along the line H1 and H2 at $t = 1.75$ s, (c) experimentally measured and numerically computed spatial distribution of transverse strain (in %) along the line H1 and H2 at $t = 2.25$ s, (d) experimentally measured and numerically computed temporal distribution of transverse strain (in %) at P1, (e) experimentally measured and numerically computed temporal distribution of transverse strain (in %) at P2 and (f) experimentally measured and numerically computed temporal distribution of transverse strain (in %) at P3.

4

a good spatial resolution close to the fusion boundary is achieved. Deviation of the numerically obtained transverse strain distribution along line H1 at $t = 2.25$ s compared to the experimental results could be due to the underestimated thermal conductivity. At $t = 1.75$ s, the laser beam is at a distance of 7.5 mm from the starting points of lines H1 and H2. At this time the measured transverse strain decreases at a rate of $\approx 6.8 \times 10^{-4} \mathrm{mm}^{-1}$ along the line H1, while it decreases at a rate of $\approx 2.9 \times 10^{-4} \mathrm{mm}^{-1}$ along the line H2. At a distance of ≈ 2.5 mm in front of the laser beam, the transverse strain is still zero. As the laser beam progresses further into the specimen, the transverse strain gradient along the H1 and H2 direction decreases.

Figures 4.2 (d), (e) and (f) show the measured and computed temporal transverse strain evolution at points P1, P2 and P3, respectively. The strain reaches a peak value when the laser beam approaches these positions. There is reasonable agreement between the experimental and numerical results. Numerically calculated peak transverse strain in the case of P3 was 0.0083 while the measured peak strain was 0.0093 Compared to P2 and P3, a large noise in transverse strain was observed at P1. This could be due to the loss of DIC data integrity close to P1 during welding. Error in displacement measurement of a subset occurs when comparing images with insufficient viable data. Other potential error sources of the DIC technique are mentioned in chapter 3 (section 3.4) and discussed in reference [14]. At $t = 90$ s, the calculated transverse strain and temperature at point P1 is 0.2 % and 409 K respectively.

The initial existence of steep gradients in transverse strain near the start of the weld increases the susceptibility to weld solidification cracking. In general, the amount of strain imposed on the weld metal is difficult to estimate due to complex geometric and thermal conditions [15]. Therefore, for evaluation of cracking tendency, controlled strain is applied on a geometrically simple specimen. Examples of tests satisfying this condition include the varestraint test, the PVR test (Programmierter Verformungsrisstest) and the sigmajig test [15]. However, the local conditions in the mushy zone that lead to solidification cracking are controlled, to a significant degree, by the development of the local macroscopic stress/strain conditions in the crack susceptible region [16]. The capability to measure strain (rates) close to the fusion boundary makes it possible to obtain information on strains in the weld region.

The two step approach of experimentally measuring the strain field and using a validated FE-based numerical model allows prediction of local critical stress/strain that leads to solidification cracking. As an example, the temporal evolution of transverse strain at a point P4 with coordinates (22.5, 10.5) mm, *i.e.* ~ 1 mm from the fusion boundary was calculated using the validated FE-based numerical model (Figure 4.3). To compare, temporal transverse strain evolution at P2 is also plotted. As expected, at P4 the transverse strain is higher than that at P2. The calculated maximum transverse strain near the weld centre is in the range of 3.2-3.6 %. It should be noted that only an estimate of the transverse strain can be made in the mushy region since the model does not take into account the strain localisation at the grain boundary of liquid films.
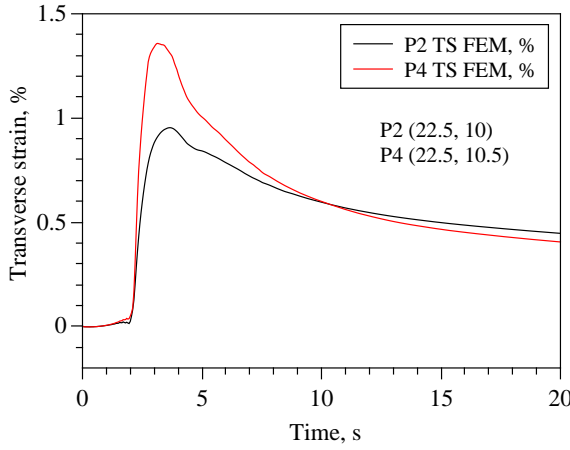
Figure 4.3: FEM computed temporal distribution of transverse strain (in %) at P2 and P4.

4.4.3 Transverse strain during welding of DP steel

The DIC technique was adopted to measure the transverse strain field during welding of DP steel sheets, utilising the same experimental arrangement and welding parameters as described in section 4.2. Figure 4.4 shows the spatial distribution of transverse strain (in %) at $t = 3.0$ s on a surface 2 mm from the fusion boundary. Figure 4.5 shows the measured temporal distribution of transverse strain at point P2 $(22.5, 10)$ mm. In comparison with the results shown in Figures 4.2 (a) and (d) for the TRIP steel, higher transverse strains exist near the fusion boundary during welding of the DP steel. The difference can be attributed to the different high temperature material properties of DP steel, which in turn depend on the composition and/or microstructure. Thermal mechanical modelling of the DP steel welds was not performed due to the lack of reliable temperature dependent mechanical property data.
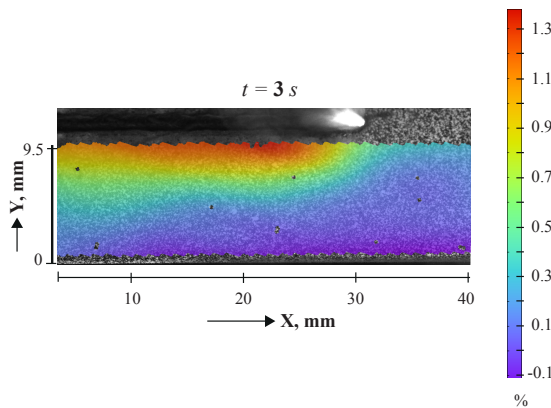
Figure 4.4: Transverse strain (in %) distribution at $t = 3.0$ s using the DIC technique.
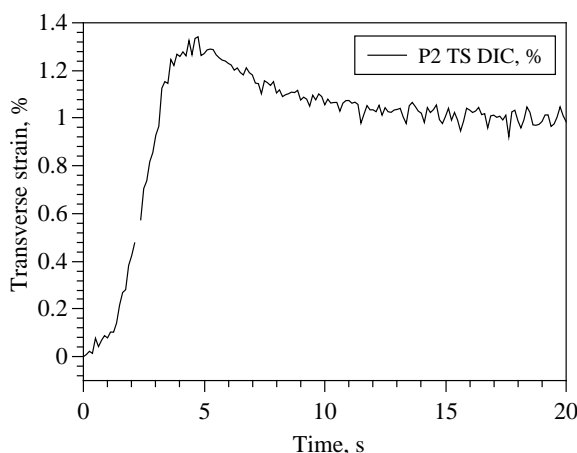
Figure 4.5: Experimentally measured temporal distribution of transverse strain (in %) at point P2.

4.5 Summary

In summary, an approach to measure *in-situ* strain fields on the top side of a welded specimen close to the fusion boundary has been introduced. This method, based on external illumination and filters allows measurement of strain fields with good spatial and temporal resolution as close as 1.5 mm to the fusion boundary. The results are in good agreement with the FE-based numerical model.

Solidification cracking will occur if the the strain imposed on the weld metal exceeds a certain threshold. In this regard, the validated FE-model is used in chapter 5 to study the effect of self-restraint on susceptibility to solidification cracking in TRIP steel.

References

[1] S. Kou, *Welding Metallurgy*, 2nd ed. (John Wiley & Sons, Inc., 2003) pp. 263–296.

[2] S. Kou, *A criterion for cracking during solidification,* Acta Materialia **88**, 366 (2015).

[3] M. A. Sutton, J.-J. Orteu and H. Schreier, *Image Correlation for Shape, Motion and Deformation Measurements: Basic Concepts, Theory and Applications*, 1st ed. (Springer Publishing Company, Incorporated, 2009).

[4] J. Kang, Y. Ososkov, J. Embury and D. Wilkinson, *Digital image correlation studies for microscopic strain distribution and damage in dual phase steels,* Scripta Materialia **56**, 999 (2007).

[5] C. Bumgardner, B. Croom and X. Li, *High-temperature delamination mechanisms of thermal barrier coatings: In-situ digital image correlation and finite element analyses,* Acta Materialia **128**, 54 (2017).

[6] N. Limodin, J. Réthoré, J.-Y. Buffière, F. Hild, S. Roux, W. Ludwig, J. Rannou and A. Gravouil, *Influence of closure on the 3D propagation of fatigue cracks in a nodular*

cast iron investigated by x-ray tomography and 3D volume correlation, Acta Materialia **58**, 2957 (2010).

[7] C. Gollnow and T. Kannengiesser, *Hot cracking analysis using in situ digital image correlation technique,* Welding in the World **57**, 277 (2013).

[8] M. De Strycker, P. Lava, W. Van Paepegem, L. Schueremans and D. Debruyne, *Measuring welding deformations with the digital image correlation technique,* Welding Journal **90**, 107S (2011).

[9] M. Shibahara, K. Yamaguchi, T. Onda, S. Itoh and K. Masaoka, *Studies on in-situ full-field measurement for in-plane welding deformation using digital camera,* Welding International **26**, 612 (2012).

[10] X. Chen and Z. Feng, *In situ strain evaluation during tig welding determined by backside digital image correlation,* Welding in the World **61**, 307 (2017).

[11] VDEh, *SEP 1220-3: Testing and Documentation Guideline for the Joinability of thin sheet of steel - Part 3: Laser beam welding*, edited by STAHL (2011).

[12] B. Aalderink, R. Aarts, J. Jonker and J. Meijer, *Weld plume emissions during nd:yag laser welding,* in *Lasers in manufacturing 2005*, edited by E. Beyer, F. Dausinger, A. Ostendorf and A. Otto (AT-Fachverlag GmbH Stuttgart, München, Germany, 2005) pp. 413–417.

[13] *LIMESS webpage, Retrieved (29-01-2019) from:* `https://www.limess.com/en/products/q400-digital-image-correlation#technical-specifications` (2017).

[14] B. Pan, K. Qian, H. Xie and A. Asundi, *Two-dimensional digital image correlation for in-plane displacement and strain measurement: a review,* Measurement Science and Technology **20**, 062001 (2009).

[15] V. Shankar, T. P. S. Gill, S. L. Mannan and S. Sundaresan, *Solidification cracking in austenitic stainless steel welds,* Sadhana **28**, 359 (2003).

[16] Z. Feng, S. A. David, T. Zacharia and C. L. Tsai, *Quantification of thermomechanical conditions for weld solidification cracking,* Science and Technology of Welding and Joining **2**, 11 (1997).

4

5

Solidification cracking investigation during laser welding in TRIP steel using experimental and numerical approaches[††‡‡]

SUSCEPTIBILITY to weld solidification cracking in transformation-induced plasticity steel sheets was studied using a modified standard hot cracking test used in the automotive industry. To vary the amount of self-restraint, bead-on-plate laser welding was carried out on a single-sided clamped specimen at increasing distances from the free edge. Solidification cracking was observed when welding was carried out close to the free edge. With an increasing amount of restraint, the crack length showed a decreasing trend, and at a certain distance, no cracking was observed. With the aid of a finite element-based model, dynamic thermal and mechanical conditions that prevail along the transverse direction of the mushy zone are used to explain the cracking susceptibility obtained experimentally. The results indicate that the transverse strain close to the fusion boundary can be used as a criterion to predict the cracking behaviour. The outcome of the study shows that by optimising the welding parameters, welds can be made without solidification cracking.

5.1 Introduction

Advanced high strength steels (AHSS) differs from mild steels in terms of chemical composition and microstructure. The higher alloying content in AHSS renders it susceptible

---

[††]G. Agarwal, H. Gao, M. Amirthalingam and M.J.M. Hermans, *Study of solidification cracking susceptibility during laser welding in an advanced high strength automotive steel*, Metals **8** (9), 673 (2018).

[‡‡]Some parts of the chapter are in, H. Gao, G. Agarwal, M. Amirthalingam, M.J.M. Hermans and I.M. Richardson, *Investigation on hot cracking during laser welding by means of experimental and numerical methods*, Welding in the World **62**, 71 (2018).

to solidification cracking during welding. During weld metal solidification, grains grow perpendicular to the fusion boundary since the temperature gradient is steepest, and accordingly, the heat extraction is maximised. The solidifying dendrites meet at the weld centreline. Upon solidification, the solidifying weld metal shrinks due to solidification shrinkage and thermal contraction. As solidification progresses, the solid in the mushy zone begins to form a rigid continuous network, *i.e.* tensile strain is induced by the surrounding material. If the deformation exceeds a certain threshold, separation of the dendrites at the grain boundary can occur. At the terminal stage of solidification, such an opening cannot be compensated by the remaining liquid due to both low permeability and a high solid fraction [1]. As a result, solidification cracking occurs. Solidification temperature range, segregation of impurity elements, morphology of solidifying grains, interdendritic liquid feeding and dendrite coherency are some of the important metallurgical aspects affecting the solidification cracking tendency [2]. The shrinkage-brittleness theory proposed by Pumphrey *et al.* [3] is based on the concept of coherency temperature. At the coherency temperature, the solid in the mushy region begins to form a rigid continuous network. The theory says that cracking occurs when there is some extent of coherency in the mushy region, *i.e.* below the coherency temperature. Pellini [4] proposed a strain-based theory for hot cracking in castings. This theory has been extended to weld solidification cracking and states that cracking occurs due to the rupture of liquid films that persist until the last stage of solidification. Building upon the work of Pellini, Prokhorov [5] considered the mushy zone as a single entity and defined the ductility of a material as solidification occurs. Later on, Zacharia [6] used the stress-based approach to describe the thermo-mechanical behaviour in the weld pool vicinity. Eskin *et al.* [7] in their review paper elaborated existing hot tearing theories and models. These models are based on the existence of a critical stress, critical strain or critical strain rate criterion, which leads to cracking. Recent physical models from Rappaz *et al.* [8] and Kou [9] indicate that in the presence of local deformation, insufficient liquid feeding in the interdendritic or intergranular region results in cracking. Matsuda *et al.* [10] and Coniglio *et al.* [11], based on the experiments, concluded that the presence of a critical strain rate is responsible for cracking. However, Katgerman [12] in his mathematical model considered stresses and insufficient feeding in the vulnerable temperature range to be the cause of hot cracking. Experiments focusing on determining the physical mechanism that leads to the separation of grains at the microscopic level under welding conditions are still lacking.

A typical car body has 40 m of weld flanges [13]. The flange width can be minimized by using laser welding and can lead to an overall weight reduction of up to 30–40 kg [13]. The distance from the free edge at which the welding is carried out is considered important for cracking behaviour in terms of the response of the material to the amount of restraint. In this study, a different approach was adopted compared to the standard hot cracking test. Different laser welding experiments were conducted at various starting positions from the free edge at an inclination of zero degrees, *i.e.* parallel to the free edge. This approach was followed,

- to maintain a constant restraint with respect to distance from the free edge during welding,

- to understand the effect of self-restraint on susceptibility to cracking,

- to identify the critical condition as a function of welding distance from the free edge in which no crack occurs,

- to develop an FE-based model to understand the process and delineate the critical factor(s) that may be responsible for the cracking behaviour.

5.2 Materials and methods

Weld solidification cracking susceptibility of TRIP steel sheets was studied using the aforementioned test arrangement. Crack length was measured for each case, and the fracture surface was observed by scanning electron microscopy. The validated finite element (FE)-based thermal mechanical model of the welding, as described in chapter 4 and chapter 3 (section 3.7), was used to substantiate the results obtained from experiments. The occurrence of a crack was not simulated explicitly. Rather, the accumulated transverse strain along the direction perpendicular to the weld was used to assess the solidification cracking susceptibility. Based on the developed understanding, optimum processing conditions can be defined to weld steels that are otherwise susceptible to solidification cracking.

5.2.1 Experimental conditions

A 3 kW Nd:YAG laser was used as the heat source. The bead-on-plate laser welding experiments were conducted in keyhole mode using a power of 1100 W and a welding speed of $10 \, \text{mm s}^{-1}$. Specimens were kept at the focal point of the optical system, and the laser spot size was 0.45 mm. The experimental arrangement is shown schematically in Figure 5.1. The coordinate system used in the FE model is also included. The dimensions of the rectangular steel sheets were $90 \times 45 \, \text{mm}^2$ and 1.25 mm thick. For all the experiments, the starting beam position was at $x = 0$ mm, and welding was carried out along the x direction. The starting y ordinate for different experiments was varied from 3 mm to 13 mm with each increment being 2 mm. Each experiment was repeated with a fresh plate at least three times. The experiment at 5 mm was repeated ten times. Hereafter, each experiment at a certain distance from the free edge is referred to as "y mm" case, where y refers to the starting y ordinate in each experiment. Images during welding were captured using a high-speed camera, the procedure of which is described in chapter 3 (section 3.3). For the 13 mm case, the temperature cycle was measured at three Positions (P1, P2 and P3) near the fusion boundary, by using spot welded K-type thermocouples. Furthermore, the evolving transverse strain near the weld fusion boundary was measured *in-situ* using the digital image correlation method [14], as discussed in chapter 4. The width of the weld bead was approximately 2.8 mm. The length of the weld centreline crack was measured for each case. The fracture surface of the crack was observed with a JEOL 6500F scanning electron microscope (JEOL, Tokyo, Japan). Additional experiments were conducted with different heat input for the 13 mm, 11 mm, 9 mm and 7 mm cases. Heat input was varied by changing the welding speed to $11 \, \text{mm s}^{-1}$, *i.e.* 10 % decrease in heat input, $12 \, \text{mm s}^{-1}$, *i.e.* 20 % decrease in heat input, and $9 \, \text{mm s}^{-1}$, *i.e.* 10 % increase in heat input. The overall experimental scheme is listed in Table 5.1.
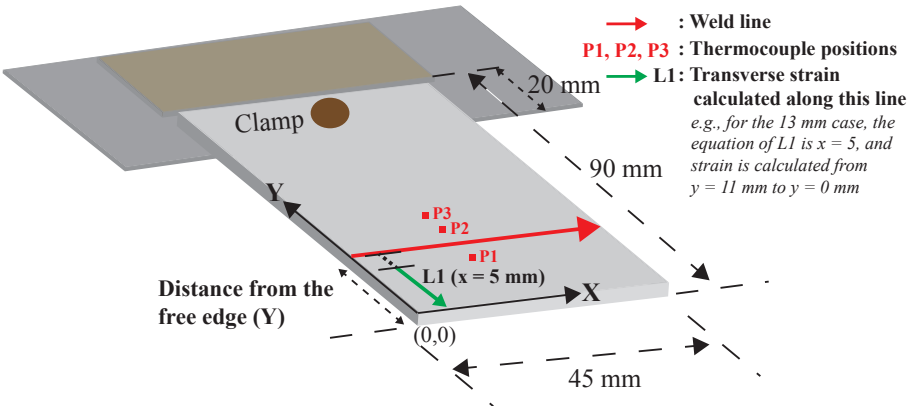
Figure 5.1: Schematic of the hot cracking test arrangement.

Table 5.1: Experimental scheme.

Welding Distance (Y ordinate, mm)	Welding Parameters	
	Laser Power (W)	Speed (mm s^{-1})
3, 5, 7, 9 and 11	1100	10
		11
		12
13	1100	9
		10
		11
		12

5.2.2 Modelling approach

A sequentially-coupled 3D finite element (FE) thermal mechanical model was utilized for laser bead-on-plate welding, details of which were discussed in chapter 3 (section 3.7).

5.3 Results

Figure 5.2 shows the experimental and simulated thermal cycle at points P1, P2 and P3, when welding was carried out at a distance of 13 mm from the free edge. The position of the points P1, P2 and P3 with respect to the weld centreline is also indicated in the figure. P1 is at a distance of 3 mm (towards the free edge), while P2 and P3 are at 2.5 mm and 4 mm (towards the fixed edge). The maximum difference between the experimental and simulated temperature is 4.9 %, and the standard deviation is 2 %. The simulated weld bead size of 2.3 mm was found while the experimental weld bead size was 2.5 mm. Thereafter, the thermal history from the heat transfer model was applied in the mechan-

ical analysis. The thermomechanical model was validated using the transverse strain measured by the digital image correlation method [14].
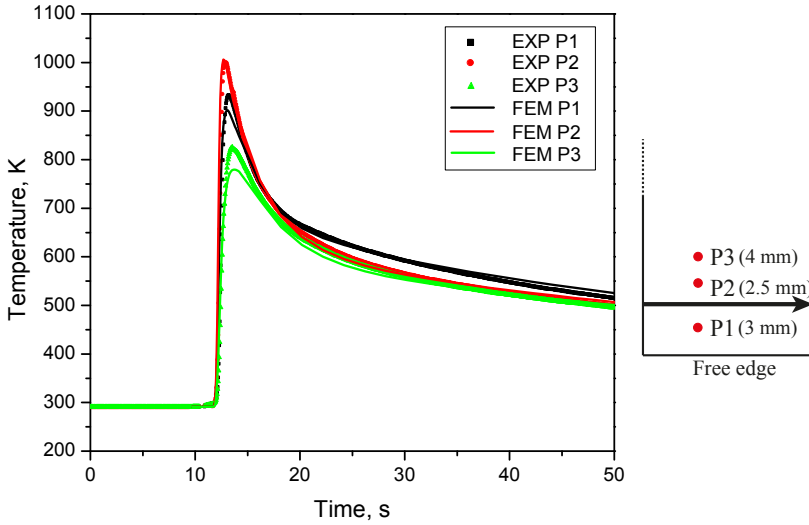
Figure 5.2: Experimental and calculated temperature cycles for the 13 mm case. The position of the points P1, P2 and P3 with respect to the weld centreline is also indicated. P1 is at a distance of 3 mm (towards free edge), while P2 and P3 are at 2.5 mm and 4 mm (towards the fixed edge).

5.3.1 Observation of solidification cracking

Figures 5.3 (a) and (b) show high speed camera images captured while welding was carried out for the 5 mm case. It is clear from these images that crack formation occurs during welding, and the crack follows the trailing edge of the mushy zone. Figure 5.3 (c) shows the image when welding was carried out at a distance of 7 mm from the free edge. After a certain distance, the crack ceased to propagate. The videos are embedded in the PDF version of this dissertation in Figure 5.4 and Figure 5.5 for the 5 mm and 7 mm cases, respectively. The measured average crack length and the standard deviation for different cases and heat inputs are shown in Figure 5.6. For the 5 mm case, fracture was observed along the entire weld in all experiments. On further increase of the distance from the free edge, the crack length decreased, and for the 13 mm case (and onwards), no solidification cracks were observed. With a 10 % decrease in heat input, the crack length reduced for the 7 mm and 9 mm cases, while no crack was observed for the 11 mm case. With a 20 % reduction in heat input, the crack length reduced further for the 7 mm case, and no crack was observed for the 9 mm case. When the heat input was increased by 10 %, a crack was also observed in the 13 mm case. The run-on plate was not used in the experiments, the use of which may effect the crack initiation. The standard hot cracking test does not mention the use of run-on and run-off plates.

The fracture surface of welded TRIP steel sheet was studied by means of scanning electron microscopy. Figure 5.7 (a) indicates that a liquid film entrapped between the dendrites led to cracking. This is an important observation as it helps to conclude that

the cracks are indeed formed during the terminal stage of solidification. Figure 5.7 (b) shows microcracks, which occur at the last stage of solidification on the dendrite tips.

The high speed camera and SEM images both corroborate the previous studies on solidification cracking [7]. Moreover, it is apparent that a material is most susceptible to cracking when the fraction of solid (f_s) becomes close to one [8, 9, 15].

Identical hot cracking tests were performed on Dual Phase (DP) steel sheets and solidification cracking was not observed in any of the cases. The aspects contributing to a high resistance of DP steel to solidification cracking are discussed in chapter 8.
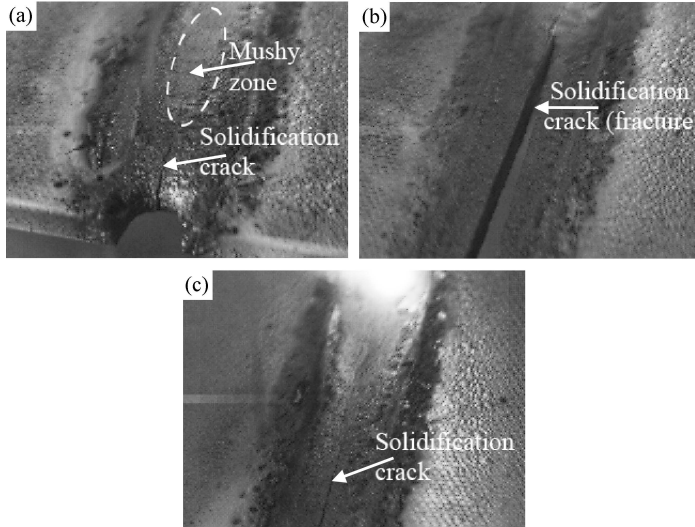
Figure 5.3: High-speed camera images showing solidification cracking during welding. (a) Solidification crack initiating at the trailing edge of the mushy zone (5 mm case), (b) full fracture observed (5 mm case) and (c) the solidification crack stops propagating further (7 mm case). The weld bead size is 2.5 mm.

Figure 5.4: High-speed camera video showing solidification cracking during welding for the 5 mm case, in which complete fraction was observed. The weld bead size is 2.5 mm.

Figure 5.5: High-speed camera video showing solidification cracking during welding for the 7 mm case, in which the cracks propagation stops after some time. The weld bead size is 2.5 mm.

5
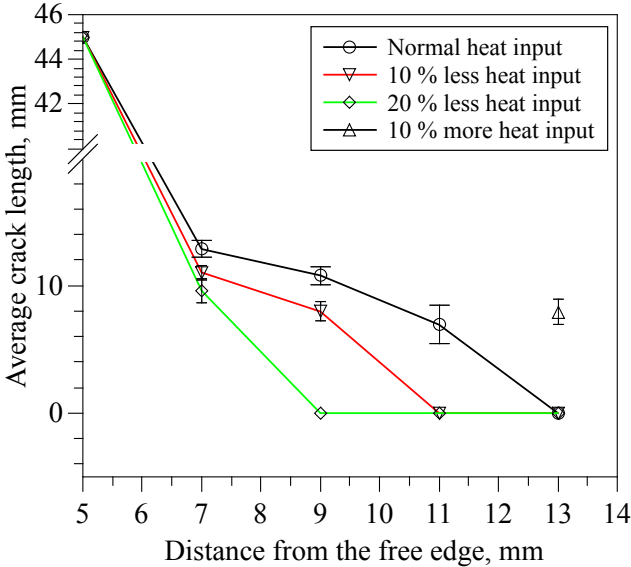
Figure 5.6: Measured crack length as a function of welding distance from the free edge. For the normal heat input, a laser power of 1100 W and a travel speed of 10 mm s^{-1} was used. For 10 % and 20 % less heat input, the travel speed was increased to 11 mm s^{-1} and 12 mm s^{-1}, respectively. For 10 % more heat input, the travel speed was reduced to 9 mm s^{-1}.
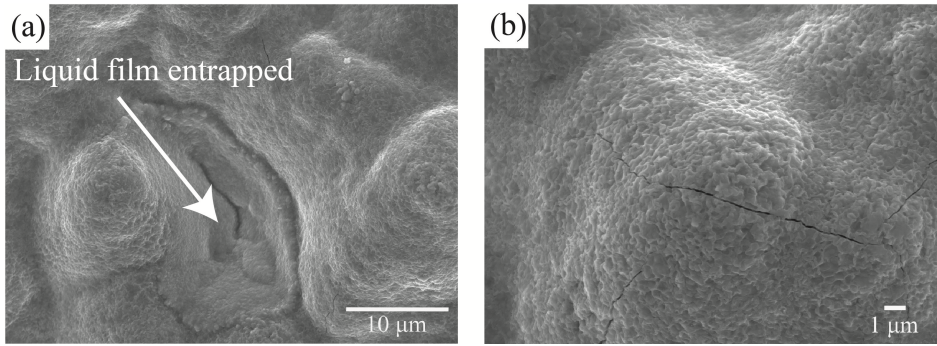
Figure 5.7: Micrographs of the fracture surface of TRIP steel (5 mm case). (a) Liquid film entrapped between dendrites that lead to cracking and (b) micro-cracks on the dendrite tip.

5.3.2 Thermomechanical analysis of the process

Figure 5.8 shows the simulated results of peak temperature at the weld centreline as a function of distance for the 5 mm case. Due to the introduction of the heat source, the peak temperature is low at the beginning. The peak temperature reaches the steady state after approximately 5 mm ($x = 5$ mm). However, due to accumulation of heat, a higher peak temperature is reached towards the last 2–3 mm. Thermal and transverse strain analysis was conducted under the steady state regime at $x = 5$ mm along the y direction. Transverse strain data along a line L1 (Figures 5.1 and 5.9) with starting point 2 mm from the weld centreline was extracted from the simulation results. The region in the mushy zone and the prevailing conditions where the analysis was performed are shown schematically in Figure 5.9 at $t = 1$ s. At $t = 1$ s and $x = 5$ mm, the fraction of solid (f_s) approaches one at the weld centreline. Temperature and transverse strain along the line L1 were extracted at various times. Using the constitutive behaviour, the total transverse strain can be decomposed as:

$$\epsilon^{Tot} = \epsilon^{el} + \epsilon^{pl} + \epsilon^{th} \tag{5.1}$$

Here, ϵ^{Tot} is the total transverse strain and terms on the right hand side are the elastic, plastic and thermal transverse strains, respectively. Note that the volumetric strain due to phase transformation is included in the linear coefficient of thermal expansion.

Figures 5.10 (a) and (b) show the temperature as a function of distance along L1 (starting point 2 mm from the weld centreline) at $t = 0.5$ s and $t = 1$ s repectively, for different experimental cases. With progressing time, the transverse strain close to the fusion boundary increases. Figure 5.10 (c) shows the simulated elastic, plastic, thermal and total transverse strain for the 5 mm case. Here, the thermal strain includes the contribution from solidification shrinkage, thermal contraction and phase transformation. From this figure, it can be inferred that the elastic and plastic strains are small compared to the thermal strain. It is thus the thermal strain that forms the most significant portion of the total strain. Note that the viscoplastic effect of the material at high temperature is not considered in this work. Safari *et al.* [16] found the effect of viscoplasticity on the total transverse strain to be negligible. Figures 5.10 (d) and (e) show the transverse strain (in %) as a function of distance along L1 at $t = 0.5$ s and $t = 1$ s respectively, for different

experimental cases. At $t = 1$ s, the transverse strain is a maximum at the starting point of line L1 for the 3 mm case and decreases as the welding distance from the free edge is increased. For the 13 mm case; in which no crack was observed, the threshold transverse strain is ≈ 1.7 %.
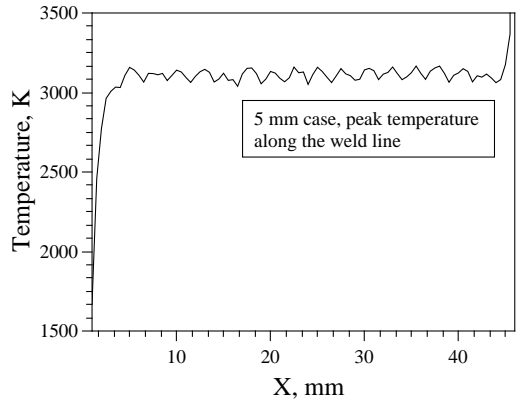
Figure 5.8: Simulated peak temperature along the weld centreline for the 5 mm case.
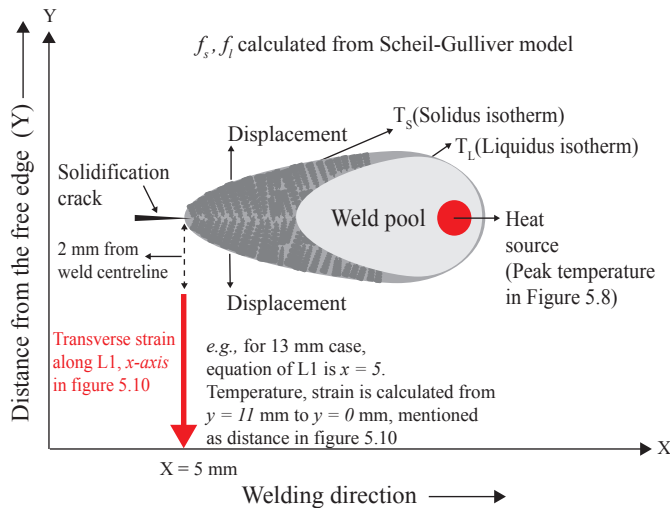
Figure 5.9: Schematic showing the prevailing conditions at $t = 1$ s. The thermomechanical analysis was performed along the line L1 at $t = 0.5$ s and $t = 1$ s.
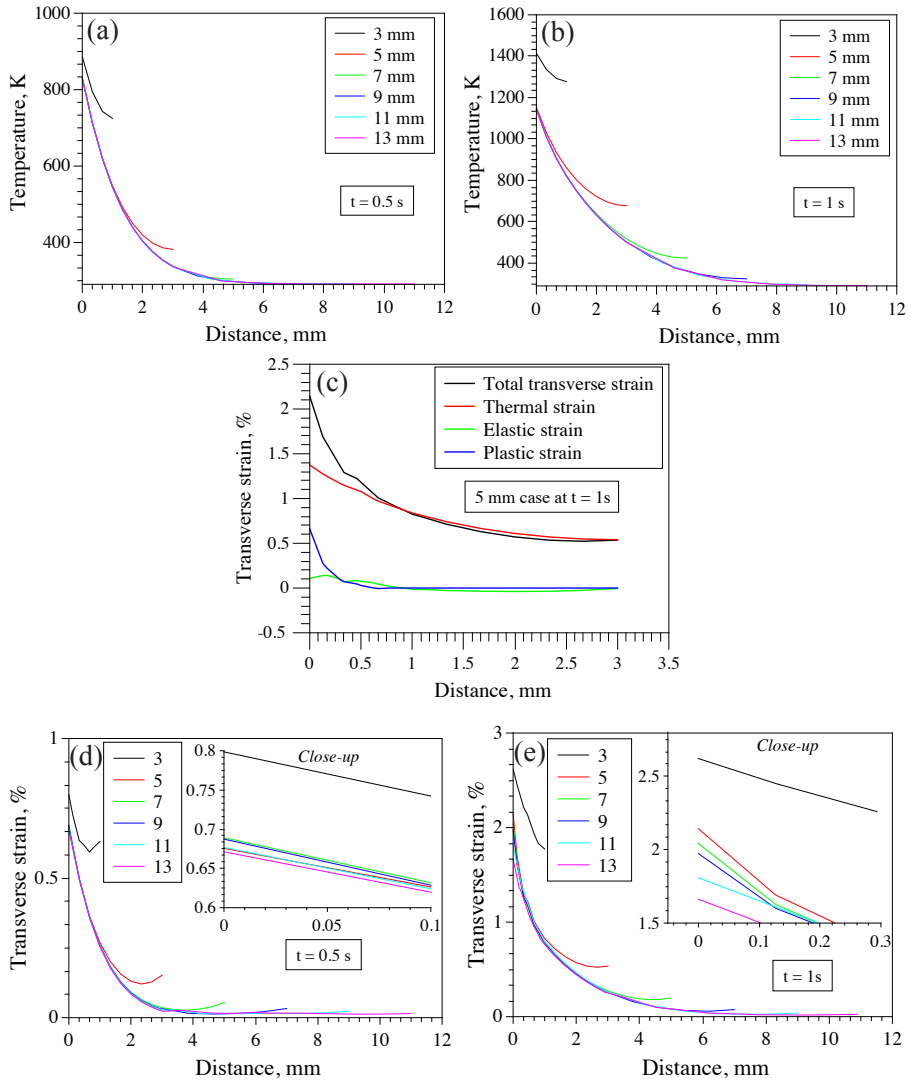
Figure 5.10: (a) simulated temperature field along L1 at $t = 0.5$ s for different cases, (b) simulated temperature field along L1 at $t = 1$ s for different cases, (c) simulated strain contributions and total strain for the 5 mm case, (d) simulated transverse strain (in %) along L1 for different cases at $t = 0.5$ s and (e) simulated transverse strain (in %) along L1 for different cases at $t = 1$ s.

5.3.3 Effect of heat input on transverse strain and crack susceptibility

To study the effect of heat input on the transverse strain, the travel speed was varied in the FE model. The maximum transverse strain for the 11 mm case (Figure 5.11 (a)) with 10 % less heat input was ≈1.6 %, *i.e.* lower than the threshold strain of the 13 mm case in which no cracking was observed. With 20 % less heat input, the maximum transverse strain for the 9 mm case was ≈1.5 %, *i.e.* below the threshold strain, while with 10 % less heat input, the maximum transverse strain was ≈1.8 %, *i.e.* above the threshold strain (Figure 5.11 (b)). For the 7 mm case, the maximum transverse strain was higher than the threshold strain for both 10 % and 20 % reduced heat input. For the 13 mm case, with 10 % higher heat input, the maximum transverse strain increased to 2.1 %, as shown in Figure 5.11 (c).
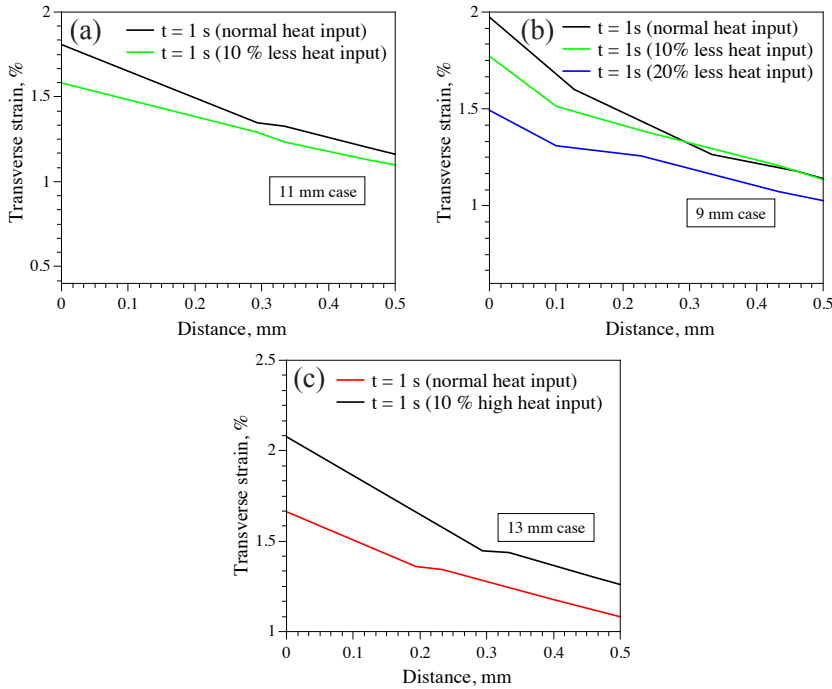
Figure 5.11: Effect of heat input on the transverse strain along L1 at $t = 1$ s. (a) The 11 mm case with normal and 10 % less heat input, (b) 9 mm case with normal and 10 % and 20 % less heat input and (c) 13 mm case with normal and 10 % high heat input.

In order to test the effect of heat input on cracking susceptibility, welding experiments were conducted with different travel speeds. A reversal in cracking tendency was observed; no crack was observed in the 11 mm case with 10 % less heat input, and no crack was observed in the 9 mm case with 20 % less heat input. With 10 % higher heat input, a crack was observed even in the 13 mm case. The average crack length as a function of distance from the free edge for different heat inputs is shown in Figure 5.6.

5.4 Discussion

The measured temperature cycles at the thermocouple positions and the simulated results show good agreement (Figure 5.2). Furthermore, the slow heat dissipation (or heat accumulation) due to a reduced amount of material towards the free edge is captured well in the simulated thermal cycles. The experimental fusion zone dimensions were also found to be in agreement with the simulated ones.

The maximum transverse strain along line L1 decreases from the 3 mm case to the 13 mm case. This result agrees well with the cracking susceptibility observed experimentally. It is observed that as the degree of self-restraint increases, the susceptibility to solidification cracking decreases, which is consistent with earlier studies [17, 18]. With the increase in welding distance, more material remains at low temperature (closer to the free edge) and resists deformation close to the fusion boundary. This leads to a difference in transverse strain (insert in Figure 5.10 (e)) and hence in cracking tendency.

For the 13 mm case, no solidification cracks were observed, and the maximum transverse strain along L1 is ≈1.7 %. This value can be used as a safety factor to avoid solidification cracking in the steel tested in this work, *i.e.* a threshold value. A lower heat input reduces the thermal strain along line L1. Since thermal strain contributes significantly towards the total transverse strain (refer to Figure 5.10 (c)), the overall transverse strain decreases. This leads to a reduction in the critical distance from the free edge at which no solidification cracking occurs. Reduction of heat input by 10 % decreases the critical distance by 2 mm, while a 20 % reduction decreases it by 4 mm. An increase in travel speed allows a reduction of the flange width and enables sound welds to be made in materials that are otherwise susceptible to solidification cracking.

Tensile strains are built up behind a moving weld pool due to both solidification shrinkage and thermal contraction [6, 19]. Solidification cracking occurs when the resistance of a material to cracking is overridden by the mechanical driving force for cracking. Generally, the Brittle Temperature Range (BTR) of an alloy, the temperature range over which cracking is found to occur, is used as a measure of susceptibility to solidification cracking. Sometimes, BTR is also defined as the difference between liquidus and solidus temperatures [20]. Senda *et al.* [21] and later on Nakagawa *et al.* [22], using the trans-varestraint test, measured temperatures at the tail of the weld pool by plunging thermocouples. The BTR was assumed to be proportional to the maximum crack length and was defined as the temperature difference between the two extremities of the crack. However, large disparities exist in the BTR of the same material [23], raising issues with the accuracy of the method. BTR, being a material-dependent parameter, is essentially constant for the steel investigated in this study. Therefore, BTR alone cannot explain the different cracking behaviour. Clyne *et al.* [24] reported that the cracking susceptibility index of an alloy is directly related to the freezing time. Freezing time at the weld centre was extracted from the simulated thermal histories of two cases, first the 9 mm case with normal heat input, *i.e.* in which a crack was observed, and second, the 9 mm case with a 20 % reduction in heat input, *i.e.* in which no crack was observed. Liquidus and solidus temperatures were taken from the Scheil-Gulliver non-equilibrium solidification model (Figure 5.12). The freezing time for the first case is 0.25 s, while for the second case, it is 0.16 s. Reduction in heat input leads to higher cooling rates, and thus, the freezing time decreases. In the second case, the material spends less time in the vulnerable cracking
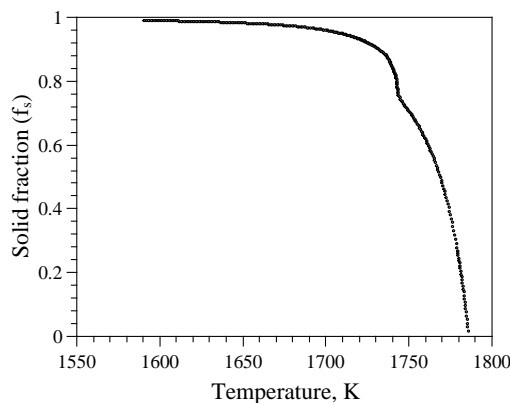
Figure 5.12: Solid fraction (f_s) versus temperature for the TRIP steel calculated using the non-equilibrium Scheil-Gulliver solidification model.

regime and therefore is less susceptible to cracking. To compare, the freezing time was also extracted for the 13 mm case with normal heat input and was found to be 0.25 s. No crack was observed in this case. It can be inferred that freezing time can only be used as a cracking susceptibility index when the mechanical restraint conditions do not change, and therefore, only relative tendencies can be compared.

Although implicit, the calculation of macroscopic strain using the FE method is based on continuum mechanics. Thus, the cracking process that occurs at the microscopic level is directly related to the local macroscopic stress/strain development in the crack vulnerable regime [25]. This approach accounts for both the thermal histories and the related mechanical response of the material.

5.5 Conclusions

1. With the use of the presented hot cracking test, in general, any given material is most susceptible to solidification cracking when welding is carried out close to the free edge. As the distance from the free edge increases, *i.e.* the degree of self-restraint increases, the susceptibility to cracking decreases.

2. The FE simulation study shows that macroscopic transverse strain near the mushy zone can be used as an indicator to explain the experimentally-observed cracking susceptibility with regards to crack length.

3. A threshold transverse strain at a point close to the fusion boundary is determined for which no cracking was observed. It is further validated by varying the heat input both in the model and the experiments.

4. Reducing the heat input decreases the susceptibility to solidification cracking or, in other words, it decreases the critical distance from the free edge at which cracking does not occur.

5.6 Outlook

In this chapter, transverse strain close to the fusion boundary is used as an indicator of susceptibility to solidification cracking. Metallurgical factors like solidification morphology, fluid flow in the mushy region, solute segregation, effective solidification temperature range were not explicitly considered. For this purpose, solidification of TRIP and DP steel was studied *in-situ* using high temperature laser scanning confocal microscopy, under simulated welding conditions. The results, discussed in the following chapters, shed light on the dominating aspects which render TRIP steel inherently prone to solidification cracking.

References

[1] M. Rappaz and J. Dantzig, *Solidification*, 1st ed. (EFPL Press, 2009) pp. 519–563.

[2] S. Kou, *Welding Metallurgy*, 2nd ed. (John Wiley & Sons Inc., 2003) pp. 263–296.

[3] W. I. Pumphrey and P. H. Jennings, *A consideration of the nature of brittleness and temperature above the solidus in castings and welds in aluminum alloys,* Journal of the Institute of Metals **75**, 235 (1948).

[4] W. S. Pellini, *Strain theory of hot-tearing,* Foundry **80**, 124 (1952).

[5] N. N. Prokhorov, *The problem of the strength of metals while solidifying during welding,* Svar Proiz **6**, 5 (1956).

[6] T. Zacharia, *Dynamic stresses in weld metal hot cracking,* Welding Journal (Miami, Fla) **73**, 164S (1994).

[7] D. G. Eskin and L. Katgerman, *A quest for a new hot tearing criterion,* Metallurgical and Materials Transactions A **38**, 1511 (2007).

[8] M. Rappaz, J. M. Drezet and M. Gremaud, *A new hot-tearing criterion,* Metallurgical and Materials Transactions A **30**, 449 (1999).

[9] S. Kou, *A criterion for cracking during solidification,* Acta Materialia **88**, 366 (2015).

[10] F. Matsuda, H. Nakagawa, K. Nakata and H. Okada, *The VDR cracking test for solidification crack susceptibility on weld metals and its application to aluminum alloys,* Transactions of JWRI **8**, 85 (1979).

[11] N. Coniglio and C. Cross, *Mechanisms for solidification crack initiation and growth in aluminum welding,* Metallurgical and Materials Transactions A **40**, 2718 (2009).

[12] L. Katgerman, *A mathematical model for hot cracking of aluminum alloys during d.c. casting,* JOM **34**, 46 (1982).

[13] M. A. Omar, *Automotive joining,* in *The Automotive Body Manufacturing Systems and Processes* (Wiley-Blackwell, 2011) Chap. 3, pp. 107–176.

[14] G. Agarwal, H. Gao, M. Amirthalingam and M. J. M. Hermans, *In-situ strain investigation during laser welding using digital image correlation and finite element based numerical simulation,* Science and Technology of Welding and Joining **23**, 134 (2018).

[15] M. M'Hamdi, A. Mo and H. G. Fjær, *TearSim: A two-phase model addressing hot tearing formation during aluminum direct chill casting,* Metallurgical and Materials Transactions A **37**, 3069 (2006).

[16] A. Safari, M. Forouzan and M. Shamanian, *Hot cracking in stainless steel 310s, numerical study and experimental verification,* Computational Materials Science **63**, 182 (2012).

[17] C. E. Cross and T. Boellinghaus, *The effect of restraint on weld solidification cracking in aluminium,* Welding in the World **50**, 51 (2006).

[18] G. Goodwin, *Development of a new hot-cracking test - the sigmajig,* Welding Journal (Miami) **66:2**, 33s (1987).

[19] Z. Feng, *A computational analysis of thermal and mechanical conditions for weld metal solidification cracking,* Welding in the World **33**, 340 (1994).

[20] C. E. Cross, *On the origin of weld solidification cracking,* in *Hot Cracking Phenomena in Welds*, edited by T. Böllinghaus and H. Herold (Springer Berlin Heidelberg, 2005) pp. 3–18.

[21] T. Senda, F. Matsuda, G. Takano, K. Watanabe, T. Kobayashi and T. Matsuzaka, *Fundamental investigations on solidification crack susceptibility for weld metals with trans-varestraint test,* Transactions of JWRI **2**, 141 (1971).

[22] H. Nakagawa, K. Sorada and F. Matsuda, *Dynamic observation of solidification and solidification cracking during welding with optical microscope (i) : Solidification front and behavior of cracking,* Transactions of JWRI **11**, 67 (1982).

[23] N. Coniglio and C. E. Cross, *Towards establishment of weldability testing standards for solidification cracking,* in *Cracking Phenomena in Welds IV*, edited by T. Boellinghaus, J. C. Lippold and C. E. Cross (Springer International Publishing, Cham, 2016) pp. 37–66.

[24] T. W. Clyne, M. Wolf and W. Kurz, *The effect of melt composition on solidification cracking of steel, with particular reference to continuous casting,* Metallurgical Transactions B **13**, 259 (1982).

[25] Z. Feng, S. A. David, T. Zacharia and C. L. Tsai, *Quantification of thermomechanical conditions for weld solidification cracking,* Science and Technology of Welding and Joining **2**, 11 (1997).

5

6

Study of solidification cracking in TRIP steel using high temperature microscopy and phase field modelling§§

6.1 Introduction

TRANSFORMATION induced plasticity steels (TRIP) with strengths over 600 MPa, possess increased formability due to the TRIP effect [1]. The TRIP effect is achieved when metastable austenite transforms to martensite upon deformation. Matsumura [2, 3] proposed the TRIP effect in low alloyed steel with a composition of C 0.2, Mn 1-2 and Si 1-2 (in wt. %). Silicon aids the TRIP effect by inhibiting cementite formation. However, an increase in the Si content beyond 0.5 wt. % reduces the galvanizability by forming silicon oxide [4]. Both Al and P, are known to retard cementite formation and partially substitute Si. Phosphorus addition increases the amount of retained austenite and additions of 0.1 wt. % P stabilize small austenite grains, even at 100 K [5]. In addition, P is also an effective solution strengthening element [6, 7] and addition of up to 0.25 wt. % is considered beneficial with regard to the TRIP effect [7–9].

Apart from formability requirements in these steels, welding is an important fabrication method for automotive applications. From the standpoint of possible welding defects [10], preventing solidification cracking is an essential prerequisite for the safety of welded components.

Weld solidification of an alloy involves the coexistence of a solid and a liquid phase, *i.e.* a mushy zone. The mushy zone generally comprises columnar dendrites separated by

---

liquid. Due to a temperature gradient in the mushy zone, the solid deforms due to both solidification shrinkage and non-uniform thermal contraction; as a consequence, tensile strains are induced in the semi-solid region. During the initial stage of solidification, grains are isolated and can accommodate tensile deformation by reorientation/rotation [11]. At the terminal stage of solidification, *i.e.* when the fraction of solid (f_s) approaches 1, the grains coalesce leading to a solid network separated by isolated liquid pockets. The material at this stage possess adequate strength and ductility and therefore has good resistance to cracking. However, prior to this stage, the grains are separated by films of the remaining liquid and hence the material possess a low strength [12]. Any separation at the grain boundary due to thermal strain is difficult to compensate with flow of the remaining liquid owing to low permeability; this can lead to solidification cracking or hot tearing. Solidification cracking has been studied for several decades [13–18] in different alloy systems. The onset of solidification cracking involves a complex interplay between interlinked factors namely; the solidifying microstructure, the weld thermal cycle and the surrounding restraint. A unified model to explain the solidification cracking phenomenon is still evolving.

Liquid feeding is an important factor that helps to avoid solidification cracking and likewise, is included in most of the models [14, 15, 19]. Early work by Feurer [19] examined the rate of feeding and the rate of shrinkage effects on hot cracking phenomenon. Cracking occurs during solidification, if the rate of feeding of the liquid in the interdendritic region is less than the rate of shrinkage of the solid being formed. The feeding ability is directly linked to the properties of solidifying microstructure; *e.g.* solidification morphology, composition, segregation of the solute *etc.*

Owing to the experimental complexity involved in studying high-temperature phenomena involving both the solid and liquid phases, most of the studies on solidification cracking are conducted *ex-situ*. Externally loaded tests like the varestraint test [10] and the PVR (programmable deformation rate) test [20] focus (primarily) only on determining the critical amount of applied strain (rate) or total crack length for assessing weldability, while underlying factors such as solidifying microstructure are not considered. To address this issue, an *in-situ* observation technique, namely high-temperature laser scanning confocal microscopy, was employed in this work. This technique is generally used to study *in-situ* solidification events like peritectic [21] and solid-state phase transformations; details of which can be found in the literature [22, 23].

In this study, a circular melt pool was formed at the center of a thin circular disk specimen while the outer rim remained solid. The solid outer rim acts as a restraint to the solidifying melt pool. Similar restraint conditions exist in welding; tensile strain is imposed on the solidifying weld metal by the surrounding cold material. Cracking was observed during the terminal stage of solidification. Segregation of the alloying elements phosphorus and carbon in the interdendritic region near the crack was studied using atom probe tomography (APT), which provided three-dimensional (3D) mapping of alloying elements with near-atomic resolution [24]. The results are compared with a phase field model and further discussed pertaining to the effect of P on solidification cracking.

6.2 Experimental procedures and modelling method

A TRIP steel sheet with a composition, C 0.19, Mn 1.63, Al 1.1, Si 0.35, P 0.089 (all in wt. %) was examined in this study. The liquidus temperature of the steel was calculated to be 1786 K (1513 °C) using the commercial thermodynamic software Thermo-Calc[TM]. Circular disk specimens with a diameter of 10 mm and a thickness of 250 μm were prepared using electro-discharge machining. Each specimen was placed in an alumina crucible. To minimise direct contact with the crucible, the sample was held by ceramic protrusions on the circumference. The crucible in turn was held in a platinum holder. A B-type thermocouple wire was welded to the platinum holder. Specimens were placed at the upper focal point of a gold plated ellipsoidal cavity in an infra-red furnace beneath a quartz view port under an ultra-high purity inert gas atmosphere, >99.9999% Ar. A 1.5 kW halogen lamp located at the lower focal point in the cavity heats the specimen by radiation. The power input to the halogen lamp is controlled by an Omron ES100P digital PID controller, which in turn was connected to the thermocouple at the crucible holder for a feedback signal. The temperature measured by the thermocouple incorporated in the crucible holder was recorded while simultaneously, optical images were recorded at a rate of 30 frames per second. Further details on the heating arrangement, temperature measurements *etc.* can be found in chapter 3 (section 3.5) and references [23, 25]. A stable melt pool with a diameter between 3 to 3.5 mm was obtained at the center of the specimen while the outer rim remained solid. A cooling rate of $10\,\mathrm{K\,s^{-1}}$ was employed until 1623 K (1350 °C). To obtain an approximation of the actual temperature in the liquid pool, calibration experiments with pure iron samples were conducted and a difference of 212 K was found between the thermocouple reading at the sample holder and the melting point of iron, taken as 1811 K (1538 °C). Figure 6.1 shows the solidification images of IF steel (considered as pure Fe), conducted for the temperature calibration.
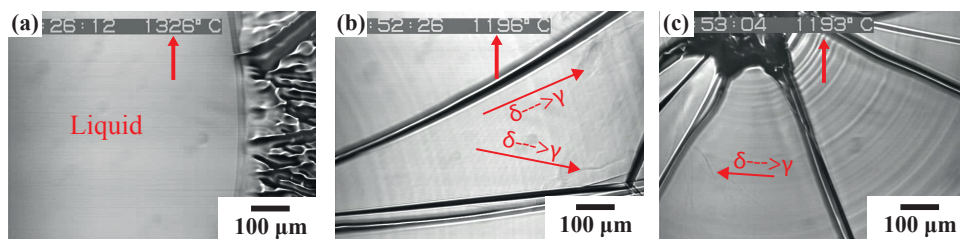
Figure 6.1: Temperature calibration experiments with IF steel. (a) liquid pool of similar size as that of TRIP steel was created. Temperature difference of 212 K from the melting point of pure Fe (1811 K), (b) delta ferrite to austenite transformation starts near the original S/L interface, identified by a change in the surface morphology due to the higher density of austenite. Temperature difference of 198 K was observed (compared with delta ferrite to austenite transformation temperature of 1667 K (1394 °C) for pure Fe) and (c) delta ferrite to austenite transformation starts near the centre. Temperature difference of 201 K was observed (compared with 1667 K (1394 °C) for pure Fe).

A multicomponent phase field model for directional solidification was constructed using MICRESS[®] [26]. Two compositions were selected; one representing the TRIP steel under investigation and other with the same composition as the TRIP steel, but without P, referred to as TRIP-0P. Simulations were carried out with a grid size of 150 μm x 250 μm and 2 μm grid resolution. The phase field code was coupled with the thermodynamic software

Thermo-Calc^{TM} to obtain equilibrium thermodynamic data. The mobility information was directly obtained from the MOB2 database of Thermo-Calc^{TM}. Four nuclei of δ ferrite were placed at the bottom of the simulation domain with an undercooling of 5 K at the underside. A cooling rate of $10\,\mathrm{K\,s^{-1}}$ and a thermal gradient of $200\,\mathrm{K\,mm^{-1}}$ in the vertical direction was applied in the model, the latter based on the average solidification rate of the dendrites from the underside to the top. Energy parameters applied in the phase field model can be found in reference [27]. To calculate the stress evolution in the solid that develops due to solidification shrinkage and thermal contraction, a fixed mechanical boundary condition (Figure 6.5 (a)) was applied to the simulation domain. For both the steels, a constant elastic modulus of 10 GPa for the solid at high temperature [28] and 1 GPa for the liquid [29, 30] was assumed. A constant thermal expansion coefficient of $2.5 \times 10^{-5}\,\mathrm{K^{-1}}$ and $3 \times 10^{-5}\,\mathrm{K^{-1}}$ was used for the solid and the liquid phases, respectively.

6.3 Results and discussion

Figure 6.2 (a) indicates the diameter of the melt pool. Figure 6.2 (b)-(f) shows the solidification sequence of the TRIP steel. A stable melt pool with a diameter of approximately 3 mm was created before the cooling cycle started, as shown in Figure 6.2 (b). The solidification front was initially observed to be planar. However, a temperature gradient in the thickness direction of the sample led to the nucleation of dendrites from the underside of the specimen as can be seen in Figure 6.2 (c). During the last stages of solidification, solidification cracking was observed *in-situ* as shown in Figure 6.2 (d). Concurrently, isolated liquid pockets could be identified at a temperature of 1615 ± 8 K (1342 ± 8 °C) (Figure 6.2 (d-e)). A crack can be observed clearly in Figure 6.2 (f) and the final extent of solidification cracking is shown in the secondary electron micrograph (Figure 6.2 (a)).

To obtain the solute content in the last solidified liquid, three site-specific samples (S1, S2 and S3) for atom probe tomography (APT) were prepared from the interdendritic region near the crack surface (Figure 6.3 (a)) using a focused ion beam and the local elemental distribution adjacent to the crack was investigated. Figure 6.3 (b) shows the C and P maps from one of the samples. The composition of the three interdendritic APT samples along with the nominal composition is shown in Table 6.1. Notable enrichment of C and P was found in all three APT samples. In addition, slight enrichment in Si was also found. Silicon enrichment in the liquid can lead to the formation of a low melting point eutectic Fe-Fe$_2$Si (melting point = 1485 K (1212 °C)) [31], thereby increasing the susceptibility to solidification cracking. Silicon contents above 0.65 wt. % may increase the cracking tendency in ferritic steels [32]. A secondary electron micrograph (Figure 6.3 (c)) of the polished sample from the same region where the APT samples were prepared, indicates the intergranular nature of solidification crack.

Figure 6.4 (a) shows the cellular morphology of delta (δ) ferrite in the TRIP steel, growing upward from the bottom of the domain. Carbon and phosphorus maps are shown in Figures 6.4 (b) and (c), respectively. Due to microsegregation of C and P in the interdendritic region, the liquid in this region is undercooled. Figure 6.4 (e) shows the temperature versus solid fraction (f_s) curves calculated from the equilibrium conditions and phase field simulations for the two steels. Experimental observation of isolated liquid pockets (Figure 6.2 (d-e)) at a temperature 1615 ± 8 K ($\approx$ 160 K undercooling) is found to be in agreement with phase field simulations (Figure 6.4 (e)). The temperature
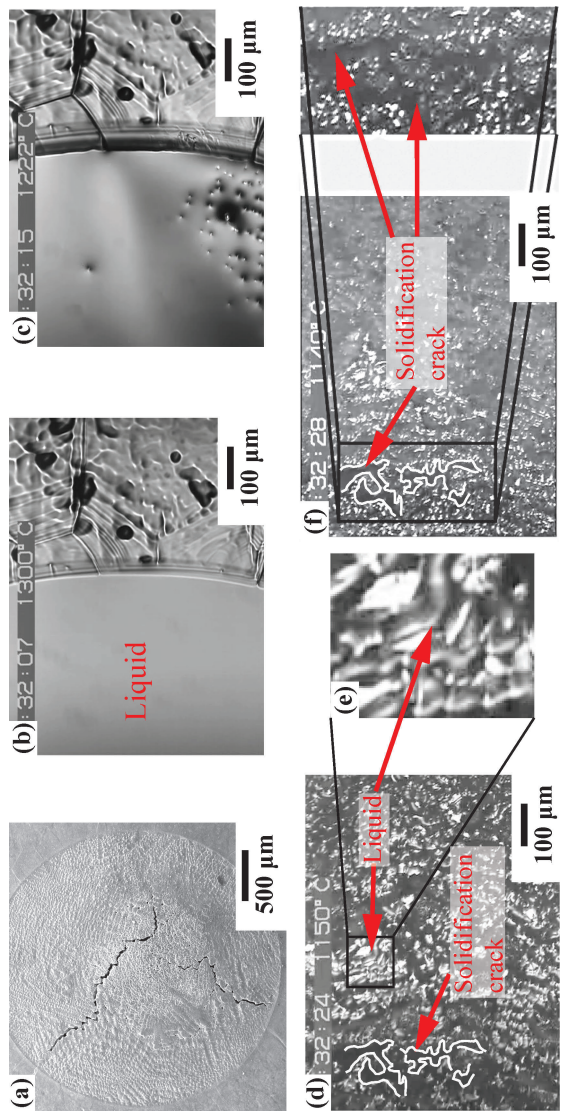
Figure 6.2: (a) Secondary electron micrograph showing the extent of solidification cracking, (b–f) solidification images from the confocal microscope, (b) a stable circular melt pool of diameter ≈ 3 mm at the center of the specimen while the outer rim remains solid, (c) dendrites growing mostly from the bottom of the pool owing to a thermal gradient in the thickness direction, (d–e) solidification crack and isolated liquid pockets and (f) distinct solidification crack observed *in-situ* at the last stage of solidification. Temperature indicated in images (b–d) and (f) is measured at the periphery of the platinum specimen holder. Based on calibration the actual temperature is ∼ 212 K higher.
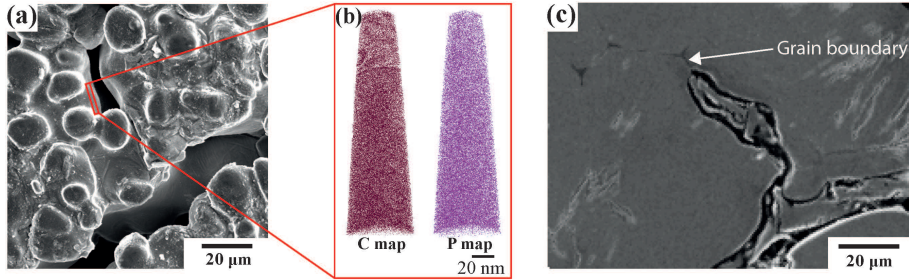
Figure 6.3: (a) Secondary electron micrograph indicating the region from which the samples were prepared for atom probe tomography using a focused ion beam, (b) C and P map obtained by APT and (c) secondary electron micrograph (from the same region where the APT samples were prepared) indicating intergranular solidification cracking.

6

corresponds to $f_s \approx 0.99$ from the phase field simulations. Due to fast solidification and limited spatial resolution, coexistence of liquid and crack prior to the image as shown in Figure 6.2 (d-e), could not be verified. However, since the maximum crack width is approximately 50 μm in Figure 6.2 (d), it can be argued that the crack must have initiated at a lower f_s. This observation is consistent with earlier studies by Rappaz *et al.* [15] and by Kou [33] in which extensive solid bridging was assumed to occur at $f_s = 0.98$ after which there is minimal susceptibility to solidification cracking.

Table 6.1: Bulk composition in the interdenritic region of the top surface. Nominal composition is also listed.

Element (*wt.* %)	Nominal composition	Sample S1	S2	S3	Average
C	0.19	0.48	0.87	0.69	0.68
P	0.089	0.32	0.22	0.32	0.29
Mn	1.63	1.44	1.50	1.62	1.52
Al	1.1	0.94	0.94	1.04	0.97
Si	0.35	0.55	0.51	0.66	0.57

Figure 6.4 (d) shows the cellular morphology of δ ferrite for the TRIP-0P steel. In comparison with the TRIP steel, the solidification rate was found to be faster in the TRIP-0P steel. For the sake of the ensuing discussion, the same liquid fraction ($f_L = 0.13$) is shown in both cases, where the temperature of the TRIP steel is 10 K lower than that of the TRIP-0P steel. Any opening at the interdendritic boundary due to tensile stress needs to be compensated by liquid feeding. Liquid flow in a porous medium is related to the pressure gradient as described by Darcy's law [34, 35],

$$v_l f_L = -\frac{K}{\eta} \left[\frac{\Delta P}{Z} + \rho g_z \right],$$ (6.1)

where v_l is the interdendritic velocity of the liquid, f_L is the fraction of liquid, K is
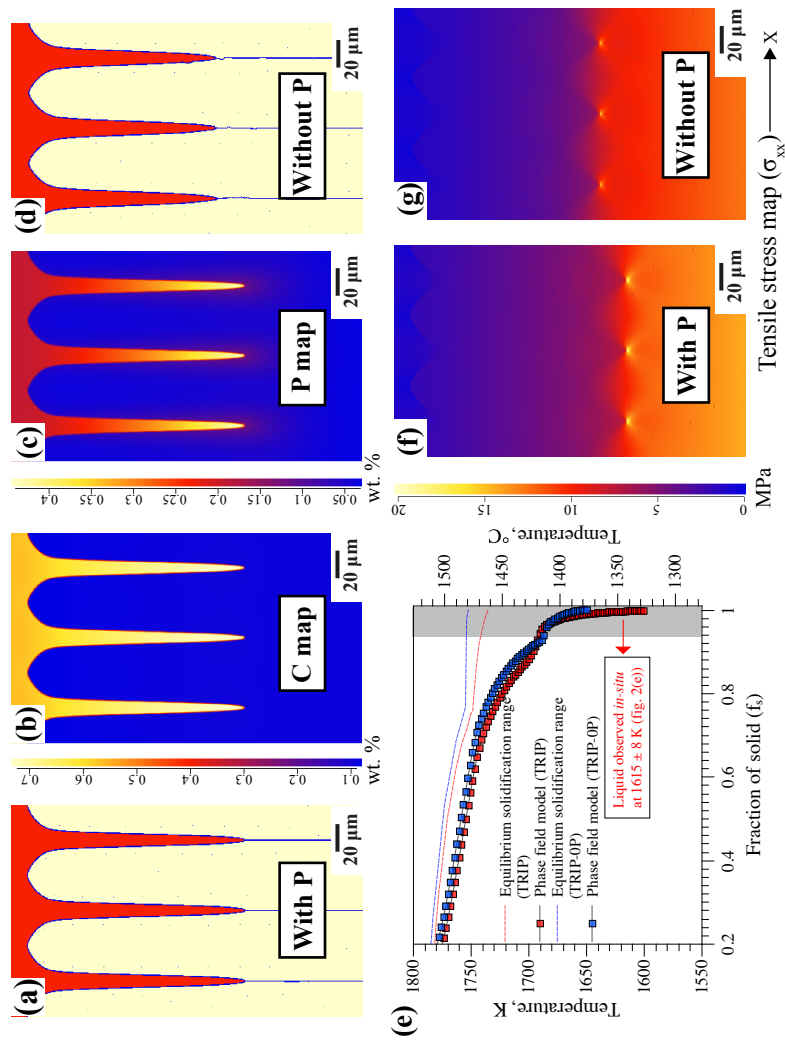
Figure 6.4: Phase field simulation showing liquid channel morphology and microsegregation (a) TRIP steel composition, (b) Carbon map in TRIP steel, (c) Phosphorus map in TRIP steel, (d) phase field simulation showing liquid channel morphology for TRIP-0P steel composition, (e) T $vs.$ f_s curves for the two steels from equilibrium phase diagram and phase field simulations, (f) and (g) tensile stress map in TRIP and TRIP-0P steel respectively.
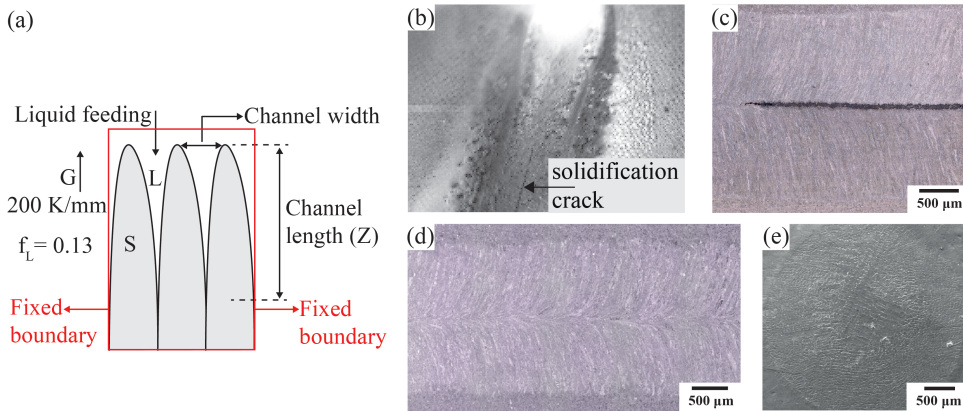
Figure 6.5: (a) Schematic illustrating the solidifying morphology and boundary conditions. Please refer to Figure 6.2 (c), (b) high-speed camera image taken during welding of TRIP steel showing solidification cracking, (c) optical macrograph of the weld surface of TRIP steel, (d) optical macrograph of the weld surface of the DP steel with 0.01 wt.% P and (e) secondary electron image of DP steel with 0.01 wt. % P after melt pool solidification.

the permeability in the mushy zone, η is the viscosity of the liquid, ΔP is the pressure difference between the tip and root of the dendrite and Z is the length of the liquid channel. The prevailing conditions are described in the schematic Figure 6.5 (a). In comparison, longer and narrower liquid channels exist in the TRIP steel (Figure 6.4 (a)) than in the TRIP-0P steel (Figure 6.4 (d)). Considering Darcy's law (6.1), a higher feeding rate v_l, is required in the TRIP steel in order to avoid cracking for a similar pressure difference. In addition, the effect of η should also be considered. Viscosity is an important parameter that leads to the kinetic slowdown of a melt being undercooled due to solute enrichment [36]. The generalized form of the viscosity of a liquid alloy as a function of temperature follows an Arrhenius curve [37]. Therefore, η in the interdendritic region increases as the extent of undercooling increases, further increasing the barrier for adequate liquid feeding. Note that liquid flow was not considered in the present phase field model and therefore only relative liquid feeding capability is discussed.

Figures 6.4 (f) and (g) shows the map of tensile stress (σ_{xx}) in TRIP and TRIP-0P steel, respectively. Due to the solidification morphology (longer dendrite arms) and the greater thermal contraction at the root of the dendrites, associated with the 10 K lower temperature, the TRIP steel exhibits a higher tensile stress ($\approx 19\,\mathrm{MPa}$) concentration at the dendritic boundaries close to the root compared to $\approx 15\,\mathrm{MPa}$ for the TRIP-0P steel. There is negligible stress in the arms of the dendrites due to the presence of liquid in between, *i.e.* coalescence has not occurred. The higher magnitude of tensile stress in TRIP steel increases the susceptibility to form a solidification crack. Next, the factors that lead to an opening near the root of the dendrites are considered. The opening occurs in the form of micro-voids due to thermally induced stress [13]. These voids are generally nucleated at grain boundaries since these provide an existing surface and thereby contribute to the driving force. Phosphorus segregation at the grain boundaries is known to promote decohesion [38–40]. The average phosphorus concentration in TRIP steel from the three samples taken near the crack was measured to be 0.29 wt. %, *i.e.* more than three times

the nominal composition. When compared to TRIP-0P, a lower critical stress at the grain boundary in TRIP steel will lead to an opening at the grain boundary.

Two associated phenomena related to P increase the solidification cracking susceptibility. Firstly, microsegregation of P leads to severe undercooling in the interdendritic region making the liquid channels longer and narrower. Secondly, phosphorus segregation at the grain boundary promotes decohesion, *i.e.* a solidification crack can nucleate at a lower thermally induced critical tensile stress. An opening thus formed is relatively difficult to fill with the remaining liquid due to low permeability and high viscosity, eventually leading to cracking.

In order to test the premise of confocal microscopy results on weld solidification cracking, autogenous or melt-run welding experiments were conducted under identical conditions using a Nd:YAG laser. TRIP steel sheets and steel sheets with low P (0.01 wt. %), *i.e.* DP steel, were selected. Figure 6.5 (b) shows a high-speed camera image taken during welding of the TRIP steel. A solidification crack was observed to follow the trailing edge of the weld pool. Figure 6.5 (c) shows the macrostructure of the weld surface indicating the centreline crack. In DP steel with 0.01 wt. % P, solidification cracking was not observed in either the laser welding (Figure 6.5 (d)) or the confocal microscopy experiments (Figure 6.5 (e)). Consistent results from the two experimental methods thus show that the TRIP steel with 0.089 wt. % P is prone to cracking during solidification under welding conditions. It is thus emphasized that a sufficiently low amount of P is needed to achieve good weldability, without compromising its role in the TRIP effect.

6.4 Summary

In summary, solidification of a TRIP steel with 0.089 wt. % P was studied and solidification cracking was observed in the final stages of solidification. Microsegregation of P leads to undercooling resulting in longer and narrower liquid channels that persist in the crack vulnerable region. In addition, P segregation renders the grain boundaries weak. As a result, tensile strain/stress are concentrated at the interdendritic boundaries leading to increased susceptibility to cracking. Conversely, lack of P in the TRIP steel leads to shorter and wider liquid channels that can be fed relatively easily in the event of an opening at the root of the solidifying dendrites. In DP steel with a small amount of P (0.01 wt. %), no solidification cracking was observed.

References

[1] T. Senuma, *Physical metallurgy of modern high strength steel sheets,* ISIJ International **41**, 520 (2001).

[2] O. Matsumura, Y. Sakuma and H. Takechi, *Enhancement of elongation by retained austenite in intercritical annealed 0.4C-1.5Si-0.8Mn steel,* Transactions of the Iron and Steel Institute of Japan **27**, 570 (1987).

[3] O. Matsumura, Y. Sakuma and H. Takechi, *Trip and its kinetic aspects in austempered 0.4C-1.5Si-0.8Mn steel,* Scripta Metallurgica **21**, 1301 (1987).

[4] J. Mahieu, J. Maki, B. De Cooman and S. Claessens, *Phase transformation and mechanical properties of Si-free CMnAl transformation-induced plasticity-aided steel,* Metallurgical and Materials Transactions A **33**, 2573 (2002).

[5] E. Jimenez-Melero, N. van Dijk, L. Zhao, J. Sietsma, S. Offerman, J. Wright and S. van der Zwaag, *The effect of aluminium and phosphorus on the stability of individual austenite grains in trip steels,* Acta Materialia **57**, 533 (2009).

[6] H. C. Chen, H. Era and M. Shimizu, *Effect of phosphorus on the formation of retained austenite and mechanical properties in Si-containing low-carbon steel sheet,* Metallurgical Transactions A **20**, 437 (1989).

[7] B. D. Cooman, *Structure–properties relationship in trip steels containing carbide-free bainite,* Current Opinion in Solid State and Materials Science **8**, 285 (2004).

[8] H. K. D. H. Bhadeshia and D.-W. Suh, *Is low phosphorus content in steel a product requirement?* Ironmaking & Steelmaking **42**, 259 (2015).

[9] J. Wang and S. v. d. Zwaag, *Theoretical study of P-containing transformation-induced plasticity steel part 1 determination of the phosphorus concentration,* Zeitschrift für Metallkunde **92**, 1299 (2001).

[10] J. Lippold, *Welding Metallurgy and Weldability*, 1st ed. (John Wiley & Sons, 2014) pp. 84–119.

[11] W. Mirihanage, M. D. Michiel, A. Reiten, L. Arnberg, H. Dong and R. Mathiesen, *Time-resolved x-ray diffraction studies of solidification microstructure evolution in welding,* Acta Materialia **68**, 159 (2014).

[12] M. Rappaz and J. Dantzig, *Solidification*, 1st ed. (EFPL Press, 2009) pp. 519–563.

[13] L. Aucott, D. Huang, H. Dong, S. Wen, J. Marsden, A. Rack and A. Cocks, *Initiation and growth kinetics of solidification cracking during welding of steel,* Scientific Reports **7: 40255** (2017).

[14] S. Kou, *A criterion for cracking during solidification,* Acta Materialia **88**, 366 (2015).

[15] M. Rappaz, J. M. Drezet and M. Gremaud, *A new hot-tearing criterion,* Metallurgical and Materials Transactions A **30**, 449 (1999).

6

[16] W. S. Pellini, *Strain theory of hot-tearing,* Foundry **80**, 124 (1952).

[17] N. N. Prokhorov, *The problem of the strength of metals while solidifying during welding,* Svar Proiz **6**, 5 (1956).

[18] I. Medovar, *On the nature of weld hot cracking,* Avtomatich. Svarka **7**, 12 (1954).

[19] U. Feurer, *Influence of alloy composition and solidification conditions on dendrite arm spacing, feeding, and hot tear properties of aluminum alloys,* in *Proceedings of the International Symposium on Engineering Alloys, Delft* (1977) pp. 131–145.

[20] T. Kannengießer and T. Böllinghaus, *Hot cracking tests - an overview of present technologies and applications,* Welding in the World **58**, 397 (2014).

[21] S. Griesser, C. Bernhard and R. Dippenaar, *Effect of nucleation undercooling on the kinetics and mechanism of the peritectic phase transition in steel,* Acta Materialia **81,** 111 (2014).

[22] H. Shibata, Y. Arai, M. Suzuki and T. Emi, *Kinetics of peritectic reaction and transformation in Fe-C alloys,* Metallurgical and Materials Transactions B **31**, 981 (2000).

[23] M. Reid, D. Phelan and R. Dippenaar, *Concentric solidification for high temperature laser scanning confocal microscopy,* ISIJ International **44**, 565 (2004).

[24] Y.-S. Chen, D. Haley, S. S. A. Gerstl, A. J. London, F. Sweeney, R. A. Wepf, W. M. Rainforth, P. A. J. Bagot and M. P. Moody, *Direct observation of individual hydrogen atoms at trapping sites in a ferritic steel,* Science **355,** 1196 (2017).

[25] S. Griesser and R. Dippenaar, *Enhanced concentric solidification technique for high-temperature laser-scanning confocal microscopy,* ISIJ International **54**, 533 (2014).

[26] I. Steinbach and F. Pezzolla, *A generalized field method for multiphase transformations using interface fields,* Physica D **134**, 385 (1999).

[27] M. Amirthalingam, E. M. van der Aa, C. Kwakernaak, M. J. M. Hermans and I. M. Richardson, *Elemental segregation during resistance spot welding of boron containing advanced high strength steels,* Welding in the World **59**, 743 (2015).

[28] W.-Y. Wang, B. Liu and V. Kodur, *Effect of temperature on strength and elastic modulus of high-strength steel,* Journal of Materials in Civil Engineering **25**, 174 (2013).

[29] N. Coniglio and C. Cross, *Mechanisms for solidification crack initiation and growth in aluminum welding,* Metallurgical and Materials Transactions A **40**, 2718 (2009).

[30] C. Bordreuil and A. Niel, *Modelling of hot cracking in welding with a cellular automaton combined with an intergranular fluid flow model,* Computational Materials Science **82,** 442 (2014).

[31] V. Shankar, T. P. S. Gill, S. L. Mannan and S. Sundaresan, *Solidification cracking in austenitic stainless steel welds,* Sadhana **28,** 359 (2003).

6

[32] N. Bailey, *Weldability of Ferritic Steels*, 1st ed. (1st ed., Woodhead Publishing, 1994) pp. 69–70.

[33] S. Kou, *A simple index for predicting the susceptibility to solidification cracking,* Welding Journal **94**, 374s (2015).

[34] K. Kubo and R. D. Pehlke, *Mathematical modeling of porosity formation in solidification,* Metallurgical Transactions B **16**, 359 (1985).

[35] D. R. Poirier, *Permeability for flow of interdendritic liquid in columnar-dendritic alloys,* Metallurgical Transactions B **18**, 245 (1987).

[36] Z. Evenson, S. Raedersdorf, I. Gallino and R. Busch, *Equilibrium viscosity of Zr-Cu-Ni-Al-Nb bulk metallic glasses,* Scripta Materialia **63**, 573 (2010).

[37] R. N. Singh and F. Sommer, *Viscosity of liquid alloys: generalization of andrade's equation,* Monatshefte für Chemie - Chemical Monthly **143**, 1235 (2012).

[38] R. Wu, A. J. Freeman and G. B. Olson, *First principles determination of the effects of phosphorus and boron on iron grain boundary cohesion,* Science **265**, 376 (1994).

[39] F. Christien, R. L. Gall and G. Saindrenan, *Phosphorus grain boundary segregation in steel 17-4PH,* Scripta Materialia **48**, 11 (2003).

[40] C. Naudin, J. Frund and A. Pineau, *Intergranular fracture stress and phosphorus grain boundary segregation of a Mn-Ni-Mo steel,* Scripta Materialia **40**, 1013 (1999).

6

7

Liquid feeding during solidification of DP steel[¶¶]

In the previous chapter, it was shown that adequate liquid feeding is an important aspect which affects solidification cracking susceptibility. In this chapter, the results of unique *in-situ* experimental observations of liquid feeding in the solidifying melt pool of DP steel, are presented.

7.1 Introduction

As mentioned in chapter 6, liquid feeding is one of the most important aspects that helps to avoid solidification cracking and likewise is included in most of the models [1–3]. Feurer [2] proposed that cracking occurs, if the rate of feeding of the liquid in the inter-dendritic region is less than the rate of shrinkage of the solid being formed. The model proposed by Rappaz *et al.* [3] considered liquid feeding due to both shrinkage and deformation of the coherent dendritic network. If the liquid feeding in the inter-dendritic region of the mushy zone is insufficient to compensate for the shrinkage and cumulative deformation of the mushy zone, the pressure drops below a certain cavitation pressure (refer to Figure 2.23) and voids form, grow and eventually coalesce to form a crack. Recently, Kou [1] proposed a model focussing on similar events occurring at grain boundary level.

Observing the solidification process in the mushy zone under welding conditions is difficult. In the past decade, high energy X-rays sources have facilitated the *in-situ* study of solidification behaviour in many metallic materials [4–7]. These studies were mostly focussed on Al-Cu, Sn-Pb, Al-Ni and other such systems with relatively low liquidus temperatures [8]. Studies in Fe-C systems are in general focussed on solid state phase transformations. Nagira *et al.* [8] observed *in-situ* deformation in a semi-solid carbon steel. They studied the deformation mechanism under direct shear of the steel with a globular morphology and solid fraction between 55 and 65 %. Several other techniques

---

like directional solidification (Bridgman technique [9]), high speed camera observations of the weld pool solidification [10] *etc.* were also frequently used to study solidification phenomena. None of the studies, however, have reported direct observation of liquid flow during the terminal stages of solidification.

In this study, solidification of a dual phase steel was observed *in-situ* using high temperature laser scanning confocal microscopy. A circular melt pool was formed at the centre of a thin circular disk specimen, while the outer rim remained solid. During the terminal stages of solidification, liquid feeding was observed in inter-cellular regions. The feeding rate in these regions is calculated and subsequently the pressure that causes liquid feeding is estimated.

7.2 Experimental procedure

A commercial dual phase steel sheet with a composition, C 0.15, Mn 2.3, Cr 0.56, Si 0.1, Al 0.03, P 0.01 (all in wt. %) was examined in this study. Circular disk specimens with a diameter of 10 mm and a thickness between 200 μm - 250 μm were prepared using electro-discharge machining. The experimental arrangement, as described in chapter 6 was utilised in this study. A stable melt pool with a diameter between 3-3.5 mm was obtained at the centre of the specimen while the outer rim remained solid. A cooling rate of $5\,\mathrm{K\,min^{-1}}$ was employed until 1623 K, which is below the equilibrium solidus temperature of the investigated steel composition.

7.3 Results and discussion

Figure 7.1 shows the solidification sequence of the steel. A stable melt pool of diameter 3.1 mm was created before the cooling cycle started, as seen in Figure 7.1 (a). Due to the slow cooling rate, the solidification front was initially observed to remain planar (Figure 7.1 (b)). On further cooling, the interface morphology changed from planar to cellular growth as seen in Figure 7.1 (c). On a macro scale, the solid-liquid interface was observed to propagate in a concentric manner throughout the solidification process. Concentric propagation of the interface was tracked using automatic video processing software for *in-situ* interface tracking [11]. The radius of curvature of the interface can be used to calculate the fraction of solid and liquid at any time. Figure 7.1 (d) shows the terminal stage of the solidification during which the liquid feeding was observed in the inter-cellular regions. The fraction of liquid remaining was ≈ 1.2 % when compared to the original melt pool size. Two regions where liquid feeding was observed are marked in Figure 7.1 (d) and further shown in Figure 7.3 and Figure 7.4 respectively. The liquid source for the feeding is the liquid remaining during the final stage of solidification in the centre. The process was dynamic and occurred in a matter of a few seconds. For better visualisation of the liquid flow, the reader is referred to the embedded video available in the PDF version of this dissertation, referred to as Figure 7.2. Figure 7.3 shows the images from region 1 with F-*n* indicating the frame numbers. Time difference between successive frames is 33.33 ms. In order to determine the extent of liquid flow, the reference gray scale image, Figure 7.3 (a), was subtracted from subsequent images and resulting bitmap images show the extent of the liquid flow in the intervening time period. The pixels with no difference were then assigned a grey colour and the pixels where motion was detected
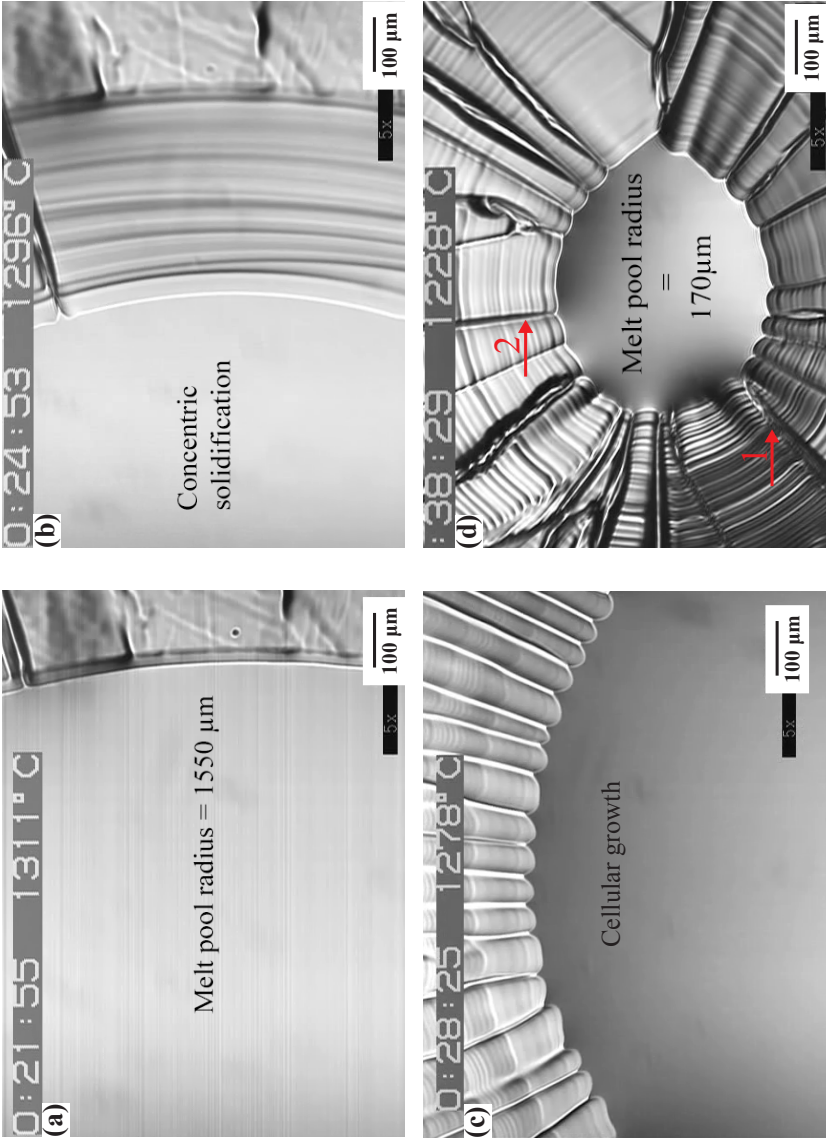
Figure 7.1: Solidification images. (a) A stable melt pool of radius 1550μm is formed to begin with. Afterwards a constant cooling rate of 5 K min^{-1} is applied, (b) solidification progresses in a concentric manner, (c) planar growth changes to cellular growth and (d) melt pool of radius 170μm when liquid feeding in the inter-cellular regions was observed. Temperature indicated in images (a-d) is measured at the periphery of the platinum holder. Based on calibration the actual temperature is ~ 212 K higher.

were assigned a red colour; the results are shown in Figure 7.3 (e)-(g).

Figure 7.2: Liquid feeding observed in the intergranular regions marked with arrows. The frame rate is of 60 frames per second.

Figure 7.3: Solidification images. Liquid flow observed in the inter-cellular region 1 as defined in Figure 7.1 (d). (a) is taken as the reference image, (b) liquid flow was observed, (c) and (d) liquid flow continues and reaches the bottom of the image when compared to the reference image, (e), (f) and (g) shows the extent of the liquid flow in images (b), (c) and (d) when compared to reference image (a). This was done using a MATLAB code to detect motion in a series of otherwise still images.
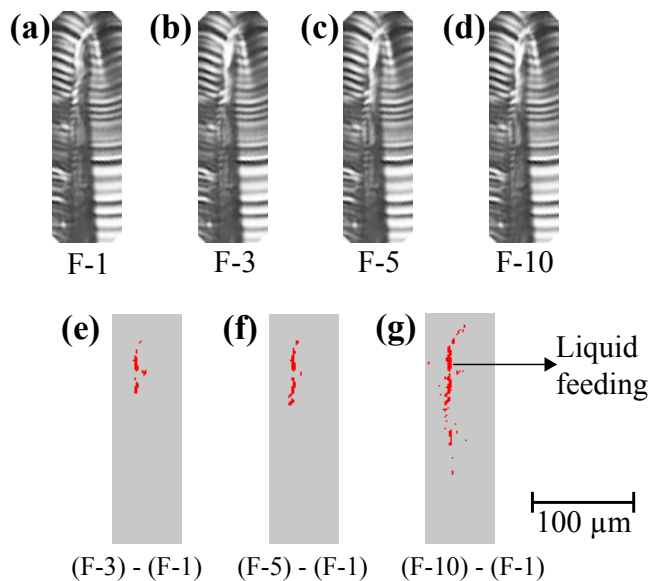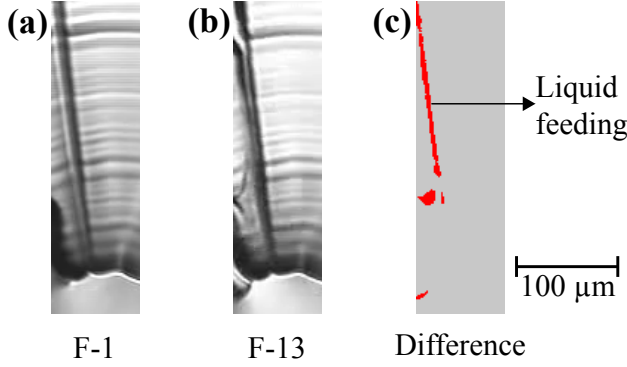
Figure 7.4: Solidification images. Liquid flow observed in the inter-cellular region 2 as defined in Figure 7.1 (d). (a) is taken as the reference image , (b) liquid flow observed and (c) shows the extent of liquid feeding.
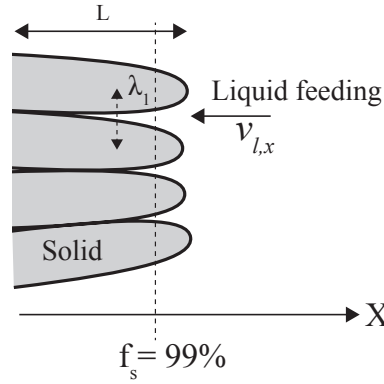
Figure 7.5: Schematic illustration of the liquid feeding observed in the experiments. Rate of feeding criterion applied for cellular growth.

A similar procedure was followed for the region 2 and the results can be seen in Figure 7.4. In chapter 6, the results of high temperature confocal microscopy experiments on TRIP steels were described and liquid feeding was not observed during solidification. Instead, solidification cracking was observed *in-situ* during the final stages of solidification.

Feurer [2] defined the maximum volumetric flow rate per unit volume (rate of liquid feeding, ROF) during solidification as:

$$ROF = \frac{\partial V}{V} \cdot \frac{1}{\partial t} = \frac{\partial \ln V}{\partial t} = \frac{f_l^2 d^2 P_s}{24\pi c^3 \mu L^2}, \tag{7.1}$$

where, f_l is the fraction of liquid, d is the secondary dendrite arm spacing, P_s is the effective feeding pressure, c is the tortuosity factor of the dendritic network, μ is the viscosity of the liquid phase and L is the length of the mushy zone. However, this equation is valid only in the case of dendritic solidification. In the current work, cellular growth was observed and the rate of liquid feeding applicable in this situation can be defined with

the help of schematic presentation in Figure 7.5. The solidification direction is assumed to be parallel to the "x" direction (Cartesian coordinate system) and the liquid flows in the $-x$ direction. The rate of liquid feeding (ROF) can be defined as:

$$ROF = \frac{\partial V}{V} \cdot \frac{1}{\partial t} = \frac{v_{l,x}}{A} \cdot \frac{A}{L} = \frac{v_{l,x}}{L}, \tag{7.2}$$

where, $v_{l,x}$ is the unidirectional flow speed of liquid in the $-x$ direction, A is the cross-sectional area perpendicular to the growth direction and L is the length of the mushy zone. Due to a low solidification rate ($0.75\,\mu m\,s^{-1}$), the cross-sectional area A is assumed to remain constant during the time period in which liquid flow was observed ($\Delta t = 0.3 - 0.4$ s).

The rate of solidification shrinkage (ROS) is given by:

$$ROS = \frac{\partial V}{V} \cdot \frac{1}{\partial t} = -\frac{1}{\rho} \cdot \frac{\partial \rho}{\partial t} = \frac{\beta}{\beta.f_s + 1} \cdot \frac{\mathrm{d}f_s}{\mathrm{d}t}, \tag{7.3a}$$

with

$$\beta = \frac{\rho_\gamma - \rho_l}{\rho_l}, \tag{7.3b}$$

where, f_s, f_l are the fractions of the solid and liquid, ρ_γ, ρ_l the densities of the austenite and liquid phases, respectively. The rate of change of f_s can be calculated by determining f_s at various times during the course of solidification. The shrinkage factor of the steel was calculated as 3.8% using the commercial thermodynamic software Thermo-Calc$^{\mathrm{TM}}$. The rate of solidification shrinkage is found to be $\approx 4.2 \times 10^{-6}\,s^{-1}$ during the period where liquid feeding was observed.

The rate of deformation (ROD) of the mushy region can be approximated as [12]:

$$ROD = -\alpha.\dot{T}, \tag{7.4}$$

where, α is the linear thermal expansion coefficient when $f_s \approx 99\,\%$ and $\dot{T}$ is the cooling rate. Assuming $\alpha = 1.2 \times 10^{-5}\,K^{-1}$ [13], the rate of deformation is $\approx 1 \times 10^{-6}\,s^{-1}$. In the current case, the rate of solidification shrinkage and the rate of deformation are found to be of the same order. To avoid the formation of voids which can later lead to solidification cracking, the rate of liquid feeding should be higher than both the rate of solidification shrinkage and the rate of deformation combined.

The average velocity of the liquid ($v_{l,x}$) in the inter-cellular channel was calculated by image analysis and was found to be $450\,\mu m\,s^{-1}$ and $500\,\mu m\,s^{-1}$ in regions 1 and 2, respectively. Such high velocities can exist due to a pressure drop in the cavities between the cells. The length of the mushy zone was $250\,\mu m$. The rate of liquid feeding calculated from equation (7.2) is six orders of magnitude higher than the rate of solidification shrinkage and the rate of deformation combined. As a result, no solidification cracking is expected and indeed no crack was observed during solidification. The velocity of the liquid in the mushy zone is related to the pressure gradient in the liquid via the Darcy's equation [3, 14],

$$v_{l,x}f_l = -\frac{K}{\mu} \frac{\Delta P}{L}, \tag{7.5}$$

where $v_{l,x}$ is the velocity of the liquid, f_l is the fraction of liquid, K is the permeability in the mushy zone and μ is the viscosity of the liquid. The contribution of gravity has been neglected in this equation. Permeability data is scarce for $f_l \leq 0.17$. For extrapolations, Poirier recommended the use of models based on Blake-Kozeny equations [15]. The permeability defined by the Blake-Kozeny relationship [15] is given by,

$$K = C_2 \frac{\lambda_1^2 f_l^3}{(1-f_l)}, \tag{7.6a}$$

with

$$C_2 = 4.53 \times 10^{-4} + 4.02 \times 10^{-6}(f_l + 0.1)^{-5}, \tag{7.6b}$$

where, λ_1 is the inter-cellular spacing and f_l is the fraction of liquid. C_2 was obtained by regression analysis. The average spacing was $45 \pm 10 \mu m$. Using the fraction of liquid (f_l) = 0.01, the value of permeability in the mushy region was calculated as $6.3 \times 10^{-16} m^2$. The value is reasonable since for a Pb - 20 wt. % Sn alloy with primary dendrite arm spacing 51 μm and higher liquid fration (f_l = 0.19), Streat *et al.* [16] reported higher permeability values of the order of $10^{-14} m^2$.

Considering the fluid behaviour to be Newtonian, the dynamic viscosity (μ) was assumed to be constant as 4.9 mPa s [17]. Moreover, the temperature change during which the flow occurred was found to be negligible (cooling rate ≈ 0.083 K s^{-1}). The pressure difference was then calculated from Darcy's equation (7.5) and an average pressure difference (in regions 1 and 2) of the order of 10^4 Pa is found. To the best knowledge, this is the first time that an experimentally derived feeding pressure has been reported. No solidification cracking occurred during solidification of the steel in the present case, therefore the cavitation pressure for this steel must exceed 10^4 Pa. In the cases where there is insufficient liquid feeding due to a combination of high viscosity and/or low permeability, the drop in the pressure can become equal to the cavitation pressure resulting in the formation of a cavity.

7.4 Summary

In summary, solidification of a dual phase steel was observed *in-situ* under a high temperature laser scanning confocal microscope. Liquid feeding occurred during the terminal stage of solidification in the inter-cellular regions. Liquid flow speed in the inter-cellular regions was derived and the pressure difference that causes liquid flow was estimated by means of Darcy's equation. It was also found that rate of liquid feeding was higher than the rate of solidification shrinkage and rate of deformation combined.

References

[1] S. Kou, *A criterion for cracking during solidification,* Acta Materialia **88**, 366 (2015).

[2] U. Feurer, *Influence of alloy composition and solidification conditions on dendrite arm spacing, feeding, and hot tear properties of aluminum alloys,* in *Proceedings of the International Symposium on Engineering Alloys, Delft* (1977) pp. 131–145.

[3] M. Rappaz, J. M. Drezet and M. Gremaud, *A new hot-tearing criterion,* Metallurgical and Materials Transactions A **30**, 449 (1999).

[4] H. Yasuda, I. Ohnaka, K. Kawasaki, A. Sugiyama, T. Ohmichi, J. Iwane and K. Umetani, *Direct observation of stray crystal formation in unidirectional solidification of Sn–Bi alloy by X-ray imaging,* Journal of Crystal Growth **262**, 645 (2004).

[5] N. Iqbal, N. van Dijk, S. Offerman, M. Moret, L. Katgerman and G. Kearley, *Real-time observation of grain nucleation and growth during solidification of aluminium alloys,* Acta Materialia **53**, 2875 (2005).

[6] P. Schaffer, R. Mathiesen and L. Arnberg, L_2 *droplet interaction with* α-*Al during solidification of hypermonotectic Al–8 wt. % Bi alloys,* Acta Materialia **57**, 2887 (2009).

[7] R. Mathiesen, L. Arnberg, F. Mo, T. Weitkamp and A. Snigirev, *Time resolved x-ray imaging of dendritic growth in binary alloys,* Physical Review Letters **83**, 5062 (1999).

[8] T. Nagira, C. Gourlay, A. Sugiyama, M. Uesugi, Y. Kanzawa, M. Yoshiya, K. Uesugi, K. Umetani and H. Yasuda, *Direct observation of deformation in semi-solid carbon steel,* Scripta Materialia **64**, 1129 (2011).

[9] M. Vandyoussefi, H. Kerr and W. Kurz, *Two-phase growth in peritectic Fe-Ni alloys,* Acta Materialia **48**, 2297 (2000).

[10] P. von Witzendorff, S. Kaierle, O. Suttmann and L. Overmeyer, *In situ observation of solidification conditions in pulsed laser welding of AL6082 aluminum alloys to evaluate their impact on hot cracking susceptibility,* Metallurgical and Materials Transactions A **46**, 1678 (2015).

[11] S. Griesser, R. Pierer, M. Reid and R. Dippenaar, *Soltrack: An automatic video processing software for in situ interface tracking,* Journal of Microscopy **248**, 42 (2012).

[12] M. Drezet, M.-F. Lima, J. Wagniere, M. Rappaz and W. Kurz, *Crack-free aluminium alloy welds using a twin laser process,* in *Proceedings of the International Institute of Welding Conference,* edited by P. Mayr, G. Posch and H. Cerjak (2008) pp. 87–94.

[13] X. Li, L. Wang, L. Yang, J. Wang and K. Li, *Modeling of temperature field and pool formation during linear laser welding of DP1000 steel,* Journal of Materials Processing Technology **214**, 1844 (2014).

[14] K. Kubo and R. D. Pehlke, *Mathematical modeling of porosity formation in solidification,* Metallurgical Transactions B **16**, 359 (1985).

[15] D. R. Poirier, *Permeability for flow of interdendritic liquid in columnar-dendritic alloys,* Metallurgical Transactions B **18**, 245 (1987).

[16] N. Streat and F. Weinberg, *Interdendritic fluid flow in a lead-tin alloy,* Metallurgical Transactions B **7**, 417 (1976).

[17] J. H. Hildebrand and R. H. Lamoreaux, *Viscosity of liquid metals: An interpretation,* Proceedings of the National Academy of Sciences of the United States of America **73**, 988 (1976).|

8

General discussion[***][†††]

IN chapters 5 and 6, it was shown that TRIP steel is susceptible to cracking during solidification. In chapter 5, solidification cracking in TRIP steel was attributed to the presence of a threshold transverse strain close to the fusion boundary. In all the welding and *in-situ* solidification experiments, no solidification cracking was observed in DP steel. A higher resistance of DP steel to solidification cracking was attributed to sufficient liquid feeding (chapters 6 and 7). Adequate liquid feeding is, however, not the only reason for the high resistance to cracking. It is the inherent strength of the mushy region, which determines the resistance of a material to cracking. Whether cracking actually occurs (or not), depends on two factors; *i.e.* the strength of the mushy region and the stresses/strains acting on the mushy region due to the surrounding material. If the introduced strain cannot be transmitted within the mushy region, cracking occurs. The presence and distribution of grain boundary liquid films depends on the solidifying microstructure. Therefore, it is important to understand the solidifying microstructure and morphology of both the TRIP and DP steels during laser welding. In this regard, it is imperative to reconsider the dominant aspects that govern the solidifying microstructure, which are listed in the Figure 2.16. The shape of the solidifying grains as well as the growth rate of the solid-liquid interface depends on the geometry of the weld pool. The chemical composition together with the segregation of impurity elements like phosphorus; determine the actual solidification temperature range, the extent of liquid films and the coherency of the solid in the mushy region.

The effect of the solidifying microstructure on cracking susceptibility is discussed in this chapter and new results are provided to support this discussion.

[***]Some parts of this chapter are in, G. Agarwal, H. Gao, M. Amirthalingam, I.M. Richardson and M.J.M. Hermans, *Study of solidification cracking in advanced high strength automotive steels*, In: C. Sommitsch (ed) Mathematical Modelling of Weld Phenomena **12** (to be published).

[†††]Some parts of this chapter are in, G. Agarwal, A. Kumar, I.M. Richardson and M.J.M. Hermans, *Evaluation of solidification cracking susceptibility during laser welding in advanced high strength automotive steels*, submitted to Materials & Design.

8.1 Aspects of solidification cracking susceptibility

In this section, metallurgical aspects which affect the solidification cracking behaviour in TRIP and DP steels welded under the same conditions are discussed. First, the weld pool shape and solidification morphology is discussed followed by the effects on the solid-liquid interface growth rate and solidification time. Furthermore, the effect of interdendritic liquid feeding is addressed. Finally, the effect of the strain distribution in the mushy zone on solidification cracking is discussed.

8.1.1 Weld pool shape and solidification morphology

The weld surfaces indicate that the weld pool in the TRIP steel is teardrop shaped, while it is elliptically shaped in the DP steel. This observation was confirmed by the weld surface macrographs as shown in Figure 8.1 and by EBSD measurements (Figure 8.2), showing the prior austenite grain colour map. Both the Figures 8.1 (a) and 8.2 (a) reveal that for the TRIP steel, grains continue to grow in one direction towards the centreline. In the DP steel welds, grains bend continuously as they grow towards the weld centreline, as indicated by Figures 8.1 (b) and 8.2 (b). Therefore, the morphology of the grains is entirely different near the centreline.
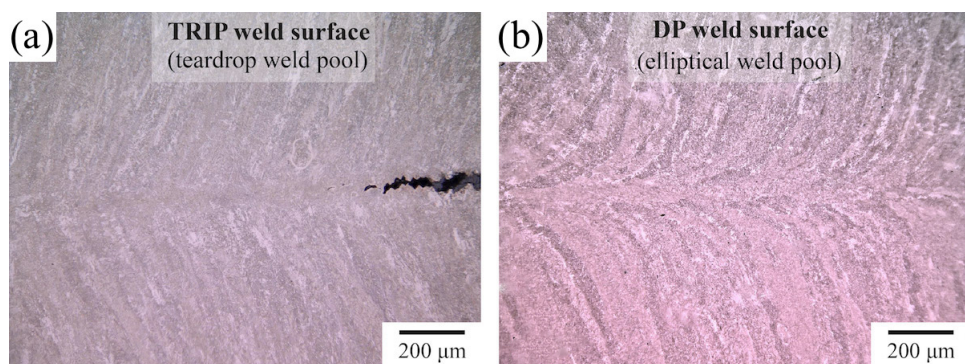

Figure 8.1: Macrographs of the weld surface. (a) TRIP steel and (b) DP steel.

The phosphorus elemental map in Figure 8.2 (c), obtained by EPMA, shows evidence of segregation at the austenite grain boundaries in TRIP steel. The phosphorus elemental map in Figure 8.2 (d) for the DP steel, shows that segregation is not that apparent in comparison with the TRIP steel. It should be noted that the DP steel has a low amount of P in the base metal (0.01 wt. %) as compared with the TRIP steel (0.089 wt. %). In chapter 6, notable segregation of phosphorus was also reported for the TRIP steel welds based on both atom probe tomography and phase field simulations. The weld surface of the TRIP steel welds was probed for inclusions using scanning electron microscopy. Secondary electron micrographs and EDS analysis shown in Figure 8.3 show aluminium-rich oxide, Fe_3P and AlN inclusions, which form during weld solidification [1, 2], particularly near the weld centreline. The melting point of Fe-Fe_3P eutectic is 1321 K [3], which confirms that the actual solidus temperature in some interdendritic regions of the weld falls 416 K below the equilibrium solidus temperature (1737 K); significantly broadening the solidification
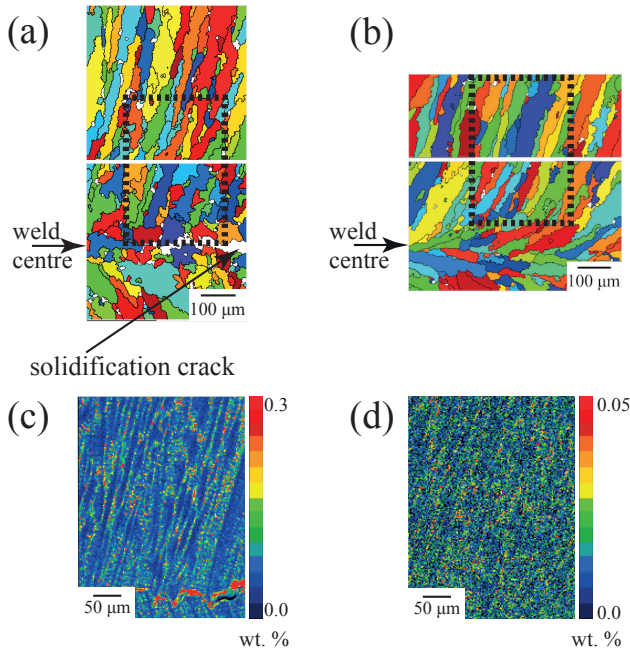
temperature range. ‡‡‡

Figure 8.2: Prior austenite grains on the weld surface in (a) TRIP steel and (b) DP steel. Phosphorus elemental maps in (c) TRIP steel and (d) DP steel. EPMA was performed within the regions indicated by the rectangular boxes in figures (a) and (b).
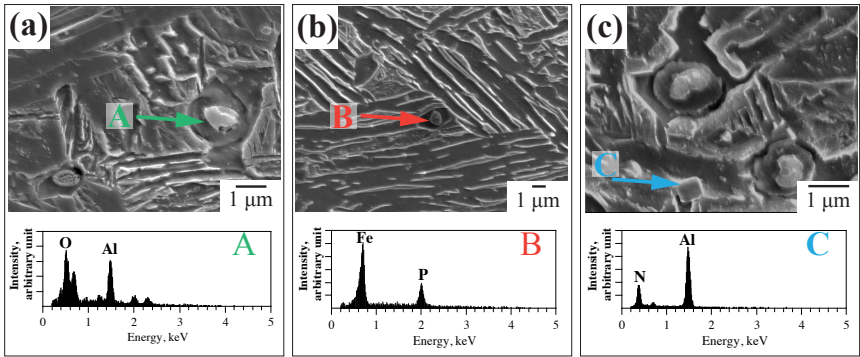

Figure 8.3: Inclusions and EDS analyses on the weld surface of TRIP steel.

---

‡‡‡Inclusions of Al form at a significantly higher temperature than Fe_3P [1, 2] (Al_2O_3, AlN starts to form approximately at 2080 K and 1939 K [2], respectively) and therefore does not affect the susceptibility to solidification cracking as much as Fe_3P.

From elemental mapping and inclusion analysis in TRIP steel, it can be inferred that grain boundary liquid films in TRIP steel prevent the solidifying microstructure from forming a coherent network until a relatively low temperature is reached. In the DP steel welds, inclusions were not found indicating a smaller solidification temperature range.

8.1.2 Influence of interface growth rate

From the solidification morphology, as discussed in the previous section, the rate at which the solid-liquid interface propagates can be determined. During solidification, the interface grows in the direction of the maximum temperature gradient, *i.e.* normal to the interface. The interface growth rate is related to the travel speed and is given by [4–6];

$$V_I = V_H cos\theta, \tag{8.1}$$

where, V_H, V_I and θ are the heat source travel speed, interface growth rate and the included angle between the travel direction and interface normal. Due to the teardrop shape of the weld pool in TRIP steel, the direction of the maximum temperature gradient does not change much. However, in the DP steel, due to the elliptical shape of the weld pool, the direction of the maximum temperature gradient changes continuously. As a consequence, θ reduces ($cos\theta$ increases) and hence the interface growth rate increases continuously from the fusion boundary to the centreline in the DP steel.

Based on the prior austenite grain colour map of the welds in both the steels, the macroscopic interface growth rate was calculated at various points from the weld centre-line towards the fusion boundary (Figure 8.4). The term macroscopic is used because the preferential dendrite growth direction <100> is not considered in the present calculation.
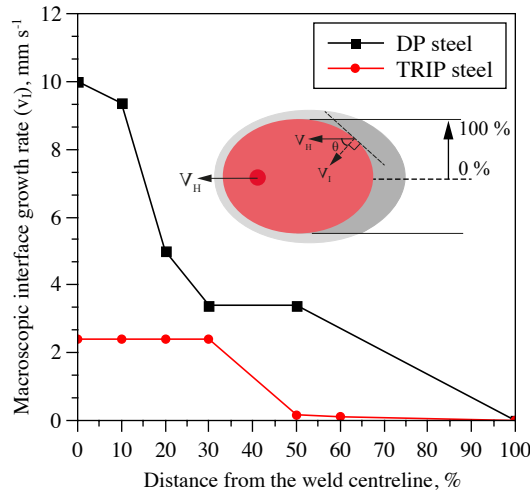

Figure 8.4: Macroscopic interface growth rate as a function of distance from the weld centreline. The inset schematic shows how the interface growth was determined at various points from the weld centreline.

In the TRIP steel welds, the interface growth rate is very slow near the fusion boundary and increases to a constant value near the weld centreline. In the DP steel welds, the interface also propagates relatively slowly at the fusion line but increases continuously, eventually matching that of the heat source near the centreline. Therefore, the region near the centre in TRIP steel welds spends considerably more time in the mushy state before solidification is completed. This allows segregation to take place on a larger scale and therefore the low melting point eutectic Fe-Fe$_3$P is observed near the centre. The Fe-P phase diagram (calculated using Thermo-Calc^{TM} with database TCFE8) shown in Figure 8.5 indicates that eutectic point of Fe-Fe$_3$P is at 1321 K with liquid containing approximately 10 wt. % P. Therefore, liquid films or liquid pockets in certain interdendritic regions encounter severe enrichment of phosphorus, before Fe$_3$P forms.
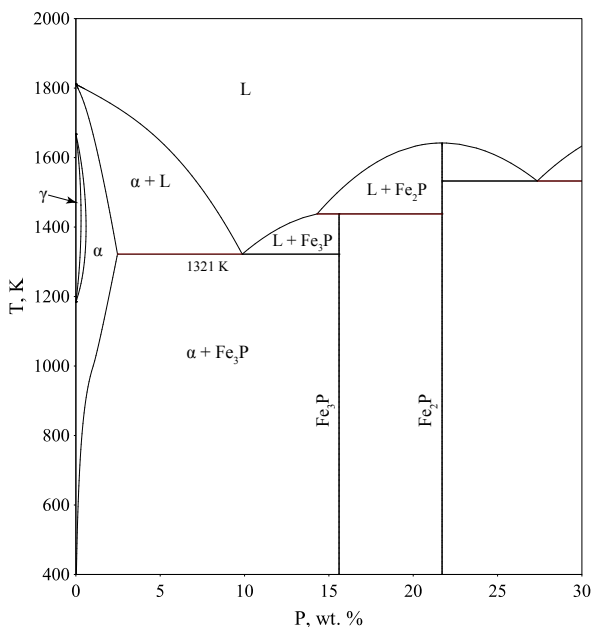

Figure 8.5: Fe-P phase diagram. Fe-Fe$_3$P eutectic point is at 1321 K with liquid containing around 10 wt. % P.

In addition, the primary dendrite arm spacing (PDAS) and the secondary dendrite arm spacing (SDAS) are proportional to $v^{-1/4}G^{-1/2}$ and $(vG)^{-1/3}$ respectively [7]. Where, v is the dendrite tip velocity and G is the thermal gradient. Assuming the magnitude of the thermal gradient to be similar in both of the steels, both PDAS and SDAS should be larger in the TRIP steel welds. Therefore, the coalescence temperature in the case of the TRIP steel is reduced due to both larger interdendritic arm spacings and associated microsegregation. As a result, the formation of a coherent solid network that can sustain transverse strain is delayed to low temperatures (an undercooling of more than 160 K was observed during the solidification experiments, in chapter 6), increasing the cracking susceptibility.

8.1.3 Interdendritic liquid feeding

Adequate liquid feeding in the interdendritic region is necessary to compensate for both the solidification shrinkage and thermal contraction of the solidifying dendrites, in order to avoid cracking. In chapter 7, based on an *in-situ* solidification study of these steels, liquid feeding in the interdendritic regions in the DP steel welds was observed and cracks were not detected. However, in the TRIP steel, cracking occurred during the last stages of solidification and liquid feeding was not encountered. Phase field simulation results presented in chapter 6 revealed a large degree of undercooling and narrow liquid channels in the TRIP steel, which act as a barrier for adequate liquid feeding. The interdendritic liquid feeding is also affected by the dendritic arm spacing, *i.e.* permeability. Both the experimental and phase-field modelling results in the preceding sections show that the weld microstructure is more dendritic in the case of the TRIP steel, which acts as an additional barrier for sufficient interdendritic liquid feeding.

8.1.4 Strength of the mushy zone

The metallurgical aspects discussed above determine the strength of the mushy zone, as also mentioned in Figure 2.16. The stresses/strains described in chapter 5 are imposed on the mushy region. An interplay between the induced stresses/strains and the strength of the mushy region dictates whether cracking occurs or not. Owing to the difference in solidification morphology in TRIP and DP steel welds, the tensile strain distribution is also different. Due to a steep angle of impingement of columnar grains at the centreline in the TRIP steel welds, a continuous liquid film is formed at the centreline [8]. As a result, transverse strain is mostly concentrated at the centreline as shown in the schematic Figure 8.6 (a). In the DP steel welds, multiple columnar grains bend towards the centreline and strain is partitioned among several grain boundary liquid films (Figure 8.6 (b)).

Figure 8.7 shows a schematic of the transverse strain distribution across the mushy region in both the steels. Solidification starts at the fusion boundary and the solid-liquid interface grows towards the weld centreline. At the last stages of solidification, the material close to the fusion boundary is strong compared to the weld centre. Thus, the transverse strain in the solid increases as one moves from the fusion boundary to the weld centre. In the presence of grain boundary liquid films, the transverse strain in the liquid films also increases. Due to the morphology of the grain boundaries in the DP steel welds, the transverse strain is partitioned among several liquid films. In addition, a high coherency temperature in the DP steel welds reduces the time over which the grain boundary liquid films persist. The overall mushy region is therefore relatively strong in the DP steel welds. In the case of TRIP steel, the coherency temperature is low; *i.e.* the grain boundary liquid films persist for a longer time. The overall mushy region is therefore weak. In presence of a concentrated transverse strain at the weld centre, there is a higher likelihood of solidification cracking. In other words, the threshold strain for solidification cracking in the TRIP steel welds is lower than in the DP steel welds.

In chapter 4, the transverse strains close to the fusion boundary, during welding, were found to be higher in the DP steel than in the TRIP steel (Figures 4.2 and 4.4). This implies that the strain imposed on the mushy region is also higher in the case of the DP steel. Since, no solidification cracking was observed in the DP steel, the mushy region is strong enough to withstand the high transverse strains.
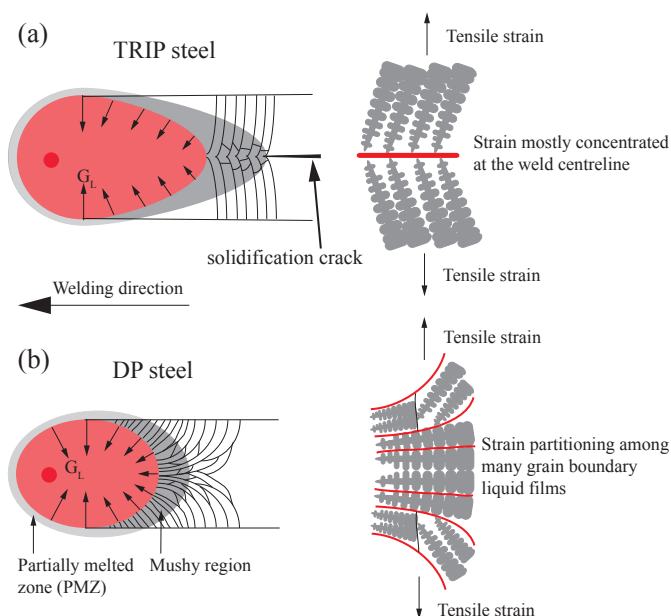
8

Figure 8.6: The effect of solidification morphology (weld pool shape) on strain partitioning. Teardrop weld pool shape leads to higher cracking sensitivity. In DP steel, strain is partitioned among several grain boundaries leading to higher cracking resistance.
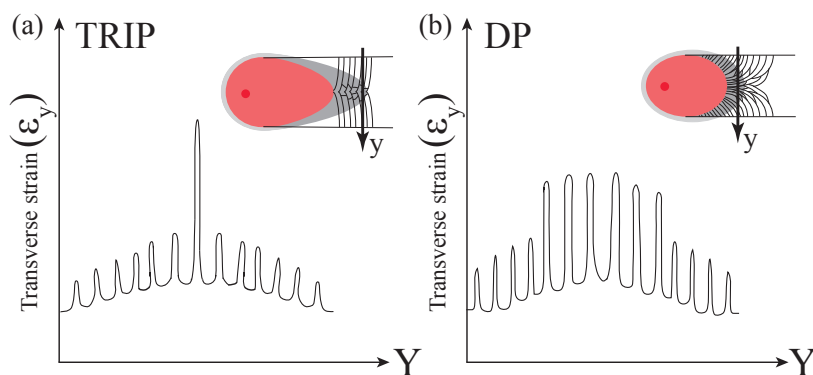

Figure 8.7: Schematic showing the transverse strain distribution along the mushy region in the transverse direction. (a) In the case of TRIP steel, the strain is concentrated at the liquid film present at the weld centre and (b) the transverse strain in the case of DP steel is partitioned among several liquid films present at the grain boundaries.

8.2 Phase-field model of solidification

To compliment the above analysis, a phase-field model of solidification was created, with a focus on the solidification morphology behind the weld pool. A two dimensional grid of $200 \times 300\,\mu m$ with a grid size of $1\,\mu m$ was defined. The solid-liquid interface thickness was assumed to be $3\,\mu m$. For the thermal conditions, transient temperature profiles at the fusion boundaries from the FE model (as described in chapter 3) were applied to both edges of the domain. A thermal gradient was defined according to the temperature difference from the fusion boundary to the weld centre line. The initial temperature at the bottom edge was given as the liquidus temperature. The initial concentration of the components was set to be the bulk composition in the liquid phase. One nucleus of δ-ferrite was placed at the bottom and the top left corner of the computational domain. The radius of the nucleus was set to $0.5\,\mu m$. The energy parameters for the phase interaction used in this simulation are listed in the Table 3.2, in chapter 3.

Figures 8.8 (a) through (d) show the solidification sequence of δ-ferrite columnar dendrites behind the weld pool in the TRIP steel welds. Solidification begins at the fusion boundary with δ-ferrite as the first solid phase (Figure 8.8 (a)). As the heat source (or weld pool) moves further, solidification progresses and columnar dendrites impinge (or coalesce) at the weld centreline (Figures 8.8 (b-c)). Note that due to the restriction of imposing a thermal gradient only in the y direction, the direction of solidification is fixed, *i.e.* perpendicular to the fusion boundary (domain boundary). Figure 8.8 (e) shows the solidification morphology in the DP steel welds with approximately the same solid fraction as that of the TRIP steel welds in Figure 8.8 (c). The secondary dendritic arm structure is more prominent in the TRIP steel welds. This is also evident from the microsegregation of phosphorous. Figures 8.8 (f) and (g) shows the P map in TRIP and DP steel welds. Note the scale differences in P due to the nominal compositional difference of P in both the steels. Phosphorous microsegregation of more than two times the nominal composition existss in the case of the TRIP steel welds.
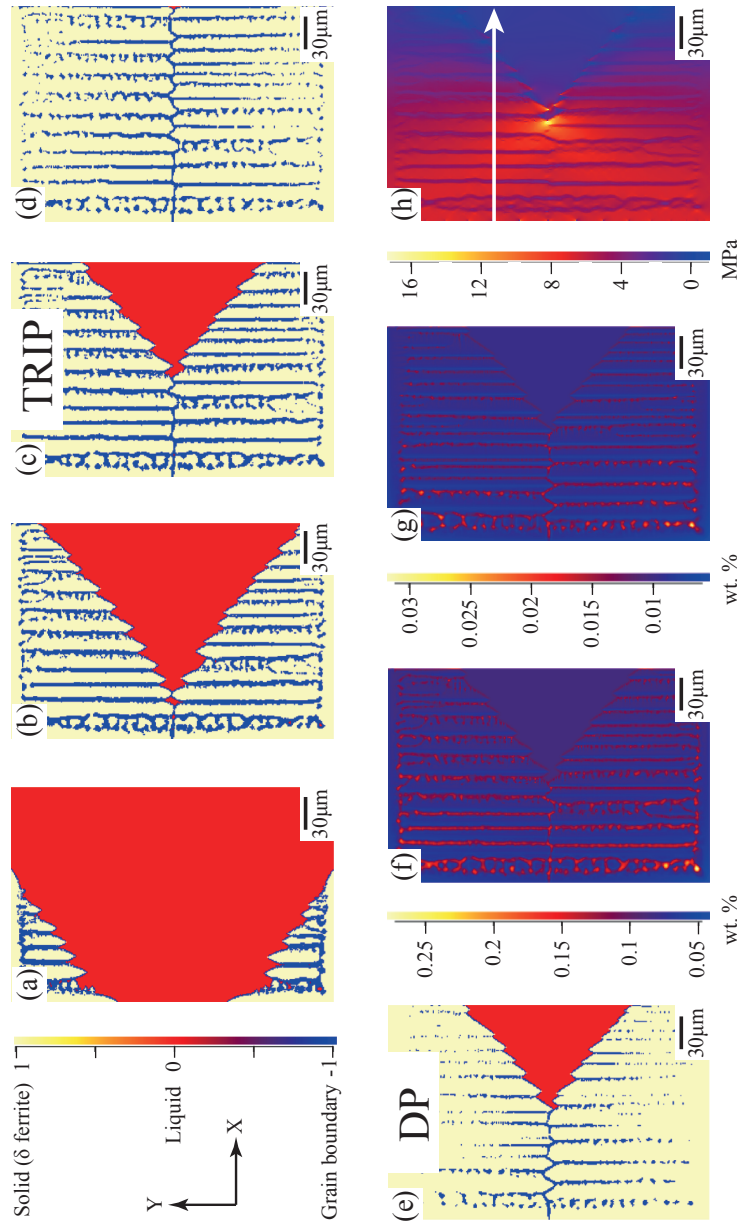
8

Figure 8.8: Phase field simulation of solidification behind the weld pool. (a) solidification starts at the fusion boundaries behind the weld pool in the TRIP steel, (b) columnar dendrites of δ-ferrite impinge at the centre, (c) solidification continues as the weld pool progresses further (at t=0.011 s), (d) primary solidification (δ-ferrite) is complete as the weld pool crosses the phase field domain completely, (e) solidification structure in the case of DP steel (at t=0.01 s), (f) P map in TRIP steel (at t=0.011 s), (g) P map in DP steel at t=0.01 s and (h) normal stress map in TRIP steel at t=0.011 s. An arrow is also marked along which the stress data is extracted for both the steels.

8

Figure 8.8 (h) shows the normal stress map in TRIP steel at t = 0.011 s. The stress distribution along the arrow indicated in Figure 8.8 (h) was extracted for both the steels and is shown in Figure 8.9. A more prominent dip in stress at the grain boundaries exists in the TRIP steel when compared with the DP steel.
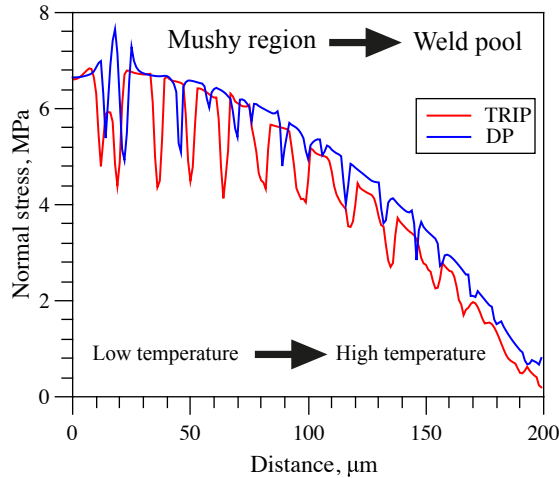

Figure 8.9: Normal stress distribution in TRIP and DP steel along the arrow indicated in figure 8.8 (h).

From the phase field results, secondary dendritic arms are more prevalent in the TRIP steel than in the DP steel welds. In addition, a higher P content also increases the secondary dendrite arm spacing. Thus, dendritic coherency in the TRIP steel is reached at a lower temperature compared to the case of the DP steel. This is also evident from Figures 8.8 (c) and (e). The delay in reaching complete solidification in the mushy zone of the TRIP steel close to the weld centreline increases the susceptibility to solidification cracking. Grain boundary liquid films are present for a longer duration in the TRIP steel than the DP steel, which means that tensile strain is imposed on the grain boundaries containing some liquid, for a longer duration, eventually reaching the required threshold for crack initiation. The prominent dip in normal stress at the grain boundaries in the TRIP steel (Figure 8.9) further indicates that the liquid films tend to persist until lower temperature in the TRIP steel. Furthermore, the width of the troughs indicating the presence of grain boundary liquid is larger in TRIP steel (Figure 8.9). As a result, the solid network is rendered weak and stress is concentrated at the weld centreline, eventually leading to cracking. At the same time, the dendritic network in the DP steel is more coherent and therefore more resistant to cracking.

The phase field modelling results corroborate the experimental analysis based on the effect of the metallurgical aspects, in particular the presence of grain boundary liquid films. The phase field model, however, does not include the effect of the weld pool shape.

8.3 Weld pool shape in TRIP and DP steel welds

It is well known that the weld pool shape (teardrop or elliptical) depends on the heat source travel speed. With increasing speed, the weld pool shape changes from circular, to elliptical and finally to a teardrop shape [9]. For the same welding parameters, the weld pool shape was observed to be different for the TRIP and DP steels, which must be related to the thermophysical properties, that in turn depend on the chemical composition. The thermal gradient is a minimum at the tail of the weld pool. If the latent heat of fusion generated upon solidification exceeds the heat dissipation at the centre, the weld pool elongates and eventually becomes teardrop shaped [6].
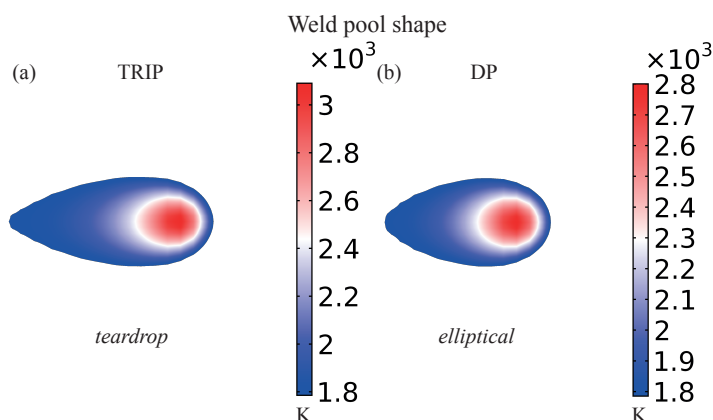

Figure 8.10: Weld pool shape calculated by finite element thermal model. (a) TRIP steel and (b) DP steel.

Figure 8.10 shows the calculated weld pool shape for both TRIP and DP steel welds for similar welding conditions. The difference in the tail of the weld pool shape can be attributed to the thermal diffusivity. Due to higher thermal diffusivity of the DP steel (Figure 8.11), the latent heat released upon solidification is dissipated faster than for the TRIP steel. Therefore, accurate determination of thermophysical properties is essential to correctly predict the weld pool shape.

Figure 8.12 shows the calculated liquidus and solidus isotherms in both the steels. The solidus temperature of TRIP (1593 K) and DP (1716 K) steel was calculated based on Scheil-Gulliver model with carbon as the fast diffusing component. Due to an extended solidification temperature range in the TRIP steel, the size of the mushy region is considerably large when compared to the DP steel.

The recent models on solidification cracking [10–12] tacitly assume that the weld pool shape does not change for a given alloy series (*e.g.* Al-Cu alloys), under the same welding parameters. As the evidence here shows, the assumption could be wrong even in alloys which are not vastly different in their compositions. Weld pool shape directly governs the solidification morphology (interface growth rate, PDAS, SDAS) and thus the strength of the mushy region.
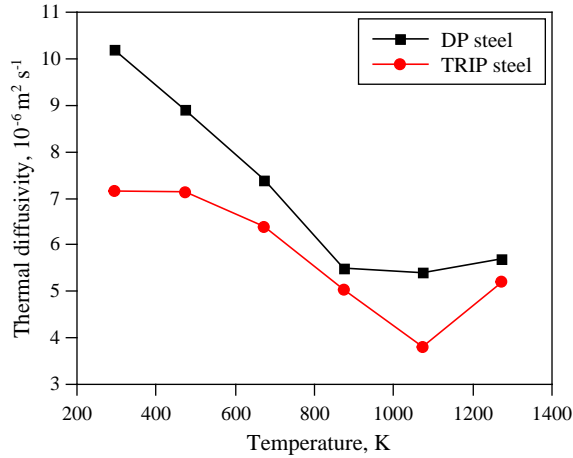
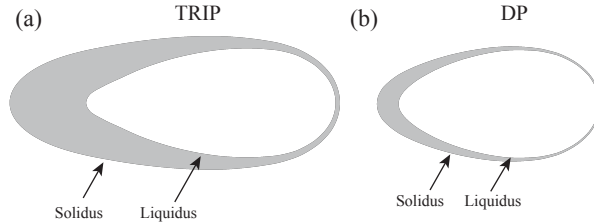Figure 8.11: Thermal diffusivity *versus* temperature of DP and TRIP steel.

Figure 8.12: Liquidus and solidus isotherms calculated by finite element thermal model. Solidus temperature is based on Scheil-Gulliver solidification model. (a) TRIP steel and (b) DP steel.

8

8.4 Effect of weld pool shape on solidification cracking in TRIP steel

From the previous discussion, it is apparent that the TRIP steel weld is susceptible to solidification cracking. A numerical and experimental study was carried out to show the effect of weld pool shape on solidification cracking behaviour.

The scheme of the experiments is listed in Table 8.1. Specimens were kept at the focal point of the optical system. In all the experiments, the heat input was 110 J mm^{-1} while changing simultaneously the laser power and travel speed (cases A to C). With this heat input a fully penetrated weld was obtained in all the cases. Each experiment was repeated five times. The weld pool shape of the TRIP steel was calculated for cases A to C, using the FE-thermal model described in chapter 3 (section 3.7). As the travel speed decreases from 9 mm s^{-1} to 7 mm s^{-1}, the weld pool shape changes from teardrop to elliptical (Figure 8.13). Also, the size of the mushy zone decreases.

Table 8.1: Experimental scheme.

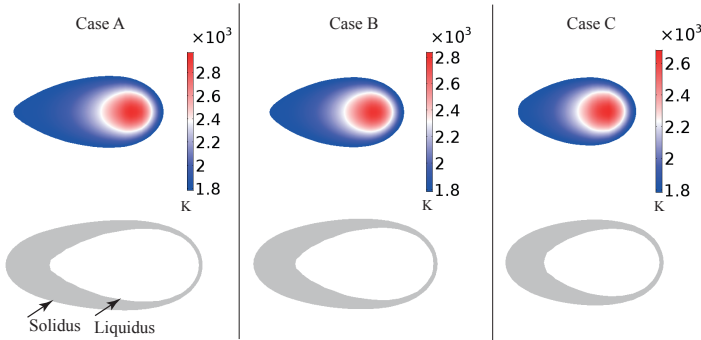| Case	Distance from the free edge, Y (mm)	Welding Parameters	
		Laser Power (W)	Speed (mm s^{-1})
A		990	9
B	5	880	8
C		770	7

Figure 8.13: Weld pool shape in cases A, B and C calculated by the finite element thermal model for TRIP steel. Liquidus and solidus isotherms are also shown. Solidus temperature is based on Scheil-Gulliver solidification model.
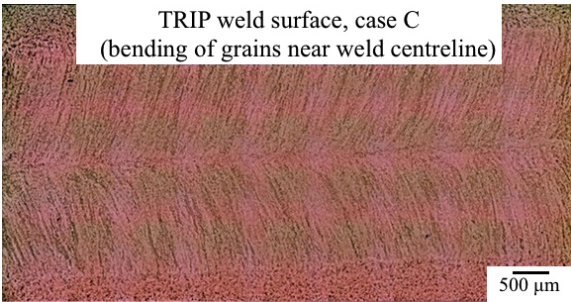

Figure 8.14: Macrograph of the weld surface of TRIP steel for case C.

Welding experiments were conducted for these conditions. Complete fracture was observed in cases A and B. Solidification cracking was not observed in any of the experiments for case C. In the latter case, the weld pool shape was elliptical, and an optical micrograph of the top surface (Figure 8.14) shows bending of grains towards the weld centre. The transverse strains close to the mushy zone were also calculated for all the cases as described in chapter 5. The transverse strains were found to be similar in all the cases and cannot explain the observed behaviour. Therefore, it can be inferred that the threshold strain required for cracking increases in case C. The rationale provided to explain the resistance to solidification cracking in DP steel also holds true in case C for the TRIP steel.

8.5 Present work in relation with Kou's criterion

A recent criterion of solidification cracking proposed by Kou [10] was applied to both the steels. According to the criterion, the susceptibility of solidification cracking is directly related to the $|dT/\sqrt{f_s}|$ near $\sqrt{f_s} = 1$. Temperature *versus* solid fraction (f_s) curves were obtained using Scheil-Gulliver solidification model. The steepness of the curve (Figure 8.15) in the case of the TRIP steel is twice that of the DP steel. Therefore, the TRIP steel is considered to be more susceptible to cracking.
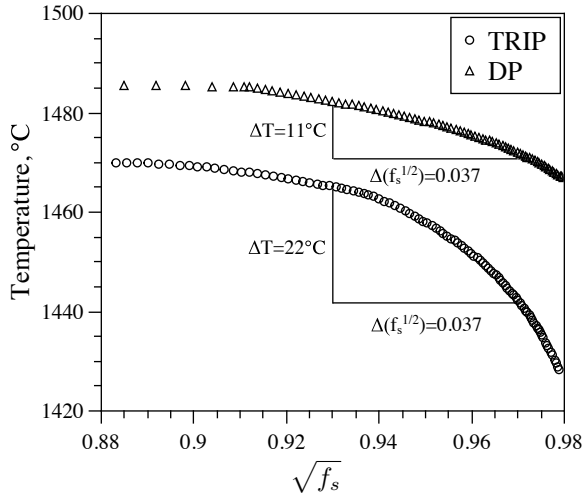
Figure 8.15: Prediction of cracking susceptibility using the Kou's criterion [10]. Slope of $T - \sqrt{f_s}$ curves with f_s varying from 0.87 to 0.94 indicates higher crack susceptibility of TRIP steel.

In general, the applicability of this criterion depends on the accuracy with which the solidification curves can be predicted under welding conditions. Also, it is important to note that all the existing models provide an indication of susceptibility to solidification cracking. Actual cracking behaviour depends on the welding conditions and in general

needs to be determined experimentally. For the welding conditions in this study, no solidification cracking was observed in either steel when welding was carried out beyond a certain distance from the free edge, *i.e.* restraint effect. Also, no cracking was observed in TRIP steel (case C) even when welding was carried out at a distance of 5 mm from the free edge.

8.6 Dominant aspects of solidification cracking

This Ph.D. research has focussed on describing the interplay between the fundamental factors which affect the susceptibility to solidification cracking. The models proposed by Rappaz *et al.* [12] and Kou [10] are based on a threshold strain rate beyond which cracking can occur. Nonetheless, as described in section 2.3, a combination of minimum local strain and local strain rate is essential for the initiation of a solidification crack. From the ductility curves shown in Figure 8.16, the strain imposed on the mushy region is related to the strain rate by:

$$\frac{d\varepsilon}{dT} = \frac{d\varepsilon}{dt}\frac{dt}{dT}. \tag{8.2}$$

The effect of the strain rate on the minimum strain required for crack initiation depends on the nature of the ductility curve of the material in question. For example, consider the ductility curve for materials A and B shown in Figures 8.16 (a) and (b), respectively. For material A, when a high strain rate is imposed on the mushy region (line A in Figure 8.16 (a)), the strain required for crack initiation decreases (ε_A). Conversely, when a lower strain rate is imposed on the mushy region (line B in Figure 8.16 (a)), the required strain for crack initiation increases ($\varepsilon_B > \varepsilon_A$). However, this effect is reversed if the ductility curve of a material is different, an example of which is shown in the ductility curve of material B (Figure 8.16 (b)). Figure 8.17 shows the reported ductility curves for plain carbon steels [13], in which the curves for 0.08 wt. % C and 0.16 wt. % C have indeed similar shapes to the schematic curves for materials A and B, respectively.

8

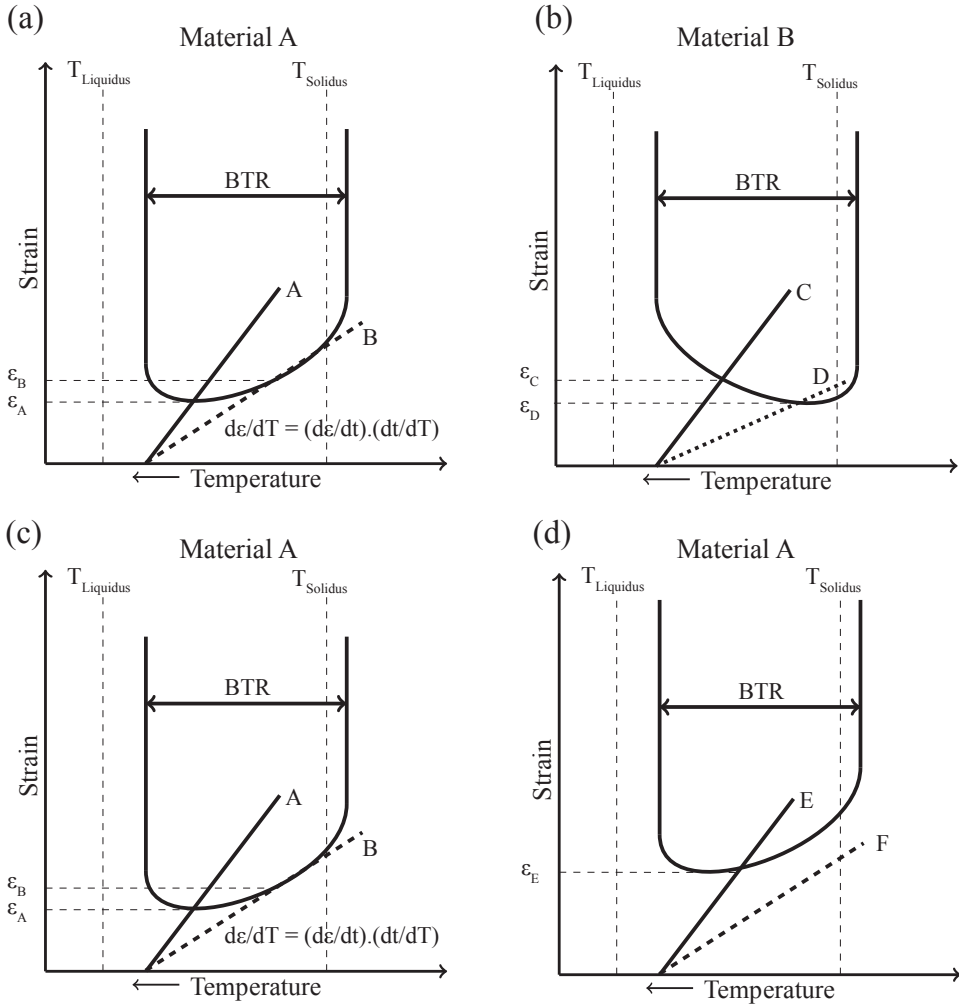Figure 8.16: Schematic of the ductility curve for materials A and B. (a) ductility curve of material A, (b) ductility curve of material B, (c) ductility curve of material A under a given welding conditions and (d) ductility curve of material A when different welding conditions exist. The ductility curves in (a) and (c) are identical; (c) and (d) are placed side by side for better visualisation of the difference.

Whether a material in the mushy state is able to withstand the imposed strain (rate) or not, depends on several aspects (Figure 2.16). Under a given set of welding conditions, the ductility curve of a material is unique, *i.e.* the ductility curve of a material changes as the welding conditions are altered. Take for example, the ductility curves of material A in Figures 8.16 (c) and (d). By changing the welding conditions, the ductility curve of the material A can shift upward as shown in Figure 8.16 (d). This could, for example, be achieved by having an elliptically shaped weld pool which can increase the strength of the mushy region and for which, the minimum strain required for crack initiation increases. In the ductility curves shown in Figures 8.16 (c) and (d), $\varepsilon_E > \varepsilon_A$ and cracking cannot occur if the strain imposed follows line F in Figure 8.16 (d). This hypothesis is supported by the experimental observations on the TRIP steel welds (cases A and C in Figure 8.13).
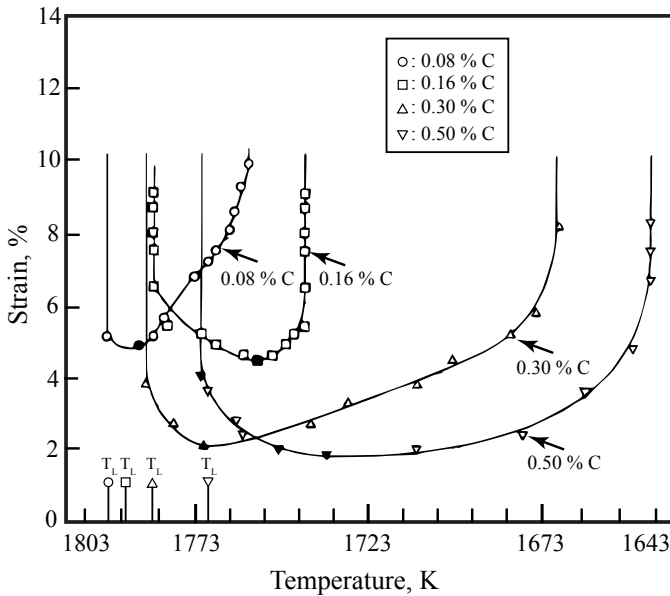

Figure 8.17: Ductility curves of several plain carbon steels. Adapted from reference [13], with permission from the Joining and Welding Research Institute (Osaka University).

References

[1] F. Matsuda, S. Katayama and Y. Arata, *Solidification crack susceptibility in weld metals of fully austenitic stainless steels (report v) : Solidification crack susceptibility and amount of phosphide and sulphide in SUS 310S weld metals,* Transactions of JWRI **10,** 201 (1981).

[2] M. Quintana, J. McLane, S. Babu and S. David, *Inclusion formation in self-shielded flux cored arc welds,* Welding Journal (Miami, Fl) **80,** 98s (2001).

[3] V. Shankar, T. P. S. Gill, S. L. Mannan and S. Sundaresan, *Solidification cracking in austenitic stainless steel welds,* Sadhana **28,** 359 (2003).

[4] W. F. Savage, *Solidification, segregation and weld imperfections,* Welding in the World **18,** 89 (1980).

[5] M. Rappaz, S. A. David, J. M. Vitek and L. A. Boatner, *Development of microstructures in Fe15Ni15Cr single crystal electron beam welds,* Metallurgical Transactions A **20,** 1125 (1989).

[6] S. A. David and J. M. Vitek, *Correlation between solidification parameters and weld microstructures,* International Materials Reviews **34,** 213 (1989).

[7] M. Rappaz and J. Dantzig, *Solidification,* 1st ed. (EFPL Press, 2009) pp. 519–563.

[8] S. Kou, *Welding Metallurgy,* 2nd ed. (John Wiley & Sons, Inc., 2003) pp. 263–296.

[9] R. Trivedi, S. A. David, M. A. Eshelman, J. M. Vitek, S. S. Babu, T. Hong and T. De-bRoy, *In situ observations of weld pool solidification using transparent metal-analog systems,* Journal of Applied Physics **93,** 4885 (2003) .

[10] S. Kou, *A criterion for cracking during solidification,* Acta Materialia **88,** 366 (2015).

[11] S. Kou, *A simple index for predicting the susceptibility to solidification cracking,* Welding Journal **94,** 374s (2015).

[12] M. Rappaz, J. M. Drezet and M. Gremaud, *A new hot-tearing criterion,* Metallurgical and Materials Transactions A **30,** 449 (1999).

[13] F. Matsuda, H. Nakagawa, H. Kohmoto, Y. Honda and Y. Matsubara, *Quantitative evaluation of solidification brittleness of weld metal during solidification by in-situ observation and measurement (report ii),* Transactions of JWRI **12,** 73 (1983).

8

9

Conclusions, recommendations and scope for future research

9.1 General conclusions

SOLIDIFICATION cracking occurs due to the strain induced in the mushy region during welding in combination with the prevailing metallurgical features during weld metal solidification. The experimental and numerical investigation of solidification cracking susceptibility during laser welding in TRIP and DP steel sheets was carried out in this work and the following conclusions are drawn:

1. Segregation of low partition coefficient elements (such as phosphorus) enriches the remaining liquid at grain boundaries and extends the solidification temperature range. The liquid films persist for an extended duration thereby increasing the susceptibility to solidification cracking.

2. Shorter and wider liquid channels due to a reduction in segregation facilitate adequate interdendritic liquid feeding which compensates for the solidification shrinkage and thermal contraction.

3. Liquid feeding in the interdendritic regions in DP steel was observed and cracks were not detected. However, in TRIP steel, cracking occurred during the last stages of solidification and liquid feeding was not observed. A feeding pressure of the order of 10^4 Pa was estimated for the DP steel during the last stage of solidification.

4. While keeping the external restraint and heat input unchanged, a change in the welding parameters can lead to an increase in the minimum strain required for crack initiation, *i.e.* the ductility curve shifts upward.

5. For the same material, the solidifying microstructure resulting from an elliptically shaped weld pool has higher resistance to solidification cracking than the solidifying microstructure obtained from a teardrop shaped weld pool. An elliptically

shaped weld pool allows partitioning of the transverse strain between several grain boundary liquid films. In addition, the duration for which the mushy region persists is reduced thereby increasing the resistance to solidification cracking.

6. For accurate prediction of the weld pool shape, determination of the high temperature thermophysical properties is essential. Small deviations in the thermal diffusivity can lead to a change in the weld pool shape and thus the grain morphology. A sufficiently accurate thermal model can be used to determine the conditions that result in an elliptical weld pool shape.

7. Due to higher thermal diffusivity in DP steel than in TRIP steel, the welds showed an elliptically weld pool shape while a teardrop weld pool shape existed in the majority of TRIP steel welds.

8. The strain imposed on the solidifying weld metal decreases as welding is carried out further away from a free edge.

9.2 Recommendations to the industry

In general, the weldability should be considered in the design phase of new steel grades. Based on the outcome of this research, the following recommendations are proposed to the industry:

1. The equilibrium solidification temperature range and the phase transformations occurring during solidification are an indicator of the susceptibility to solidification cracking. In general, with an increase in the solidification temperature range the susceptibility to cracking increases. Therefore, the phase diagram of the steels should be plotted. For this purpose, commercially available softwares (*e.g.* Thermo-Calc^{TM}) can be used.

2. To get an estimate of the actual solidification temperature range, weld solidification under non-equilibrium conditions should be considered. In this regard, the Scheil-Gulliver solidification model can be assumed to be valid and temperature as a function of solid fraction (f_s) data can be extracted from commercially available thermodynamic software (*e.g.* Thermo-Calc^{TM}). The cracking susceptibility of the alloys can be ranked following Kou's model, *i.e.* by calculating the slope of the $T - \sqrt{f_s}$ curves with f_s varying from 0.87 to 0.94. Cracking susceptibility increases as the magnitude of the slope increases. In this study, the magnitude of the slope for the steel in which no cracking occurs is 297 K while the magnitude for the steel where cracking occurred is 594 K. Since only two steels were investigated, a database should be made for the existing and the upcoming steel grades. The extent to which the model is applicable should also be tested experimentally.

3. Consideration should be given of the extent of the segregation of alloying elements during weld metal solidification, with emphasis on the elements such as sulphur, phosphorus and boron *etc*. A first estimate of the segregation levels and thus the extended solidification temperature range can be made by the use of commercially available software such as MICRESS$^{®}$ under typical welding conditions.

9

4. For crack susceptible steels, a suitable increase in the distance from the flange edge can lead to sound welds without changing the heat input. The distance from the free edge without cracking can be reduced further by reducing the heat input appropriately.

5. When the flange width does not allow an appropriate increase in the distance from the free edge, a sufficiently low welding speed (without changing the heat input) can increase the resistance to solidification cracking. In order to achieve optimum welding conditions and with minimal impact on productivity, a reasonably accurate thermal model and thus the high temperature thermophysical properties of steels, in particular the thermal diffusivity, should be available. The thermal model can be used to select appropriate welding conditions under which an elliptical weld pool shape is obtained, leading to an increase in the resistance to cracking. In the cases where reliable thermophysical properties are unavailable, a series of welding experiments should be conducted by proportionally decreasing both the laser power and travel speed to obtain a safe window of welding parameters. The above recommendation also holds true in the continuous steel sheets production lines.

9.3 Scope for future research

On the basis of the present study, the following possibilities for future academic and industrial research are generated:

1. A failure criterion for the initiation of solidification crack should be defined; it can be based on a threshold strain (and strain rate) needed for the rupture of liquid films present at the grain boundaries and/or interdendritic boundaries.

2. The applicability of the knowledge generated, based on the standard hot cracking tests and *in-situ* solidification study, needs to be determined for practical welding geometries (butt and overlap weld configurations) and conditions.

3. In order to better understand interdendritic liquid feeding in the mushy region during welding, fluid flow must be incorporated in future models describing weld solidification.

4. To elaborate upon the effect of solidification temperature range and element partitioning in delta ferrite and austenite, solidification cracking should be studied on steel compositions ranging from hypo-to hyper-peritectic.

9

Summary

THE CO_2 emission regulation of passenger vehicles has become pressing in the last two decades and the target emission between 2020-2025 is converging globally. One of the fundamental ways to achieve this target in the automotive industry is to reduce the overall weight of the vehicle. The reduction of weight should not compromise vehicle performance or passenger safety. To meet this demand, new steels under the umbrella of advanced high strength steels (AHSSs) are being increasingly developed and adopted. These steels comprise on average 30-35 percent by weight of a typical car body-in-white and possess high strength, ductility and toughness. The increased strength and ductility allows the use of thinner gauge steels thus reducing vehicle weight, leading to an improvement in the vehicle's fuel efficiency. Apart from formability requirements in these steels, weldability of such steels is important. Some of these steels contain high amounts of alloying elements, which are required to achieve the necessary mechanical properties, but render these steels susceptible to weld solidification cracking. Typically, preformed parts are welded in a flange geometry and the use of laser welding allows the flange width to be minimised. However, when welding is carried out too close to the edge, solidification cracking may occur. The automotive industry has reported solidification cracking during assembling parts by laser welding. In the continuous galvanising lines, entry and exit coils are also joined by laser welding. During welding of some AHSS grades, solidification cracking has also been reported, leading to serious downtime and production losses, which need to be avoided.

Solidification cracks, similar to hot cracks or hot tears in casting, are intergranular or interdendritic cracks that occur during the final stages of solidification. Two fundamental factors generated by the weld thermal cycle are responsible for solidification cracking. The first is the restraint which is usually the mechanical or thermal stresses/strains imposed on the solidifying weld and the second is the solidifying microstructure. It is the complex interaction of these two factors which leads to solidification cracking. If the stress imposed on the weld metal exceeds its strength, cracking occurs. The objective of the research work was to study and elucidate the solidification cracking phenomenon in two popular and commercially available advanced high strength steels (AHSS), namely transformation-induced plasticity (TRIP) and dual phase (DP) steel sheets. In particular, the effects of the following aspects on susceptibility to solidification cracking were considered; restraint (strain imposed), shape of the weld pool, solidification morphology, segregation, solidification temperature range, dendrite coherency and interdendritic liquid feeding. For this purpose, a mixture of both experimental and modelling techniques were employed. A laser welding arrangement, similar to that used in the standard hot cracking test, prescribed by the steel institute VDEh (Verein Deutscher Eisenhüttenleute), was employed. To vary the restraint, bead-on-plate laser welding was carried out on single sided clamped specimens at increasing distances from the free edge. In TRIP steel sheets, solidification cracking was observed when welding was carried out close to the

free edge. The crack length decreased as the distance from the free edge is increased. At a certain minimum distance (13 mm), no solidification cracking was observed. In DP steel welds, no cracking was observed for the studied welding conditions. For the no cracking condition, *in-situ* strain evolution during laser welding was measured by means of digital image correlation. Auxiliary illumination coupled with an optical narrow bandpass filter, suppressed the intensity of the laser plume light entering the camera of the digital image correlation system and allowed strain measurements up to 1.5 mm from the fusion boundary.

A sequentially coupled 3D finite-element based thermal mechanical model (with isotropic hardening) was developed to numerically calculate the temperature and strain fields during welding. The model was validated based on temperature and strain measurements. The validated model was used to calculate strains that are difficult to obtain experimentally. The transverse strain (perpendicular to the welding direction) near the mushy zone was used to explain the experimentally observed cracking behaviour. A threshold strain at a point close to the fusion boundary was determined for the condition in which no cracking was observed, *i.e.* when welding was carried out at a distance of 13 mm from the free edge. This threshold strain was further validated by varying the heat input, both in the model and the experiments. Reducing the heat input decreased the cracking susceptibility in TRIP steel welds, *i.e.* the critical distance from the free edge at which no cracking occurs decreased.

As mentioned before, the occurrence of solidification cracking depends on two factors; *i.e.* the strength of the mushy region and the stress/strain acting on the mushy region due to the surrounding material and/or constraints. The strain is localised at the grain boundary liquid films. If the introduced strain cannot be accommodated within the mushy region, cracking occurs. The morphology of the solidifying grains affects the distribution of the grain boundary liquid films. Under similar welding conditions, the weld pool in the TRIP steel was observed to be teardrop shaped while in the DP steel the shape was (more) elliptical. This was confirmed by optical macrographs, morphology of the prior austenite grains as well as by finite element thermal model of welding. The difference in weld pool shape in both the steels is attributed to the different thermo-physical properties. In TRIP steel, the grains grow mostly in one direction whereas in DP steel, the solidifying grains bend continuously towards the weld centreline. In the TRIP steel welds, the interface growth rate is very slow near the fusion boundary and increases slightly to a constant value near the weld centreline. In the DP steel welds, the interface also propagates relatively slowly at the fusion line but increases continuously, eventually matching the heat source velocity near the centreline. Therefore, the region near the centre in the TRIP steel welds spends considerably more time in the mushy state before solidification is completed. During solidification, the solid rejects solute into the solid-liquid interface. In the TRIP steel welds, considerable segregation at the grain boundaries, particularly of phosphorus, was found; which increases the solidification temperature range significantly. The increase in the solidification temperature range was also confirmed by the presence of Fe_3P inclusions. In the DP steel welds, segregation was found to be limited (low amount of phosphorus in the base metal) and inclusions were not observed, indicating that the solidification temperature range does not increase significantly. Due to a higher content of alloying elements in TRIP steel, the solidifying

microstructure is more dendritic. This was also confirmed by a phase field model of so-lidification. A more prominent dendritic nature of the microstructure restricts adequate interdendritic feeding, which compensates for the solidification shrinkage and thermal contraction.

Owing to the teardrop shape of the weld pool in TRIP steel welds, the transverse strain is mostly concentrated in the liquid films present at the weld centreline while the strain is partitioned among several grain boundary liquid films in DP steel welds due to the presence of an elliptically shaped weld pool. It is thus inferred that the threshold strain for solidification cracking in TRIP steel welds is lower than in the DP steel welds. While keeping the heat input constant by proportionally decreasing both the laser power and travel speed, additional welding experiments were conducted on TRIP steel sheets. As the travel speed was decreased, the weld pool changed from a teardrop to an elliptical shape, which was confirmed both by the thermal model and by the optical macrograph of the weld surface. No solidification cracking was observed for this case, indicating an increase in the strength of the mushy zone

The solidification behaviour of both the steels was studied in more detail, by em-ploying high-temperature laser scanning confocal microscopy. To simulate the welding conditions, a stable melt pool was created at the centre of a thin circular disk shaped specimen while the outer rim remained solid. Solidification cracking was observed in the interdendritic region during the last stage of solidification. Atom probe tomography revealed notable enrichment of phosphorus in the last remaining liquid. Phase field simulations also confirmed phosphorus enrichment leading to severe undercooling in the interdendritic region, resulting in longer and narrower liquid channels that persist in the crack vulnerable region. In the presence of tensile stress, an opening at the interden-dritic region is difficult to fill with the remaining liquid due to low permeability and high viscosity, resulting in solidification cracking. In the case of the DP steel, liquid flow was observed in the interdendritic regions during the last stage of solidification. Liquid flow speed was derived and the pressure difference that causes this flow was estimated using Darcy's law. It was also found that the rate of liquid feeding was higher than the rate of solidification shrinkage and the rate of thermal deformation combined.

The outcome of this PhD research highlights the importance of many aspects that affect the susceptibility to solidification cracking. The construction of a unified model for the accurate prediction of cracking sensitivity, taking into account all these aspects, still remains a challenging task.

Samenvatting[§§§]

De regelgeving ten aanzien van CO_2 emissie van personenwagens is in de afgelopen twee decennia aangescherpt en de doelstelling met betrekking tot de beperking van de uitstoot tussen 2020-2025 convergeert wereldwijd. Eén manier om dit doel in de automobielindustrie te bereiken is het verlagen van het totale gewicht van het voertuig. De reductie van het gewicht mag echter de functionele eigenschappen en de veiligheid van de inzittenden niet compromitteren. Om aan alle eisen te voldoen, worden in meerdere mate nieuwe geavanceerde hogesterkte staalsoorten ontwikkeld en geïmplementeerd. Een autochassis bestaat gemiddeld voor 30 tot 35 procent uit deze staalsoorten, die een hoge sterkte combineren met een grote ductiliteit. Deze combinatie maakt het mogelijk dunnere en dus lichtere componenten/onderdelen te gebruiken, waardoor de auto een hogere brandstofefficiëntie behaalt. Naast een eis aan vormbaarheid van deze staalsoorten is ook de lasbaarheid van groot belang. Sommigen van deze staalsoorten bevatten hogere gehaltes aan legeringselementen, noodzakelijk om de gewenste mechanische eigenschappen te behalen, maar die tegelijkertijd het staal ook gevoelig maken voor het ontstaan van stolscheuren tijdens smeltlassen. Veelal worden voorgevormde onderdelen gelast in een flens-geometrie en het toepassen van laserlassen staat een vermindering van de flensbreedte toe ten opzichte van het conventioneel toegepaste weerstandspuntlassen. Wanneer er echter te dicht bij de rand gelast wordt, kunnen stolscheuren optreden. De automobielindustrie heeft tijdens het assembleren van onderdelen door middel van het laserlasproces stolscheuren gerapporteerd. Ook in continu verzinklijnen, waar opeenvolgende spoelen staal verbonden worden door middel van laserlassen hebben zich bij sommige geavanceerde hogesterkte staalsoorten stolscheuren voorgedaan. Dit leidt tot met ernstige uitvaltijd en productieverlies, hetgeen voorkomen dient te worden.

Stolscheuren, vergelijkbaar met warmscheuren in gietstukken, zijn intergranulaire of interdendritische scheuren die optreden tijdens de laatste fase van de stolling. Twee fundamentele factoren ten gevolge van de thermische cyclus van het lasproces zijn verantwoordelijk voor het optreden van stolscheuren; de eerste factor is de mechanische en thermische spanning/rek in het stollende lasmetaal en de tweede de microstructuur van het stollende metaal. Het is de complexe interactie tussen deze twee factoren die leidt tot scheurvorming. Als de geïntroduceerde spanning, de sterkte van het lasmetaal overschrijdt, zal scheurvorming optreden.

Het doel van het onderzoek was om het fenomeen stolscheuren te onderzoeken en te verklaren voor twee veelvuldig toegepaste en commercieel verkrijgbare geavanceerde hogesterkte staalsoorten, te weten transformation-induced plasticity (TRIP) en dual phase (DP) staal. Hierbij zijn met name de effecten van de volgende aspecten op de stolscheurgevoeligheid in beschouwing genomen; de tijdens het lassen geïntroduceerde rek, de vorm van het lasbad, de stollingsmorfologie, segregatie, de grootte van het stoltraject, de

---

[§§§]Dutch translation by ir. R. Welschen. Proofreading by dr. ir. M.J.M. Hermans.

coherentie van dendrieten en interdendritische vloeistoftoevoer. Een combinatie van zowel experimentele en modelleertechnieken is hiervoor aangewend.

Er is gebruik gemaakt van een laserlasopstelling, overeenkomstig standaard warm-scheurtesten, zoals voorgeschreven door het staal instituut VDEh (Verein Deutscher Eisenhüttenleute). Het werkstuk wordt eenzijdig ingeklemd en de spanning en rek om-standigheden van het werkstuk wordt gemodificeerd door de afstand van de 'bead-on-plate las' ten opzichte van de vrije zijde van het werkstuk te variëren.

In TRIP-staal worden stolscheuren waargenomen als dicht bij de vrije zijde gelast wordt. De scheurlengte neemt af als de afstand tot de vrije zijde van het proefstuk toe-neemt. Stolscheuren doen zich niet meer voor wanneer er een minimum afstand (13 mm) tot de vrije zijde wordt aangehouden. In de DP-staal lassen zijn voor de bestudeerde las-condities geen scheuren aangetroffen. Onder de omstandigheden waarbij geen scheuren optraden is met digitale beeld correlatie tijdens het laserlassen de rekontwikkeling gemeten. Dit is mogelijk tot een afstand van 1,5 mm van de smeltlijn door gebruik te maken van aanvullende belichting en een optische bandpass filter om de hoge lichtintensiteit van de plasmapluim te onderdrukken.

Een thermisch-mechanisch sequentieel gekoppeld drie dimensionaal eindige elemen-ten model (met isotrope versteviging) is ontwikkeld om de temperatuur- en rekvelden tijdens het lassen te berekenen. Het model is gevalideerd met temperatuur- en rekmetin-gen. Dit gevalideerde model is vervolgens gebruikt om rekken te berekenen voor locaties waar het experimenteel niet mogelijk is. De transversale rek (loodrecht op de lasrich-ting) in de buurt van de gedeeltelijk gesmolten zone is gebruikt om het experimenteel bepaalde scheurgedrag te verklaren. Een drempelwaarde voor de rek op een punt dicht bij de smeltlijn is bepaald voor specifieke lascondities waarbij geen scheurvorming is opgetreden, zijnde de minimum afstand van 13 mm ten opzichte van de vrije zijde. Deze drempelwaarde voor de rek is bevestigd door de warmteïnbreng te variëren. Een lagere warmteïnbreng zorgt voor een verlaagde gevoeligheid voor scheurvorming tijdens het lassen van TRIP-staal. Dit betekent dat de kritische afstand tot de vrije zijde van het werkstuk, waarbij geen scheurvorming is waargenomen, verkleint kan worden.

Zoals vermeld hangt het optreden van scheurvorming af van twee factoren; te weten de sterkte van de gedeeltelijk gesmolten zone en de spanning/rek die door het omliggende materiaal op de gedeeltelijk gesmolten zone wordt uitgeoefend. De door de spanning geïntroduceerde rek is geconcentreerd in de nog aanwezige vloeistoffilms op de korrel-grenzen. Als de rek in de gedeeltelijk gesmolten zone te groot is, ontstaan scheuren. De aard en de verdeling van deze vloeistoffilms hangt nauw samen met de morfologie van de stolstructuur en is verschillend voor TRIP- en DP-staal. Onder vergelijkbare lasomstan-digheden is de vorm van het lasbad in TRIP-staal druppelvormig, terwijl in DP-staal een meer elliptische lasbadvorm ontstaat. Dit is bevestigd met optische macrofoto's, bepaling van de oriëntatie van voormalige austenietkorrels en het thermisch eindige elementen model van het lassen. Het verschil in lasbadvorm is te wijten aan de verschillen in thermo-fysische eigenschappen van beide staalsoorten. Korrels groeien loodrecht op de smeltlijn parallel aan de maximale temperatuurgradiënt. Door het verschil in lasbadgeometrie zullen aanwezige korrels in TRIP-staal in dezelfde richting blijven doorgroeien totdat de centrale lijn van de las is bereikt, terwijl bij DP-staal de korrels voortdurend van richting veranderen totdat ze in het centrum van de las evenwijdig groeien aan de voortlooprich-

ting van het lasproces. Ook de stolsnelheid is daarom verschillend. Bij TRIP-staal is de stolsnelheid bij de smeltlijn van de las relatief laag en neemt slechts licht toe, terwijl bij DP-staal de stolsnelheid continu toeneemt en gelijk is aan de lasvoortloopsnelheid bij het naderen van de centrale lijn van de las.

Daarom bevindt het gebied bij de centrale lijn van de las bij TRIP-staal zich veel langer in een gedeeltelijk gesmolten toestand voordat de stolling voltooid is. Tijdens de stolling treedt segregatie op. In TRIP-staal worden de korrelgrenzen significant verrijkt aan met name fosfor. Deze segregatie verlengt het stoltraject, wat bevestigd wordt door de aanwezigheid van laagsmeltende Fe_3P insluitsels. In DP-staal is segregatie slechts in beperkte mate waargenomen (het fosfergehalte in DP-staal is veel lager in vergelijking tot TRIP-staal) en de aanwezigheid van insluitsels is niet aangetoond. Dit impliceert dat het stoltraject niet aanzienlijk verandert.

Tevens is waargenomen dat de stolstructuur van TRIP-staal meer dendritisch is in vergelijking tot DP-staal. Dit is ook bevestigd door een 'phase field' stollingsmodel. Een meer uitgesproken dendritisch karakter van de microstructuur bemoeilijkt vloeistofstroming in de interdendritische ruimte, waardoor de krimp ten gevolge van stolling en thermische contractie niet gecompenseerd kan worden.

Door het druppelvormige lasbad bij het lassen van TRIP-staal is de transversale rek geconcentreerd in de aanwezige vloeistoffilms in de centrale lijn van de las. In het elliptisch lasbad bij DP-staal wordt de rek verdeeld over een aantal vloeistoffilms aan de korrelgrenzen. Hieruit kan worden afgeleid dat de drempelwaarde voor de rek waarbij stolscheuren optreden lager is voor TRIP-staal dan voor DP-staal. Aanvullende experimenten zijn uitgevoerd voor TRIP-staal met een constante warmteïnbreng, maar met proportionele lagere laservermogens en voortloopsnelheden. Als de lassnelheid wordt verlaagd verandert het uiterlijk van het lasbad van een druppel naar een elliptische vorm. Dit blijkt uit macrofoto's van het lasoppervlak en is bevestigd door de resultaten van het thermische model. Onder deze omstandigheden worden geen stolscheuren waargenomen, wat betekent dat de sterkte van de gedeeltelijk gesmolten zone toeneemt.

Het stolgedrag van beide staalsoorten is in meer detail bestudeerd door middel van hoge-temperatuur laser scanning confocale microscopie. Om lascondities te simuleren is een stabiel smeltbad gevormd in het centrum van een dun cirkelvormig proefstukje waarbij de buitenrand vast blijft. Stolscheuren werden waargenomen in de interdendritische zones tijdens de laatste fase van de stolling. Atom probe tomografie toonde in de laatst stollende vloeistof een aanzienlijke verrijking van fosfor aan. Ook 'phase field' simulaties voorspellen de fosforverrijking. Dit resulteert in smeltpuntverlaging in de interdendritische zone en leidt tot langere en smallere vloeistofkanalen tussen de korrels. In de aanwezigheid van trekspanningen treden scheuren op die niet worden opgevuld door de nog aanwezige vloeistof, doordat de permeabiliteit laag is door het dendritische karakter van de stolling en de relatief hoge viscositeit van de vloeistof. In DP-staal is een vloeistofstroming waargenomen in de interdendritische zone tijdens de laatste fase van de stolling tijdens hoge temperatuur laser scanning confocale microscopische experimenten. De stroomsnelheid is bepaald en het drukverschil dat verantwoordelijk is voor de stroming is geschat met behulp van de wet van Darcy. Het blijkt dat de toevoersnelheid van vloeistof groter is dan de krimpsnelheid ten gevolge van stolling en de thermische krimp.

Het promotieonderzoek toont aan dat de stolscheurgevoeligheid van geavanceerde hogesterkte stalen beïnvloed wordt door meerdere factoren. Het accuraat voorspellen van de stolscheurgevoeligheid blijft, gezien al deze aspecten, een uitdaging.

Acknowledgements

GIVEN the opportunity to take "time machine" and be again in 2014, I would make the same decision of pursuing PhD and relive the bumpy and yet enjoyable moments that life so generously arranged. The journey has been enjoyable largely on account of the people that I have come to know over the last four years.

First and foremost, I would like to express my sincere gratitude to my promoters, dr. Marcel Hermans and professor Ian Richardson for their academic support, freedom and encouragement. Both of them provided an effective and challenging research environment which has helped me profoundly to think independently. Through the ups and downs that make up a PhD, Marcel has been a constant source of guidance. I owe him a huge debt of gratitude. Sincere thanks are due to dr. Murugaiyan Amirthalingam (Muru), whom I first met during my master thesis at Tata Steel in IJmuiden. Muru introduced this PhD topic and from thereon, my research journey in Delft started. Thank you, Muru!

The PhD project was part of the programme–physics of failure, carried out in the framework of the partnership program of the Materials Innovation Institute (M2i) and the Foundation for Fundamental research on Matter (FOM), which is part of the Netherlands Organisation for Scientific Research (NWO). I thank all the partners involved in this research. In particular the industrial partner, Tata Steel Nederland b.v., is acknowledged for its financial support and provision of the test materials. I thank ir. Roel Boesenkool, dr. Ellen van der Aa and dr. Tony van der Veldt, all at Tata Steel, for their support and useful suggestions. I acknowledge dr. Viktoria Savran (M2i) for managing the project.

I would like to thank Annette Bor (NWO), Marian Smit–Kooima and Froukje Prins (former secretaries in our department) as well as the present secretaries in our department: Saskia Brandt Corstius, Ellen Vendrig, Prisca Koelman and Saskia van der Meer for their administrative help.

The confocal microscopy experiments were performed in Australia at the University of Wollongong. I thank professor Rian Dippenaar and dr. Suk-Chun Moon for extending their help in using this fantastic piece of instrument. The collaboration proved to be fruitful and I appreciate their involvement in useful discussions. Also, I thank Rian for arranging our accommodation in Wollongong as well as for hosting us for lunch and dinner on several occasions. I thank professor John Norrish and his wife, Madeline, for having us for dinner to their home and also for taking us out on a day trip in Sydney. Madeline, you have amazing skills in cooking Indian food! Sincere thanks are due to professor Laurens Katgerman and professor Jilt Sietsma for reviewing one of the manuscript (chapter 7).

The PhD project was undertaken in close cooperation with another project focussing on the modelling aspects of solidification cracking. I thank the former post-docs, Muru and dr. He Gao for engaging in long and fruitful discussions. Short and intense ping-pong sessions with He were full of fun!

I sincerely thank Jurriaan van Slingerland for his technical support in conducting the laser welding experiments. I enjoyed philosophical discussions with him about

List of publications

- G. Agarwal, A. Kumar, I.M. Richardson and M.J.M. Hermans, *Evaluation of solidification cracking susceptibility during laser welding in advanced high strength automotive steels*, submitted to Materials & Design.

- A. Kumar, G. Agarwal, R. Petrov, S. Goto, J. Sietsma and M. Herbig, *Microstructural evolution of white and brown etching layers in pearlitic rail steels*, Acta Materialia **171**, 48 (2019). DOI: 10.1016/j.actamat.2019.04.012

- G. Agarwal, H. Gao, M. Amirthalingam, I.M. Richardson and M.J.M. Hermans, *Study of solidification cracking in advanced high strength automotive steels*, In: C. Sommitsch (ed) Mathematical Modelling of Weld Phenomena **12** (to be published).

- G. Agarwal, H. Gao, M. Amirthalingam and M.J.M. Hermans, *Study of solidification cracking susceptibility during laser welding in an advanced high strength automotive steel*, Metals **8**, 673 (2018). DOI: 10.3390/met8090673

- G. Agarwal, A. Kumar, H. Gao, M. Amirthalingam, S.C. Moon, R.J. Dippenaar, I.M. Richardson and M.J.M. Hermans, *Study of solidification cracking in a transformation-induced plasticity-aided steel*, Metallurgical and Materials Transactions A **49**, 1015 (2018). DOI: 10.1007/s11661-018-4505-7

- G. Agarwal, M. Amirthalingam, S.C. Moon, R.J. Dippenaar, I.M. Richardson and M.J.M. Hermans, *Experimental evidence of liquid feeding during solidification of a steel*, Scripta Materialia **146**, 105 (2018). DOI: 10.1016/j.scriptamat.2017.11.003

- H. Gao, G. Agarwal, M. Amirthalingam, M.J.M. Hermans and I.M. Richardson, *Investigation on hot cracking during laser welding by means of experimental and numerical methods*, Welding in the World **62**, 71 (2018). DOI: 10.1007/s40194-017-0524-z

- H. Gao, G. Agarwal, M. Amirthalingam, M.J.M. Hermans and I.M. Richardson, *Hot cracking investigation during laser welding of high-strength steels with multi-scale modelling approach*, Science and Technology of Welding and Joining **23**, 287 (2018). DOI: 10.1080/13621718.2017.1384884

- G. Agarwal, H. Gao, M. Amirthalingam and M.J.M. Hermans, *In-situ strain investigation during laser welding using digital image correlation and finite-element based numerical simulation*, Science and Technology of Welding and Joining **23**, 134 (2018). DOI: 10.1080/13621718.2017.1344373

• G. Agarwal, M. Amirthalingam, M.J.M. Hermans and I.M. Richardson, *In-situ investigation of solidification behaviour of an Al-containing Transformation Induced Plasticity steel melt pool*, In: 10th International Conference on Trends in Welding Research, TWR 2016, 9th International Welding Symposium of Japan Welding Society (9WS), 2016, Tokyo, Japan.

• G. Agarwal, M. Amirthalingam, M.J.M. Hermans, I.M. Richardson, S.C. Moon and R.J. Dippenaar *In-situ investigation of solidification behaviour of commercial automotive steels using high temperature microscopy*, In: Proceedings of the Visual-JW2016, 2016, Osaka, Japan.

Curriculum Vitae

Gautam AGARWAL

Education

1992–2006	Schooling Saint Paul's Senior Secondary School, Kota, India (1992–2004) Modi Public School, Kota, India (2004–2006)
2007–2011	B.Tech in Metallurgical Engineering Indian Institute of Technology (BHU), Varanasi, India
2011–2014	M.Sc. in Metallurgical Engineering RWTH Aachen University, Aachen, Germany
2019	Ph.D. in Materials Science and Engineering Delft University of Technology (TU Delft), Delft, The Netherlands

Thesis: Study of solidification cracking during laser welding in advanced high strength steels

Promotors: Dr. ir. M.J.M. Hermans and Prof. dr. I.M. Richardson

Preventing solidification cracking is an essential prerequisite for the safety of a welded structure. An undetected solidification crack has the potential to cause premature failure during service. Two conditions generated by a weld thermal cycle are responsible for the initiation of solidification cracks. The first is the presence of excessive stresses/strains imposed on the solidifying weld metal and the second is the existence of a weak solidifying microstructure. For more than five decades, weld solidification cracking has been a subject of considerable interest. Cracking has been observed in various alloys, used in a wide range of engineering applications. Despite achieving a better understanding over this period, an accurate prediction of the occurrence of solidification cracking under a specific set of conditions remains difficult. An alloy with a high susceptibility to solidification cracking can still exhibit good weldability upon selection of appropriate welding conditions. Conversely, an alloy with supposedly high resistance to cracking, can still fail when subjected to inappropriate welding conditions.

The objective of the research work reported in this dissertation is to study and elucidate the solidification cracking phenomenon in two popular and commercially available automotive sheet steels, namely transformation-induced plasticity (TRIP) and dual phase (DP) steels. In particular, the effect of restraint (strain imposed), shape of the weld pool, solidification morphology, segregation, solidification temperature range, dendrite coherency and interdendritic liquid feeding on susceptibility to solidification cracking is considered.